Department of Electrical and Information Engineering
ELECTRICAL AND INFORMATION ENGINEERING
Ph.D. Program
S.S.D. ING-INF/02 Campi Elettromagnetici

Dissertation

Second-Harmonic Generation in Plasmonic Nanostructures

---

by

NOOR Ahsan

Supervisors:
Prof.ssa Antonella D' Orazio (DEI, Poliba)
Dr. Cristian Ciracì (IIT, CBN Lecce)

Coordinator of the Ph.D. Program:
Prof. Mario Carpentieri

Course **n**°*34, 01/11/2018-30/04/2022*

Department of Electrical and Information Engineering
ELECTRICAL AND INFORMATION ENGINEERING
Ph.D. Program
S.S.D. ING-INF/02 Campi Elettromagnetici

Dissertation

Second-Harmonic Generation in Plasmonic Nanostructures

by

NOOR Ahsan

Supervisors:
Prof.ssa Antonella D' Orazio (DEI, Poliba)
Dr. Cristian Ciracì (IIT, CBN Lecce)

Coordinator of the Ph.D Program:
Prof. Mario Carpentieri

*Course **n**°34, 01/11/2018-30/04/2021*

Declaration

I, Noor Ahsan, declare that this thesis titled, "Second-Harmonic Generation in Plasmonic Nanostructures" and the work presented in it are my own. I confirm that:

- This work was done wholly or mainly while in candidature for a research degree at this University.
- Where any part of this thesis has previously been submitted for a degree or any other qualification at this University or any other institution, this has been clearly stated.
- Where I have consulted the published work of others, this is always clearly attributed.
- Where I have quoted from the work of others, the source is always given. With the exception of such quotations, this thesis is entirely my own work.
- I have acknowledged all main sources of help.
- Where the thesis is based on work done by myself jointly with others, I have made clear exactly what was done by others and what I have contributed myself.

Signed:

Date:08-05-2022

Noor Ahsan

Acknowledgements

I would like to express my sincere gratitude to my supervisor Dott. Cristian Ciracì (IIT, CBN Unile) for his technical guidance in research presented in this thesis. I would also like to thank my supervisor Prof.ssa Antonella D'Orazio from Politecnico Di Bari for her support and encouragement throughout the course of the study. I thank Prof. Michele Celebrano and Prof. Domenico de Ceglia for being part of the technical evaluation committee. I I thank the people and the Computational Nanoplasmonics group at the IIT, CBN Unile for their company. Finally, I thank my family members for their understanding and support.

Abstract

Nonlinear plasmonics is a bridge linking the conventional nonlinear optical components with the contemporary nanoptics. At optical frequencies, metals support surface electromagnetic modes —surface plasmon-polaritons — that have the ability to localize light far below the diffraction limit, down to sub-wavelength regions. This unique property can be exploited to enhance inherently weak nonlinear light-matter interactions. In this thesis, we present numerical study of second-harmonic generation (SHG) in distinct plasmonic structures. A part of this thesis comprises the study of SHG in *hybrid plasmonic nanopatch antennas*. Exploiting the localized modes (field enhancements) of the nanopatch system, we demonstrate that the nonlinearities arising from spacer layer of the nanopatch system can be greatly enhanced. The presented study enables an efficient and technologically competitive route to realize nanophotonics devices like onchip frequency converter and optical bistability. *Plasmonic Waveguides* provide an integrated platform to develop efficient nanoscale ultrafast photonic devices. In this context, second part of the thesis presents a novel semi-analytical method to study SHG from plasmonic and/or photonic waveguides with nonlinearities of its constituents modeled using the "Hydrodynamic Theory of free electrons". Nonlocal optical effects, arising due to plasma gas nature of electrons in the media like metal, significantly alter the optical response of the system, especially, at the sizes much smaller than the incidence of radiation. Our proposed method, thus, allows the studies in the presence of additional degrees of freedom and their implications.

Contents

List of Figures

List of Tables

Preface

Interaction of light with metallic nanostructures enables the coupling of free electrons in metal with the incident electromagnetic (EM) excitations near its surface, formally known as the surface plasmons. These so-called plasmonic resonances open the opportunities to manipulate light confine light on the nanoscale. Whereas, their excitation rely on the geometry of the structure, which may include extended metal surfaces and the resonances associated the individual metallic nanoparticles.

Nonlinear optical effects are a crucial part in modern photonic applications, including the control over the frequency spectrum of laser light, ultrashort pulses generation, and optical signal processing. Inherently, optical nonlinearity is weaker as nonlinear responses of a material are governed by the interacting photons in the material. The nonlinear optical effects, which are proportional to the intensity of electromagnetic field, can be strengthened in environments providing mechanisms for field enhancement. The large electromagnetic fields arising from the plasmonic excitations enable the weaker nonlinear processes, to be substantially enhanced. Apart from providing the enhanced nonlinear effects with ultrafast response times, plasmonic nanostructures allow nonlinear optical components to be scaled down to the sizes at miniaturized scale.

There are several ways to achieve plasmonic-aided boosting of nonlinear optical effects. For example, strong local fields in plasmonic systems had demonstrated the surface-enhanced Raman scattering, for applications like single-molecule detection. For nonlinear optics, this naturally transforms to higher effective nonlinearities of the metal in plasmonic structure or the neighboring dielectric material. Likewise, plasmonic excitations can be extremely sensitive to dielectric properties of the metal and the surrounding medium. This is the basis for label-free plasmonic sensors: a small change in the refractive index near the metal surface result in significant modifications of the plasmonic resonance. Finally, plasmonic excitations

respond on the timescale of femto-seconds, which allow ultrafast modulation and processing of the optical signals. Nonlinear effects in plasmonics nonstructure could therefore lead to several intriguing nanophotonic functionalities, and recent years have saw the emergence of metal nanostructures designed to favor distinct nonlinear processes.

The main component of the thesis is articulated around the first three chapters. The first Chapter introduce the basics of linear plasmonics and its applications. Foundation of nonlinear optics and nonlinear plasmonics are then reviewed. We highlighted the main scientific concepts and technological achievements in the field of nonlinear plasmonics and present advanced nonlinear plasmonic models and systems. The aim of this chapter is to offer a background that allow the reader to contextualize the main contributions in the following chapters.

The purpose of the second chapter is to show an interesting application of the plasmonic system to boost the nonlinear optical effects. The studied plasmonic system, hybrid plasmonic nanopatch antenna, which act as an amplifier to enhance the nonlinearities at the "plasmonic hot-spot" of system for application of optical second-harmonic generation. The quasi phase-matching like conditions from the conventional nonlinear optics are achieved in the nanoscale system to optimize the second-harmonic generation process. Such a study provide the possibility to enable efficient on-chip frequency converters.

The third chapter of the thesis is devoted to the study of second-harmonic generation in plasmonic waveguides. The pith of this chapter is the derivation and application of a novel semi-analytical formulation to study second-harmonic generation in plasmonic waveguide. The proposed formulation enables the study of the nonlinear phenomenon in the presence of variety of nonlinear sources including the sources arising from the nonlocal optical effects and electron spill-out.

Chapter 1

Plasmonics and Nonlinear Optics

Nanophotonics concerns the study of light-matter interactions at the nanometer scale [1–3]. Recent years saw a great deal of interest in nanophotonics research and its applications [4, 5], including the *nonlinear optics* at the nanoscale [1–5]. *Plasmonics* is a sub-field of nanophotonics, which primarily studies the nano-optical phenomena at the interfaces and surfaces of nanostructured metals with dielectrics and semiconductors [2–5]. This chapter presents an introduction to plasmonics and its applications in nonlinear optics. We review linear plasmonics in section 1.1. We then provide a brief introduction to nonlinear optics and nonlinear plasmonics in section 1.2. *Advanced plasmonics* models and their nonlinear optical counterparts are discussed section 1.3. We further introduce the numerical methods utilized in this manuscript in section 1.4. The current discussion aims to set a pedagogical foundation for the works presented in the subsequent chapters.

1.1 An overview of plasmonics

A fundamental limitation on optical confinement is posed by *diffraction*: light cannot be confined to regions much smaller than one-half of its wavelength [6]. Plasmonics overcome this limitation, and its implications are among the major driving forces in nanophotonic-based research and technological advancements [4]. Plasmonic systems owe their sub-diffraction characteristics to *surface plasmons* (SPs): the collective excitation of free electrons at metallic surfaces and nanostructured particles. SPs were predicted by Richie [7] while studying energy loss of electrons passing through thin metal films, and later observed by Powell and Swan [8]. These

excitations take two distinct forms: a freely propagating electron density wave along metal surfaces called the *Surface Plasmon Polaritons* (SPPs), and oscillations of localized charges in metallic nanoparticles known as the *Localized Surface Plasmons* (LSPs). Plasmonics is concerned with a rich set of exotic optical phenomena. In the following, we review the main principles and highlight some applications.

1.1.1 Basics of Plasmonics

Most properties of surface plasmons can be described using a classical electrodynamics approach based on Maxwell's equations [2, 3]. The macroscopic Maxwell's equation set [2, 3, 9] reads as (in SI units):

$$\nabla \times \mathbf{E} = -\frac{\partial \mathbf{B}}{\partial t}, \tag{1.1a}$$

$$\nabla \times \mathbf{H} = \frac{\partial \mathbf{D}}{\partial t} + \mathbf{J}, \tag{1.1b}$$

$$\nabla \cdot \mathbf{D} = \rho, \tag{1.1c}$$

$$\nabla \cdot \mathbf{B} = 0, \tag{1.1d}$$

with **E** being the electric field, **D** the electric displacement field, the magnetic field **B**, the magnetization field **H**, the charge density, and **J** being the electric current density. All the quantities above are dependent on time (t) and space $(\mathbf{r})$.

Commonly, the electric displacement field relates to the electric field by the electric polarization density **P** defined as:

$$\mathbf{D} = \varepsilon_0 \mathbf{E} + \mathbf{P}. \tag{1.2}$$

Similarly, magnetization field and magnetic field are related by magnetic polarization density **M** defined as:

$$\mathbf{B} = \frac{1}{\mu_0}\mathbf{H} + \mathbf{M}, \tag{1.3}$$

where in Eqs. (1.2-1.3) the ε_0 and μ_0 represent the permittivity and permeability of free space, respectively. The electric (**P**) and magnetic (**M**) polarization densities describe the material's response to the EM fields. These quantities are defined in terms of electric dipole moment d**p** and magnetic dipole moment d**m** per unit volume

of the material [9], defined as:

$$\mathbf{P} = \frac{\mathrm{d}\mathbf{p}}{\mathrm{dt}} = \varepsilon_0 \chi \mathbf{E}, \tag{1.4a}$$

$$\mathbf{M} = \frac{\mathrm{d}\mathbf{m}}{\mathrm{dt}} = \mu_0 \chi_m \mathbf{H}. \tag{1.4b}$$

Both the polarization and magnetization are also dependent on the space and time. In the right-hand side of Eq. (1.4) the terms are first-order series expansions of **P** and **M** in terms of the electric (**E**) and magnetizing fields (**H**), respectively. We shall show in section 1.2.1 that the nonlinear response of the materials can be incorporated by adding higher-order terms to the polarization field. The Eqs. (1.2-1.3) together with Eq. (1.4), can be rewritten as:

$$\mathbf{D} = \varepsilon_0 \varepsilon_r \mathbf{E}, \tag{1.5a}$$

$$\mathbf{B} = \mu_0 \mu_r \mathbf{H}, \tag{1.5b}$$

which are formally known as constitutive relations, with $\chi = \varepsilon_r - 1$ and $\chi_m = \mu_r - 1$. The quantities ε_r and μ_r are relative permittivity and permeability of materials, defined as the ratios between the material's permittivity and permeability to the corresponding free space values. The material parameters combined with boundary conditions [2, 3, 9]– the continuity of the components of the fields (electric and magnetic) parallel to the interface between two different adjoining materials – enables finding the closed-form solutions of Eq. (1.1) to specify EM response of a system.

We will now discuss the two most basic plasmonic systems: the metal-dielectric or metal-insulator (MI) half space and the metallic sphere. The purpose of presenting these systems [2, 3] is to introduce basic *terminologies* in plasmonics and modes of operations in distinct plasmonic systems. We will be considering non-magnetic materials for the discussed problems, i.e., $\mu_r = 1$ and $\mathbf{M} = 0$ (so will be the case throughout the manuscript). Moreover, the dielectric function of the metal is obtained through the well-known Drude model [2, 3], defined as:

$$\varepsilon_{metal} = 1 - \frac{\omega_p^2}{\omega^2 + i\gamma\omega}, \tag{1.6}$$

with ω_p being the plasma frequency defined as $\omega_p = \sqrt{\frac{n_0 e^2}{m_e \varepsilon_0}}$, γ is the electron collision rate, and ω is the angular frequency of the electromagnetic wave. In the expression for ω_p, the n_0 electron density e is the charge of one electron, and m_e is the mass of one electron. This model provides reliable results in the local response approximation (LRA), i.e., when microscopic dynamics relating to the quantum mechanical nature of the free electrons in the metal are neglected [10, 11].

Surface plasmon propagation at metal-Dielectric interface

Surface electromagnetic waves that travel on the interface between a metal and a dielectric material are surface plasmons polariton (SPPs). These are charge oscillations at the metal surface, coupled to the propagating EM waves. Here, we discuss the SPPs excited at the infinite metal-dielectric (MI) half-spaces (see Fig. 1.1).

Assuming time-harmonic fields, i.e., $\mathbf{E}(\mathbf{r},t) = \mathbf{E}(\mathbf{r})e^{-i\omega t}$, and no external charges, i.e. $\rho = 0$, combining Eqs. (1.1) with the constitutive relation Eqs. (1.5) we get the usual following *wave equation*:

$$\nabla^2 \mathbf{E}(\mathbf{r}) - \varepsilon(\mathbf{r}) k_0^2 \mathbf{E}(\mathbf{r}) = 0, \tag{1.7}$$

with $k_0 = \frac{2\pi}{\lambda}$ being the free space wavenumber of the EM wave having wavelength λ, and $\varepsilon(\mathbf{r})$ is the relative the permittivity of different materials in the EM system.

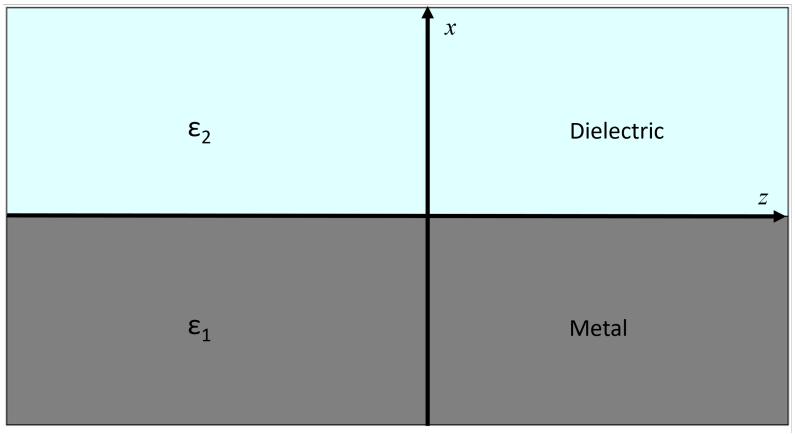

Fig. 1.1 An infinite metal dielectric half space.

For the considered geometry in which interface traverses indefinitely in the xz-plane (see Fig. 1.1), the solution to the Eq. (1.7) takes the form $\mathbf{E}(x,y,z) = \mathbf{E}(x)e^{ik_z z}$. Upon back substituting this form of solution to Eq. (1.7) yields:

$$\frac{\partial \mathbf{E}(x)}{\partial z^2} + (\varepsilon(\mathbf{r})k_0^2 - k_z^2)\mathbf{E}(x) = 0 \tag{1.8}$$

where k_z is the *propagation constant* of the surface plasmon polaritons.

It can be shown [2, 3] that the propagation constant of the SPPs at the MI interface with relative permittivity of the metal and dielectric denoted as ε_1 and ε_2, respectively is the following:

$$k_z = \sqrt{\frac{\varepsilon_1 \varepsilon_2}{\varepsilon_1 + \varepsilon_2}}. \tag{1.9}$$

Note that both ε_1 and ε_2 can be frequency dependent. Now, we are ready to characterize the surface plasmon polaritons at the MI interface:

- The surface plasmons polaritons (SPPs) are characterized by a broadband dispersion relations (see Fig. 1.2).

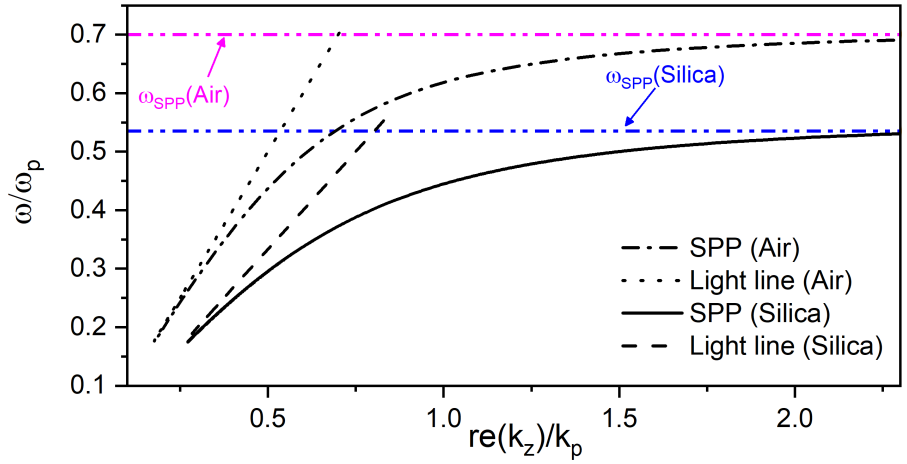

Fig. 1.2 Dispersion relation of the SPP propagation along the MI interface for air: the SPP (dash-dotted line) and light line (dotted line), and silica as dielectric: SPPs (solid line) and the corresponding light line (dashed line). The horizontal (dot-dot-dashed) lines represent the SPPs wavelengths in each of the case. In extracting these result, the permittivity of the metal is described using the Eq. (1.6) with parameters $\omega_p = 1.34 \times 10^{16}\ s^{-1}$ and $\gamma = 1.07 \times 10^{14}\ s^{-1}$.

- Propagation constant "k_z" always remained on the right-hand side of the light line as can be seen in Fig. 1.2. Such an increase in the wavevector parallel to the surface of the metal determines an increase in the mode confinements perpendicular to the interface (x-direction). Mathematically, this argument can

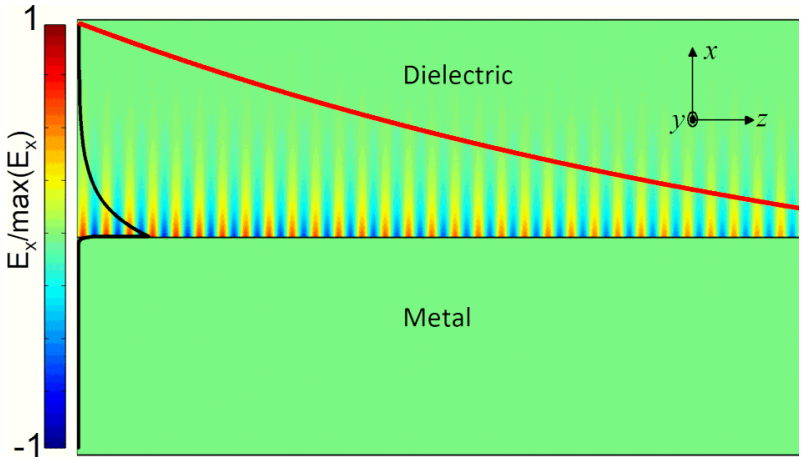

Fig. 1.3 Finite element simulation of surface plasmon propagation along metal-dielectric (silica) half-spaces; the black-line ($x-$component of the field) shows decay of the field transverse to prorogation's direction of the mode, and red-line represent the intensity decay of the SPP in the direction of propagation.

  be backed by the fact that the field's amplitude decay is proportional to $e^{-|k_x||x|}$ (see Fig. 1.3, the black line) with $k_x = \sqrt{k_z^2 - \varepsilon_{metal}(\frac{\omega}{c})^2}$ [2, 3]. This property shows the SPPs' potential to concentrate light to the subwavelength volumes.

- The intensity of the field decays exponentially in the direction of propagation. For the field with amplitude A, the decay of intensity of the field in the direction of propagation is proportional to $|A|^2 e^{-Im(k_z)z}$ (see the red line in Fig. 1.3)
- Propagation length of a SPP mode, which represent the energy attenuation of the mode along the direction of propagation can be defined as $L = 2Im(k_z)$.

Although discussed for a simple configuration, the SPPs' properties can be generalized for a variety of systems [12–14]. Optical configurations that support the SPPs are known *plasmonic waveguides*. In section 1.1.3, we will present latest advances in nanophotonics concerning plasmonic waveguides.

Electromagnetic scattering from a metallic sphere

Collective oscillations of the electrons that propagate along metallic surface are called SPPs. In optically small metal particles, the SPPs' propagation is hindered due to the spatial confinement, and the localized surface plasmon modes appear. If dimensions of an object are much smaller than the wavelength of the incident electromagnetic radiation, the EM problem can be accurately treated within the quasi-static limits [2, 3, 9]. Under this limit, the phase of the harmonically oscillating EM field is almost uniform over the particle volume (see Fig. 1.4(a)). So, one can consider problem such that a particle is immersed in an electrostatic field. The electric fields, in this scenario can be related to the scalar electric potential, denoted by ϕ, [2, 3] as $\mathbf{E} = -\nabla\phi$.

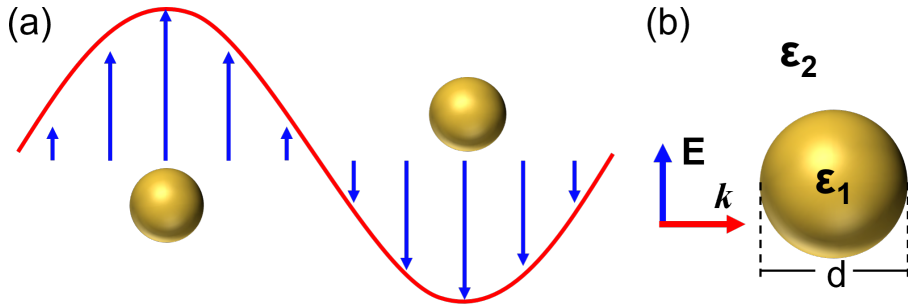

Fig. 1.4 (a) Illustration of an object's excitation with an electromagnetic field under quasi-static limits and (b) the EM field incident on a sphere of diameter d.

Consider a homogeneous isotropic spherical nano-particle of diameter d placed in a uniform static electric field having amplitude E_0 such that $\mathbf{E} = E_0\hat{z}$. The surrounding medium of the sphere is a nonabsorbing isotropic dielectric with permittivity ε_2, and the particle itself is described by a complex valued dielectric constant ε_1 defined using Eq. (1.6) (see Fig. 1.4(b)). The scalar electric potential for a sphere immersed in an electrostatic field is the solution to Laplace's equation such that $\nabla^2\phi = 0$. The relation for the electric potential in the surrounding of the sphere is the following [2, 3]:

$$\phi = -E_0 r cos\theta + \frac{\mathbf{p}\cdot\mathbf{r}}{4\pi\varepsilon_0\varepsilon_1 r^3}, \tag{1.10a}$$

$$\mathbf{p} = 4\pi\varepsilon_0\varepsilon_1 a_0^3 \frac{\varepsilon_2 - \varepsilon_1}{\varepsilon_2 + \varepsilon_1}\mathbf{E}. \tag{1.10b}$$

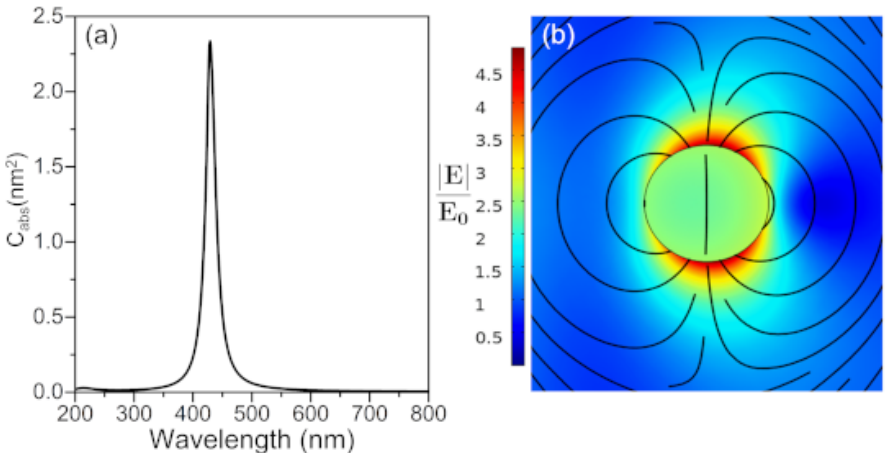

Fig. 1.5 EM scattering from a metallic nanosphere of 60 nm diameter (a) the absorption efficiency and (b) electric field distribution; black lines show the scattered EM field from the sphere.

In the above Eq. (1.10) the $a_0 = \frac{d}{2}$ is the radius of the spherical particle, and **p** is the dipole moment which is proportional to the electric field inside the sphere. Using the expression for **p**, one can define the polarizability of a sub-wavelength sphere of radius a_0 as [2, 3, 9]:

$$\alpha = 4\pi a_0^2 \frac{\varepsilon_2 - \varepsilon_1}{\varepsilon_2 + \varepsilon_1}. \tag{1.11}$$

From the Eq. (1.11) it can be deduced that the polarizability can undergo a resonant enhancement, giving rise to *localized surface plasmon resonances* (LSPRs) [2, 3]. The characteristics LSPRs excitation in a nanosphere are the following:

- The excitation of LSPRs results in the enhancement of the absorption and scattering cross-section of the sphere defined as:

$$C_{abs} = kIm[\alpha] = 4\pi k a_0^4 \left[\frac{\varepsilon_2 - \varepsilon_1}{\varepsilon_2 + \varepsilon_1}\right], \tag{1.12a}$$

$$C_{sca} = \frac{k^4}{6\pi}|\alpha|^2 = \frac{8\pi}{3}k^4 a_0^6 \left[\frac{\varepsilon_2 - \varepsilon_1}{\varepsilon_2 + \varepsilon_1}\right]^2, \tag{1.12b}$$

  with $k = 2\pi/\lambda$. It can bee seen from the Eq. (1.12) that for smaller particles (i.e., $a_0 << \lambda$) the absorption cross-section C_{abs} dominates, however, with increasing particles' sizes the scattering cross-section C_{sca} becomes more pronounced.

- The resonant position (wavelength) is highly dependent on the material parameters of the nanoparticle system as well as the physical dimensions of the scatter, as deduced form Eq. 1.11.
- LSPR has features such as confinement of light within a nanometer regions around the sphere and a large electric field produced at the LSPR condition (see Fig. 1.5(b)).
- LSPR excites for a narrow spectral range (see Fig. 1.5(a)). However, such a resonant response has its own implications, to be introduced in section 1.1.2

The systems supporting LSPR are generally referred to as *optical nanoanetnnas*. In the next section, we will discuss some of their interesting properties.

1.1.2 Nanoantennas

Localized surface plasmon resonance (LSPR) supported by noble metal nanoparticles make them excellent absorbers and scatterers in the visible spectrum, ideal for a variety of nanophotonic applications. Indeed, the large electric fields induced in the proximity of the particle due to the excitation of LSPRs can significantly enhance light-matter interactions [2, 15]. Nanoantennas offer opportunities for efficient conversion of propagating free-space light into highly localized and confined optical fields at the nanoscale, and the other way around [16]. Nanoantennas have shown their potential in a range of optical applications, which we will briefly discuss in the following paragraphs. For a broad overview on modeling and characterization of such nanodevices, we refer the monograph by Agio and Alu [17].

The use of nanoantennas spans through a wide range of applications. It is possible to use arrays of nanoantennas to achieve, for example, imaging, realized through the spectrally well-designed LSPRs [18]. Plasmonic nanoantennas supporting Fano-like resonances find their applications to enhance higher-order multipolar radiative transitions. Optical counterparts to radio-frequency antennas have enabled the strong directivity in the scattered angular intensity, as well as optical designs that offer the possibility of forward/backward anisotropic scattering and wavelength-dependent switching of directionality [19]. Similarly, distinct designs allow for the polarization conversion and polarization-sensitivity or -insensitivity [20, 21]. Acoustic vibrations can be optically excited in nanoparticles, used as nano-sources for hyper sound generation [22].

Nanoantennas are also used for surface-enhanced spectroscopy. The underlying phenomenon in such a process exploits plasmonic field enhancements to boost signals from few or even single molecules [19]. For biomedical applications, plasmonic nanoparticles play a crucial role in the development of nano biosensors for specific biomolecules or as biomarkers for local thermal treatment and drug delivery [23]. Optomechanical plasmonic resonators can utilize spectrally narrow resonances offered by nanoantennas for tuning and sensing applications [24]. Lately, researchers have explored the utility of a periodic array of the plasmonic antenna as an ideal optical absorber [25]. Such a design have lead to the realization of designs like selective emitters, sensors, and spatial light modulators [26–28].

1.1.3 Plasmonic waveguides

The subwavelength confinement associated with the SPPs and their propagation along the guide offers opportunities for plasmonic waveguides (PWs) [13, 14, 29]. In this section, we will briefly discuss some applications of PWs. For a complete review on the subject we refer the reader to Ref. 12 and Ref. 30.

With the ever-decreasing sizes and the ever-increasing processing capabilities of modern electronic devices, the need for efficient and high-speed links to carry information is ubiquitous. All-optical (silicon/dielectric-based) interconnects, capable of handling high-speed communications, has been an attractive solution in that regard [31]. However, due to their diffraction-limited operations, the miniaturization of such optical components to the sizes of current electronic devices is not possible. On the contrary, the integration of plasmonic components (waveguides/couplers) into subwavelength systems for information processing/exchange has been emerged as a viable solution [13, 14]. A collection of PW-based counterparts of conventional digital/electronic elements has been conceived. These include devices like plasmonic nanolasers/modulators, optical digital-gates, routers, photon-electric converters, control switches, and devices such as Mach-Zehnder Interferometers (MZIs) [32]. Moreover, plasmonic waveguides demonstrate several quantum optical phenomena like single-photon emission, the SPPs enabled coupling of two emitters for applications in controlling of superradiance of emitter-pairs, and qubit-qubit entanglement generation [33, 34]. SPPs confinement at the metal surface has proven instrumental for realizing the biosensors with improved sensing capabilities. PW-based biosensors find their role in various medical applications such as the early-stage disease detec-

tion and measurement of blood glucose and blood hemoglobin [35, 36]. Another application of plasmonic waveguide is the near field scanning optical microscopy (NSOM), which is an effective tool in investigation of nanoscale light-matter interaction. Plasmonic NSOM probes are capable of confining high density of light to sub-nanometer spots, useful in high-density data storage, molecular trapping, nanolithography, and nano spectroscopy [37].

1.1.3.1 Modes orthogonality in optical waveguide

For distinct modes m and n of any arbitrary z-directed waveguide, the electromagnetic fields takes the form:

$$\mathbf{E}_{(m,n)}(x,y,z) = \tilde{\mathbf{E}}_{(m,n)}(x,y)exp(i\kappa_{(m,n)}z) \tag{1.13a}$$

$$\mathbf{H}_{(m,n)}(x,y,z) = \tilde{\mathbf{H}}_{(m,n)}(x,y)exp(i\kappa_{(m,n)}z) \tag{1.13b}$$

with $\kappa_{(m,n)}$ being propagation constants of the modes m and n, respectively and $\{\tilde{\mathbf{E}}_{(m,n)}(x,y), \tilde{\mathbf{H}}_{(m,n)}(x,y)\}$ are the fields in the transverse direction. The orthogonality between the modes of the waveguide states that, for $m \neq n$ [38, 39]:

$$\int_S (\tilde{\mathbf{E}}_m \times \tilde{\mathbf{H}}_n^*) \cdot \hat{z}\, dS = 0.. \tag{1.14}$$

In Eq. (1.14) the quantities $\tilde{\mathbf{E}}_m$,$\tilde{\mathbf{H}}_m$ are the transverse vector fields (throughout the discussion in this section, the tilde vectors shall represent the fields transverse to the direction of propagation), * denote the conjugate operation, S is the cross-sectional plane, and $\hat{z}$ is the unit vector normal to it. Eq. (1.14) states that there is no power exchanged between fields of different modes [38]. This power orthogonality property, however, is valid for lossless waveguides [38–40]. The expression for the generalized orthogonality between the waveguide modes [38–40] is:

$$\int_S (\tilde{\mathbf{E}}_m \times \tilde{\mathbf{H}}_n) \cdot \hat{z}\, dS = 0. \tag{1.15}$$

Note that this relation is still valid only for the waveguides composed of isotropic material [38–40].

Proof of the generalized orthogonality

The following proof of the Eq. (1.15) is based on the assumption that there is no outward flux fields from the side walls of the waveguide. Maxwell's curl equations (i.e., Eq. (1.1a) and Eq. (1.1b)) for the time-harmonic fields the modes m and n result in:

$$\nabla \times \mathbf{E}_m = -j\omega\mu\mathbf{H}_m \tag{1.16a}$$

$$\nabla \times \mathbf{H}_m = j\omega\varepsilon\mathbf{E}_m + \mathbf{J}_m \tag{1.16b}$$

$$\nabla \times \mathbf{E}_n = -j\omega\mu\mathbf{H}_n \tag{1.16c}$$

$$\nabla \times \mathbf{H}_n = j\omega\varepsilon\mathbf{E}_n + \mathbf{J}_n \tag{1.16d}$$

Combining these equations and utilizing the vector identity $\nabla \cdot (\mathbf{A} \times \mathbf{B}) = \mathbf{B} \cdot (\nabla \times \mathbf{B}) - \mathbf{A} \cdot (\nabla \times \mathbf{B})$ give:

$$\nabla \cdot (\mathbf{E}_m \times \mathbf{H}_n - \mathbf{E}_n \times \mathbf{H}_m) = \mathbf{J}_m \cdot \mathbf{E}_n - \mathbf{J}_n \cdot \mathbf{E}_m$$

which for a sourceless media, i.e., for the vanishing right-hand side of the above expression results in:

$$\nabla \cdot (\mathbf{E}_n \times \mathbf{H}_m - \mathbf{E}_m \times \mathbf{H}_n) = 0. \tag{1.17}$$

Integrating both side of Eq. (1.17) over the volume bounded by two cross-sections at $z = z_1$ and $z = z_1 + dz$ (see Fig. 1.6) and making use of the Gauss' theorem yields [38–40]:

$$\int_\Omega \nabla \cdot (\mathbf{E}_n \times \mathbf{H}_m - \mathbf{E}_m \times \mathbf{H}_n)\, dV = \int_A (\mathbf{E}_n \times \mathbf{H}_m - \mathbf{E}_m \times \mathbf{H}_n) \cdot \hat{n}\, dA. \tag{1.18}$$

Where A is the surface closing the chosen volume Ω. With our initial assumption of fields' flux through the side walls being zero, and making use of the Divergence Theorem [38, 39], the Eq. (1.18) reduces to:

$$\left(\frac{\partial}{\partial z}\right) \int_S (\mathbf{E}_n \times \mathbf{H}_m - \mathbf{E}_m \times \mathbf{H}_n) \cdot \hat{z}\, dS = 0. \tag{1.19}$$

with integration taken over the cross-sectional area denoted by S (see Fig. 1.6). The Eq. (1.19) is what known as the *Lorentz Reciprocity Theorem* [38–40] for media with its characteristics invariant along the $z-$direction.

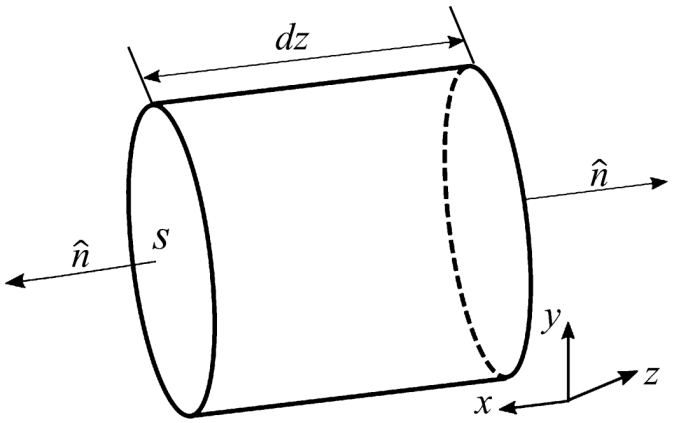

Fig. 1.6 A differential length of an arbitrary shape (not necessarily a cylindrical) waveguide.

Substituting the forms of fields for modes m and n from Eq. (1.13) back in Eq. (1.19), and employing the differential operator $\frac{\partial}{\partial z}$ yields:

$$(\kappa_n + \kappa_m) \int_S \left(\tilde{\mathbf{E}}_n \times \tilde{\mathbf{H}}_m - \tilde{\mathbf{E}}_m \times \tilde{\mathbf{H}}_n\right) \cdot \hat{z}\, dS = 0. \tag{1.20}$$

which shows that unless $\kappa_n = -\kappa_m$

$$\int_S \left(\tilde{\mathbf{E}}_n \times \tilde{\mathbf{H}}_m - \tilde{\mathbf{E}}_m \times \tilde{\mathbf{H}}_n\right) \cdot \hat{z}\, dS = 0 \tag{1.21}$$

Now if one consider the mode m is left unchanged, while the mode n is taken to be the a reflected modes, i.e., $\kappa_n = -\kappa_n$, then from Maxwell's equation $\tilde{\mathbf{H}}_n$ also flips its sign if $\tilde{\mathbf{E}}_n$ is kept unchanged. Under this new scenario the Eq. (1.19) becomes:

$$(\kappa_n - \kappa_m) \int_S \left(\tilde{\mathbf{E}}_n \times \tilde{\mathbf{H}}_m + \tilde{\mathbf{E}}_m \times \tilde{\mathbf{H}}_n\right) \cdot \hat{z}\, dS = 0. \tag{1.22}$$

which again shows that unless $\kappa_n = \kappa_m$

$$\int_S \left(\tilde{\mathbf{E}}_n \times \tilde{\mathbf{H}}_m + \tilde{\mathbf{E}}_m \times \tilde{\mathbf{H}}_n\right) \cdot \hat{z}\, dS = 0 \tag{1.23}$$

Adding the Eq. (1.21) and Eq. (1.23), and considering that $\kappa_n \pm \kappa_m$, we obtain:

$$\int_S \left(\tilde{\mathbf{E}}_n \times \tilde{\mathbf{H}}_m\right) \cdot \hat{z}\, dS = 0 \tag{1.24}$$

The Eq. (1.23) and Eq. (1.24) are the mode's orthogonality relations, extensively used in excitation and scattering problems of the waveguide. In rearranged forms,

these equations can be written as:

$$\int_S \left(\tilde{\mathbf{E}}_n \times \tilde{\mathbf{H}}_m + \tilde{\mathbf{E}}_m \times \tilde{\mathbf{H}}_n\right) \cdot \hat{z}\, dS = 2N_n \delta_{(n,m)} \tag{1.25a}$$

$$\int_S \left(\tilde{\mathbf{E}}_n \times \tilde{\mathbf{H}}_m\right) \cdot \hat{z}\, dS = N_n \delta_{(n,m)} \tag{1.25b}$$

$$N_n = 2 \int_\Omega \left(\tilde{\mathbf{E}}_n \times \tilde{\mathbf{H}}_n\right) \cdot \hat{z}\, dS \tag{1.25c}$$

and $\delta_{(n,m)} = 1$ only if the $n = m$; otherwise it is equal to zero [39]. Note that contrarily to the orthogonality relation of Eq. (1.14), N_n does not represent the power carried by the n-th mode.

Modal expansion of the fields in a waveguide

Once the orthogonality between distinct modes in a waveguide have been established, we can expand an arbitrary field distribution over the guide's cross-section in terms of its modes. Consider the transverse electric field $\mathbf{E}_t(0)$ over the cross-section $z = 0$ excites the waveguide. The expansion of the transverse field at any point along the guide, in terms of the excited modes, is the sum defined as:

$$\mathbf{E}_t(z) = \sum_n a_n \tilde{\mathbf{E}}_n exp(i\kappa_n z) \tag{1.26}$$

where the a_ns are the excitation coefficients of each mode [39]. If $\mathbf{E}_t(0)$ is known, the Eq. (1.26) can be written as:

$$\mathbf{E}_t(0) = \sum_n a_n \tilde{\mathbf{E}}_n$$

multiplying the above expression by $\tilde{\mathbf{H}}_n$ and using the orthogonality relation from Eq. (1.25b), the excitation coefficient a_n can be obtained as:

$$a_n = \frac{1}{N_n} \int_S (\mathbf{E}_t(0) \times \tilde{\mathbf{H}}_n) \cdot \hat{z} dS \tag{1.27}$$

Likewise, the duality of the EM fields yields an alternative for obtaining the excitation coefficients in terms of the magnetic fields as:

$$a_n = \frac{1}{N_n} \int_S (\tilde{\mathbf{E}}_n \times \mathbf{H}_t(0)) \cdot \hat{z} dS \tag{1.28}$$

These relations are valid if the backward propagating modes are neglected.

On the contrary, backward propagating modes cannot be neglected, both the transverse electric and magnetic fields at $z = 0$ are needed to determine the field expansion. In this case, the transverse electric and magnetic fields in a waveguides expanded in terms of the modal fields are:

$$\mathbf{E}_t(z) = \sum_n a_n \tilde{\mathbf{E}}_n exp(i\kappa_n z) + b_n \tilde{\mathbf{E}}_n exp(-i\kappa_n z), \tag{1.29a}$$

$$\mathbf{H}_t(z) = \sum_n a_n \tilde{\mathbf{H}}_n exp(i\kappa_n z) - b_n \tilde{\mathbf{H}}_n exp(-i\kappa_n z). \tag{1.29b}$$

where, in the above expressions, the terms with multiplication factor $exp(-i\kappa_n z)$ are the reflected modes, present in the guide due to any type of discontinuities. Substituting $z = 0$, multiplying the Eq. (1.29a) by $\tilde{\mathbf{H}}_m$ and Eq. (1.29b) $\tilde{\mathbf{E}}_m$, integrating over the cross section, and using the orthogonality relationship Eq. (1.25b) yields:

$$\int_S (\mathbf{E}_t(0) \times \tilde{\mathbf{H}}_m) \cdot \hat{z} dS = (a_m + b_m) N_m, \tag{1.30a}$$

$$\int_S (\tilde{\mathbf{E}}_m \times \mathbf{H}_t(0)) \cdot \hat{z} dS = (a_m - b_m) N_m. \tag{1.30b}$$

Solving the Eq. (1.30) for the a_m and b_m, we obtain:

$$a_m = \frac{1}{2N_m} \int_S (\mathbf{E}_t(0) \times \tilde{\mathbf{H}}_m + \tilde{\mathbf{E}}_m \times \mathbf{H}_t(0)) \cdot \hat{z} dS, \tag{1.31a}$$

$$bm = \frac{1}{2N_m} \int_S (\mathbf{E}_t(0) \times \tilde{\mathbf{H}}_m - \tilde{\mathbf{E}}_m \times \mathbf{H}_t(0)) \cdot \hat{z} dS. \tag{1.31b}$$

which is general expression for modal excitation by known aperture fields [39, 41].

These orthogonality properties will be used in chapter 3, where we will derive a generalized formulation to calculate second-harmonic generation in plasmonic waveguides.

1.2 Plasmonics for nonlinear optics

Nonlinear optics is a growing field, and nonlinear optical phenomena are at the core of many emerging technologies from optical signal processing, to optical

computers, ultrafast switches, ultra-short pulsed lasers, sensors, laser amplifiers, and many others [42, 43]. Nevertheless, nonlinear optical systems rely on bulkier components[42, 43], which hinder their integration with modern-day devices of miniaturized scales [5, 14, 44]. Moreover, *conventional* nonlinear optical systems require a high rate of power consumption to generate nonlinear effects of practical significance [43]. On the other hand, plasmonic designs possess nanoscale footprints, and the localized field enhancement associated with plasmonic modes could lead in the context of nonlinear optics to lower power consumption [5, 44]. In this section, we present plasmonic systems' application for nonlinear optics. First, we review the main principles of nonlinear optics, paying particular attention to the second-harmonic generation process, and later discuss some applications in nonlinear plasmonics.

1.2.1 Basics of nonlinear optics

Nonlinear optical phenomena arise when the electromagnetic response of a material system is no longer proportional to the amplitude of applied EM fields. Typically, these phenomena are only observable by employing laser light, which is sufficiently intense to induce a nonlinear optical response in the material and generate the corresponding effects. Following the discovery of laser by Maiman [45], seminal works on nonlinear optics are the study of the second-harmonic generation process by Franken et al., and Bloembergen and Pershan in 1960's [46, 47]. Lasers have physical characteristics of being monochromatic, coherent, and squeezing light to areas as small as a few hundreds of square microns. As a result, it is possible to obtain electrical fields associated with the propagating waves, comparable to those inside atoms that can induce local modifications in the material composition to induce the nonlinear responses [42].

Nonlinear polarization and electromagnetic formulation of nonlinear interactions

In order to describe the meaning of optical nonlinearity, let us consider Eq. (1.4a), i.e., how the polarization $\mathbf{P}$ of a material system depends upon the strength of the electric field $\mathbf{E}$. For the nonlinear optics, polarization can be generalized for a power

series of the electric field intensity as follows:

$$P(t) = \varepsilon_0 \left[\chi^{(1)} E(t) + \chi^{(2)} E^2(t) + \chi^{(3)} E^3(t) \dots \right] \tag{1.32}$$

where $\chi^{(1)}$ is equal to χ in Eq. (1.4a), i.e., the linear susceptibility, while $\chi^{(2)}$ and $\chi^{(3)}$ are known as second- and third-order nonlinear optical susceptibilities, respectively. Distinct physical processes arises due to a second- and third-order polarization [42]. In general, quantities describing material properties ($\chi^{(s)}$) are tensors [42]. For condensed matter $\chi^{(1)}$ is of the order of unity, $\chi^{(2)}$ is of the order of 10^{-12} m/V and $\chi^{(3)}$ is 10^{-21} m^2/V^2, such that the 12 and 21 orders of magnitude of difference is with respect to linear susceptibility. It is, therefore, evident why sufficiently intense electromagnetic radiations such as the lasers can only excite the nonlinear effects. Note that in the writing of Eq. (1.32), the assumption is that the response time of the mediums to an EM excitation is instantaneous, i.e., the interaction time between the electric field oscillations and the bound electrons in the atoms is very short.

From simple constraints on the symmetry of the material's response to the external electric field, it can be shown that the second-order nonlinear optical interactions of the second-order can occur only in non-centrosymmetric materials [1]. Consequently, second-order susceptibility vanishes in liquids, gases, and amorphous solids, and these materials cannot produce nonlinear second-order optical interactions. Nonlinearities of the third order, on the other hand, can arise both from centrosymmetric means as well as non-centrosymmetric material systems [42].

At this point it is appropriate to ask how polarization contribute to the generation of nonlinear optical effects. The reason is related to the fact that a time-varying polarization field can act as a source of new components of the electromagnetic field.

[1] In a centrosymmetric crystal, change in the sign of the electric field also changes the sign of the polarization. This implies that a relation between the polarization and electric fields as for which one has:

$$-\mathbf{P}^{(2)} = \chi^{(2)}(-\mathbf{E})(-\mathbf{E})$$

comparing the above equation with Eq. (1.32) we obtian:

$$\mathbf{P}^{(2)} = -\mathbf{P}^{(2)}$$

which is satisfied only if the $\mathbf{P}^{(2)} = 0$ and so, $\chi^{(2)} = 0$.

To elaborate, consider the general form of the wave equation:

$$\nabla \times \nabla \times \mathbf{E} + \mu_0 \frac{\partial^2}{\partial t^2} \mathbf{D} = 0 \tag{1.33}$$

which can be derived from Eqs. (1.1-1.2) after some vector algebraic manipulation [42]. Taking in to account the Eq. (1.32), material's electric displacement field can be expanded as: $\mathbf{D} = \varepsilon_0 \mathbf{E} + \mathbf{P}^{(1)} + \mathbf{P}^{\mathrm{NL}}$. The Eq. (1.33) can be rearranged then:

$$\nabla \times \nabla \times \mathbf{E} + \mu_0 \frac{\partial^2}{\partial t^2} (\varepsilon_0 \mathbf{E} + \mathbf{P}^{(1)}) = -\mu_0 \frac{\partial^2}{\partial t^2} \mathbf{P}^{\mathrm{NL}}$$

In the above expression, the term $\varepsilon_0 \mathbf{E} + \mathbf{P}^{(1)}$ is proportional to linear electric induction $\mathbf{D}^{(1)}$, so the above expression can be rewritten as:

$$\nabla \times \nabla \times \mathbf{E} + \mu_0 \frac{\partial^2}{\partial t^2} \mathbf{D}^{(1)} = -\mu_0 \frac{\partial^2}{\partial t^2} \mathbf{P}^{\mathrm{NL}} \tag{1.34}$$

We can interpret the Eq. (1.34) as inhomogeneous vector wave equation in which the polarization $\mathbf{P}^{\mathrm{NL}}$ associated with the nonlinear response of the medium drives the electric field. The governing physics can be interpreted on the following arguments. The polarization induced is a consequence of separation of charges within the material. The second-order time derivative of $\mathbf{P}^{\mathrm{NL}}$ is, thus, a measure of the acceleration of the charges within the medium. This is a well-known fact in classical electromagnetism that accelerated charges generate electromagnetic radiations [42].

Second-order nonlinear optical processes and second-harmonic generation

Let us consider a nonlinear material having the non-zero susceptibility of the second-order, which contains an optical field consisting of two distinct frequency components:

$$E(t) = E_1(t) e^{i\omega_1 t} + E_2(t) e^{i\omega_2 t} + c.c \tag{1.35}$$

where c.c. represents the complex conjugate of the fields. Considering the Eq. (1.32), the nonlinear polarization of the medium can be written as:

$$P^{(2)}(t) = \varepsilon_0 \chi^{(2)} E^2(t)$$

substituting the Eq. (1.35) in the above expression yields:

$$\begin{aligned} P^{(2)}(t) =& \varepsilon_0 \chi^{(2)} \left[E_1(t) e^{i\omega_1 t} + E_2(t) e^{i\omega_2 t} + c.c \right]^2 \\ =& \varepsilon_0 \chi^{(2)} (E_1^2 e^{-2i\omega_1 t} + E_2^2 e^{-2i\omega_2 t} + 2E_1 E_2 e^{-i(\omega_1+\omega_2)t} + \\ & 2E_1 E_2 e^{-i(\omega_1-\omega_2)t} + c.c) + 2\varepsilon_0 \chi^{(2)} (E_1 E_1^* + E_2 E_2^*). \end{aligned}$$

From the expression above, we can observe that the nonlinear polarization of the second-order is a series of contributions at different frequencies. According to the Eq. (1.34), each of the contribution can lead to the generation of electromagnetic radiation at the corresponding frequency. The complex amplitudes of different components of the polarization at each frequency are given by:

$$\begin{aligned} P(2\omega_1) =& \varepsilon_0 \chi^{(2)} E_1^2 && \text{(SHG)} \\ P(2\omega_2) =& \varepsilon_0 \chi^{(2)} E_2^2 && \text{(SHG)} \\ P(\omega_1+\omega_2) =& 2\varepsilon_0 \chi^{(2)} E_1 E_2 && \text{(SFG)} \\ P(\omega_1-\omega_2) =& 2\varepsilon_0 \chi^{(2)} E_1 E_2^* && \text{(DFG)} \\ P(0) =& 2\varepsilon_0 \chi^{(2)} (E_1 E_1^* + E_2 E_2^*) && \text{(OR)} \end{aligned} \tag{1.36}$$

The polarization components in Eq. (1.36) are labeled with the name of the physical processes to which they contribute: optical Second-Harmonic Generation (SHG), the Sum-Frequency Generation (SFG), Difference-Frequency Generation (DFG), and finally the optical rectification (OR). The polarization component that lead to the optical rectification process does generate the electromagnetic radiation. In fact, its second derivative is zero. However, in this process a static electric field is produced through the nonlinear source. Finally, note that, according to the complex notation, for each of the non-zero frequencies, there will be a corresponding contribution to the same frequency changed in sign. However, it is not necessary to explicitly indicate all these contributions as they are simply the complex conjugate of those in the list above [42].

Form Eq. (1.36), we see that nonlinear polarization has four non-zero frequency components. Nonetheless, no more than one of the frequency components will be usually available with noticeable intensity in the radiation generated during the nonlinear optical interactions. In the case of nonlinear optical crystals, we can link this aspect to satisfying certain *Phase-Matching* conditions (to be introduced in the next section). Operationally, the nonlinear crystal's orientation and the input

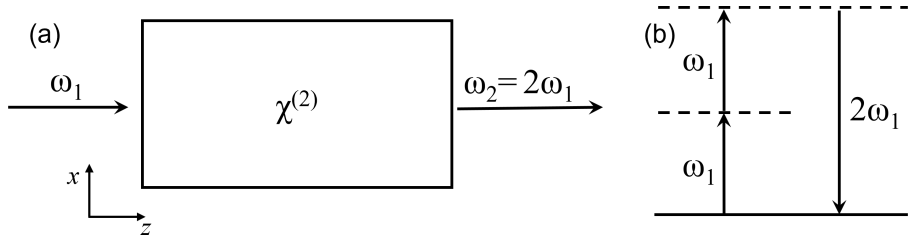

Fig. 1.7 (a) the schematic illustration and (b) the energy-level diagram of the SHG process.

radiation's polarization determine the excited frequency component of the nonlinear polarization [42]. For nanostructures, the excitation of the nonlinear polarization depends on the spectral and spatial characteristics of the resonances supported by the structure and its overlap with the orientation of the nonlinear crystal. We will expand on this fact in chapter 2.

1.2.1.1 Second-Harmonic Generation

It is difficult to generate laser emissions in the short-wavelength part of the visible and near-visible range of the EM spectrum. Nonlinear optical frequency mixing, on the other hand, enables the generation of new short wavelengths from the existing lasers. In the second-harmonic generation (SHG) process, an input frequency passes through a nonlinear crystal to generate light twice the input frequency. The first experimental demonstration of the SHG, at the optical frequencies, goes back to 1961 by Franken et al., [46]. The study revealed that focusing a ruby laser of wavelength ($\lambda = 694$ nm) on a crystalline quartz plate generated optical radiations at twice the input frequency (i.e., at $\lambda = 347$ nm).

Let us consider Fig. 1.7 for a schematic visualization of the SHG. Fig. 1.7(a) illustrates the process: an illumination of frequency ω_1 on a medium with a second-order nonlinear response generates the radiation, which is twice the frequency of the illumination. Fig. 1.7(b) describes the SHG process in terms of the photonic interactions. It shows the annihilation of two photons of frequency ω_1 resulted in the creation of a photon at frequency $2\omega_1$ during a quantum-mechanical process [48]. Note that in Fig. 1.7(b), the solid line represents eigenstates of the atom with a distinct energy value. In comparison, the dashed lines indicate those which are known as the virtual energy levels. The energy of the virtual levels is equal to the energy of the radiant fields [42].

We now present analytical description of the SHG process in a nonlinear crystal [42]. For the time-harmonic fields, the Eq. (1.34) can be rewritten as:

$$\nabla \times \nabla \times \mathbf{E} - \varepsilon_r k_0^2 \mathbf{E} = -\mu_0 \omega^2 \mathbf{P}^{\mathrm{NL}} \tag{1.37}$$

where we have considered $\mathbf{D}^{(1)} = \varepsilon_0 \varepsilon_r \mathbf{E}$ which is the linear polarization of the crystal and $k_0 = \omega\sqrt{\mu_0 \varepsilon_0}$. Considering crystal's second-order nonlinear response $\chi^{(2)}$, ω_1 and $\omega_2 = 2\omega_1$ representing the fundamental (FF) and second-harmonic (SH) frequencies, respectively; using the Eq. (1.36) then yields the nonlinear polarization with the following frequency components:

$$\mathbf{P}^{\mathrm{NL}} = \varepsilon_0 \chi^{(2)} \mathbf{E}^2 \Longrightarrow \begin{cases} \mathbf{P}^{\mathrm{NL}}_{\omega_1} = 2\varepsilon_0 \chi^{(2)} \mathbf{E}^*_{\omega_1} \mathbf{E}_{\omega_2} \\ \mathbf{P}^{\mathrm{NL}}_{\omega_2} = \varepsilon_0 \chi^{(2)} \mathbf{E}^2_{\omega_1} \end{cases}$$

Utilizing the forms of the polarization defined above, the wave equation at each frequency can be defined as:

$$\nabla^2 \mathbf{E}_{\omega_1} + k_1^2 \mathbf{E}_{\omega_1} = -2\mu_0 \omega_1^2 \chi^{(2)} \mathbf{E}^*_{\omega_1} \mathbf{E}_{\omega_2} \tag{1.38a}$$

$$\nabla^2 \mathbf{E}_{\omega_2} + k_2^2 \mathbf{E}_{\omega_2} = -4\mu_0 \omega_1^2 \chi^{(2)} \mathbf{E}^2_{\omega_1} \tag{1.38b}$$

where $k_1 = \frac{n(\omega_1)\omega_1}{c}$, $k_2 = \frac{n(\omega_2)\omega_2}{c}$. In the expression for $k_{1/2}$, the $n(\omega_{1/2}) = \sqrt{\varepsilon_r(\omega_{1/2})}$ is the refractive index of material at the fundamental and the SH frequency, respectively.

For a one-dimensional problem (along z, for the system considered in Fig. 1.8), the solution to the Eq. 1.38 in the form of plane waves $\tilde{\mathbf{E}}_1(z) = A_1 e^{-ik_1 z}$ at the ω_1 and $\tilde{\mathbf{E}}_2(z) = A_2 e^{-ik_2 z}$ at ω_2 yield:

$$\frac{dA_1}{dz} = -i\frac{\mu_0}{k_1^2} \omega_1^2 \chi^{(2)} A_1^* A_2 e^{-i\Delta k z} \tag{1.39a}$$

$$\frac{dA_2}{dz} = -i\frac{2\mu_0}{k_2^2} \omega_1^2 \chi^{(2)} A_1^2 e^{-i\Delta k z} \tag{1.39b}$$

where $\Delta k = k_2 - 2k_1$, and $A_{1/2}$ are constants amplitudes of the plane waves. It is wroth mentioning that derivation of the Eq. 1.39 is carried out under the slowly varying envelope approximation, i.e., $\frac{d^2 A_{1/2}}{dz^2} << k_{1/2} \frac{dA_{1/2}}{dz}$. Fig. 1.8(a) renders the finite element simulation of SHG through a lossless and isotropic nonlinear crystal.

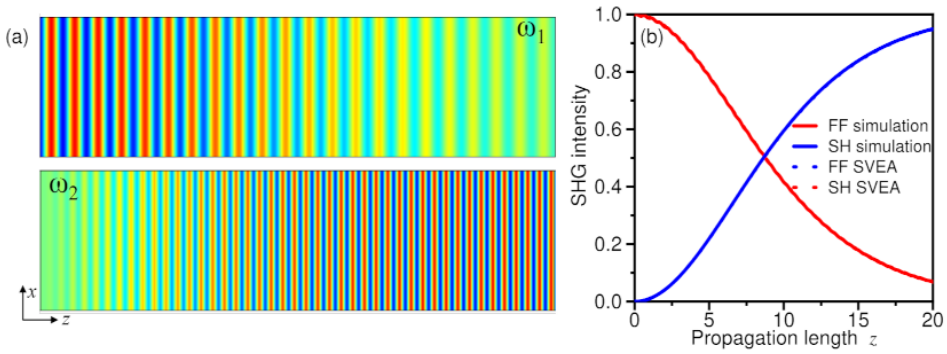

Fig. 1.8 SHG through a nonlinear crystal: (a) Finite element simulation of the SHG process and (b) the normalized second-harmonic intensity versus the propagation distance z and its comparison.

Trends show that the amplitude for the SH builds up along the length of the crystal. Fig. 1.8(b) provides a comparison of the calculated intensity with the analytical solution of the Eq. (1.39). The reason for the FF field's decay during propagation along the crystal in (see Fig. 1.8) is that in our simulations, we have considered that the input beam loses energy to the converted SH beam. In most experimental conditions, however, the power lost by the input beam due to the conversion to the SH frequency remained negligible, i.e., $dA_1/dz = 0$ in Eq. (1.39). This assumption is formally known as the *undepleted pump approximation*. Throughout the draft, we will operate under this assumption. Note here that for the trends presented in Fig. 1.8, we have considered the refractive indices of the material at the interaction wavelengths in the SHG process are identical, i.e., $n_{\omega_1} = n_{\omega_2}$ or $\Delta k = 0$ in Eq. (1.39). In most practical scenarios, this consideration is not valid due to the dispersive nature of the matter, however. In the following we detail about the consequences of the $\Delta k \neq 0$ on the second-harmonic generation.

Phase-matching condition in SHG process

The Eq. 1.39 shows that the energy transfer between the FF field and the generated SH can be maximized only if $\Delta k = 0$ or $k_2 = 2k_1$. In the vector form:

$$\mathbf{k}_2 = 2\mathbf{k}_1 \tag{1.40}$$

the above expression is known as the perfect phase-matching condition for the SHG process. The physical interpretation of the phase-matching is that the linear

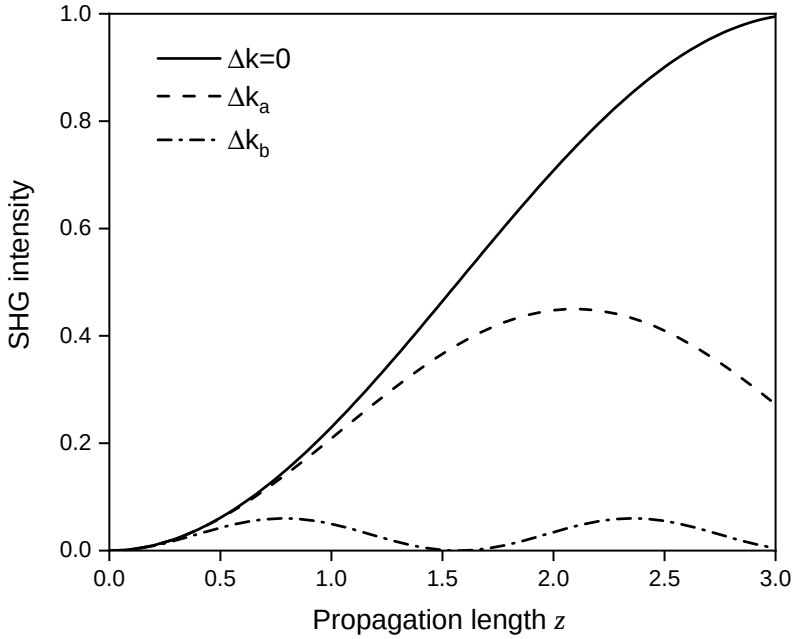

Fig. 1.9 Illustration of SHG intensity's variation for different values of Δk against the propagation distance z.

momentum between the interacting fundamental and the generated harmonic fields must remain conserved. As a direct consequence of the Eq. (1.40), the SHG conversion efficiency increases *proportionally* to the propagation length squared, as shown in the Fig. 1.8(b). The non-phase matched operation, i.e., $\Delta k \neq 0$, results in a drastic decrease in the SHG conversion efficiency. Under this operation, the SHG wave generated at point p_1 along crystal length, propagating to another point p_2, is out of phase with the second-harmonic wave at the p_2. The resultant interference of the non-phase matched SHG is described by the factor $L^2 sinc^2(\Delta kL/2)$ in Eq. (1.40), where L is the length along the crystal. Fig. 1.9 presents the normalized SHG intensity for varying values of the Δk, such that $\Delta k_b > \Delta k_a$. A trade-off between the maximum generated intensity and the propagation length is apparent. One half of the distance that divides the two neighboring peaks of SHG interference pattern is called the coherence length, defined as [42]:

$$L_{coh} = \frac{2}{\Delta k}$$

The coherence length L_{coh} stands for the maximum crystal length that is useful in producing the second-harmonic power. Based on the mismatch between the effective

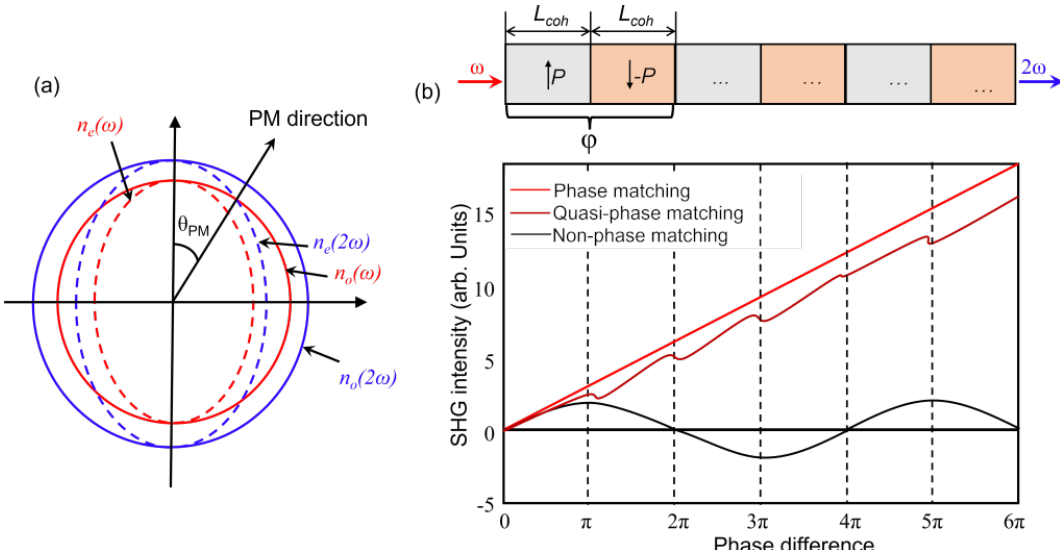

Fig. 1.10 Schematic illustration of the phase-matching techniques: (a) the birefringent phase-matching condition in a negative uniaxial crystal ($n_e < n_o$) and (b) the quasi-phase-matching using a periodically poled nonlinear material.

refractive indices of the crystal, which is typically of the order of 10^{-1} to 10^{-2} at the interaction wavelengths of the SHG, the maximum coherence lengths are usually a few wavelengths.

Phase-matching techniques

In the earlier section, we have emphasized that phase-matching is necessary for an efficient SHG process. Various techniques have been adopted over the years to fulfill the phase-matching conditions. One such technique is to use the natural birefringence of uniaxial crystals [42]. This technique demonstrates propagation along the specific direction θ_{PM} in a negative uniaxial crystal allows for $n_e(2\omega) = n_o(\omega)$, consequently $\Delta k = 0$ (see Fig. 1.10(a)). Another method widely employed is quasi-phase-matching (QPM). The chromatic dispersion means that after one coherence length L_{coh} a phase shift of π develops between the nonlinear polarization source and the generated second-harmonic field. Resultant destructive interference between the polarization and second-harmonic over propagation lengths larger than L_{coh} is detrimental to the SHG buildup until a 2π difference of phase. In QPM, a π phase shift is engineered between nonlinear polarization and second-harmonic fields at each multiple of the coherence length by inverting the sign of $\chi^{(2)}$. This scenario then enables the SHG efficiencies close to those obtained in phase-matched crystals. Fig. 1.10(b)

presents the schematic illustration of the SHG intensity in the quasi-phase-matched crystal. The oscillation of the polarization vector contributes to the interference-free SHG propagation in the nonlinear crystal. The period length is double the coherence length $\Phi = L_{coh} + L_{coh}$ (see Fig. 1.10(b)). In QPM, the modulation of the nonlinearity is usually realized by the periodic domain inversion in the bulk crystals or waveguides composed of ferroelectric materials [49, 50]. The process of periodic domain inversion is known as *poling*, which can be of electric [49] or all-optical [50] type. The additional periodic phase (APP) is another technique, which exploits order/disorder alignment of the nonlinear coefficient to meet the phase-matching condition in arbitrary nonlinear crystals [51].

1.2.2 Hybrid plasmonic systems for nonlinear optics

Plasmonics guarantees optical devices with miniaturized footprints, ultrafast operating speeds, and efficient power consumption compared to conventional electronics systems. These devices connect the microscale dielectric photonic systems and nanoscale electronics. Recent advancements in nanotechnology and optics have led to various plasmonic designs for a number of nanophotonic applications [12–25, 29–37, 52]. Among these designs, plasmonic nanoantenna enable an enhanced and controllable light-matter interactions as well as efficient coupling between the far-field radiation and the localized sources at the nanoscale [15–25, 52]. Likewise, plasmonic waveguides empower an efficient transfer of the optical energy, let's say between two points of an optical circuits [12–14, 29–37]. We have already established a brief introduction of several plasmonic designs and their extraordinary applications within the linear operational schemes [12–25, 29–37, 52] in the section 1.1.2 and 1.1.3.

Over the past decades, a plethora of nanophotonic research has focused on developing plasmonic designs for nonlinear optical processes with enhanced efficiencies. With plasmonic field enhancements at the core of the designated nonlinear phenomena, such designs enabled efficient integrated frequency converters, nanoscale single-photon sources, and other nonlinear devices [53–55]. Nevertheless, high losses associated with plasmonic materials (i.e., metals) still mitigate the benefits of the field enhancements. Moreover, second-order optical parametric processes such as SHG are inherently forbidden in centrosymmetric materials like metals by the electric dipole emission selection rules [53–55]. A perspective to enhance the nonlinear

interactions is the hybrid plasmonic configurations. Such systems utilize the highly enhanced localized fields of plasmonic resonances to boost the nonlinearities arising from the nonlinear material placed at the plasmonic "plasmonic-hotspots". The nonlinear matter coupled to plasmonic systems with the plasmonic resonances tuned to boost the pumped fields in the region of nonlinearity has indeed constituted a novel concept hybrid nonlinear plasmonics, with nanoantennas and plasmonic waveguides at the core [56–59]. A variety of nanoantenna designs demonstrated the enhancement of distinct nonlinear optical phenomena [49, 60–68]. Notably, the phase-matching conditions in subwavelength sizes of nanoantenna-based optical devices. Likewise, distinct hybrid plasmonic waveguides, which are the key building block of photonic integrated circuits, show several nonlinear functionalities across several application areas [59].

1.2.3 Second-order nonlinear response of metals

Although metals are centrosymmetric materials and the (local) dipole-allowed bulk nonlinear polarization cancels in a centrosymmetric optical medium [42, 54], the second-order nonlinearities in such media arise from the higher-order effects [53–55]. According to a widely employed model in the study of the SHG in centrosymmetric media [54, 69], the nonlinear polarization consists of two components: the dipole allowed surface nonlinear polarization $\mathbf{P}_s^{(2)}(\mathbf{r})$ and the nonlocal bulk nonlinear polarization $\mathbf{P}_b^{(2)}(\mathbf{r})$.

Let us consider the metal Ω_i immersed in a homogeneous medium Ω_e, as illustrated in Fig. 1.11. The free electrons are kept inside the metal domain by the ion lattice. Nonlinear optical characteristics arise from two distinct regions of the metal: the selvedge layer denoted by σ and the bulk domain denoted by Ω_b (see Fig. 1.11(b)).

The surface nonlinear polarization $\mathbf{P}_s^{(2)}(\mathbf{r})$ arises from the quantum interactions between the electrons taking place in the domain δ, which can be written as:

$$\mathbf{P}_s^{(2)}(\mathbf{r}) = \varepsilon_0 \chi_s^{(2)} : \mathbf{E}(\omega, \mathbf{r})\mathbf{E}(\omega, \mathbf{r})\delta(\mathbf{r} - \mathbf{r_s}) \tag{1.41}$$

where in the above expression $\mathbf{r_s}$ define the selvedge region σ in the Fig. 1.11(b), $\chi_s^{(2)}$ is the second order surface susceptibility tensor, and Dirac delta-function expresses the surface like characteristic of the nonlinear polarization. Note here that the in

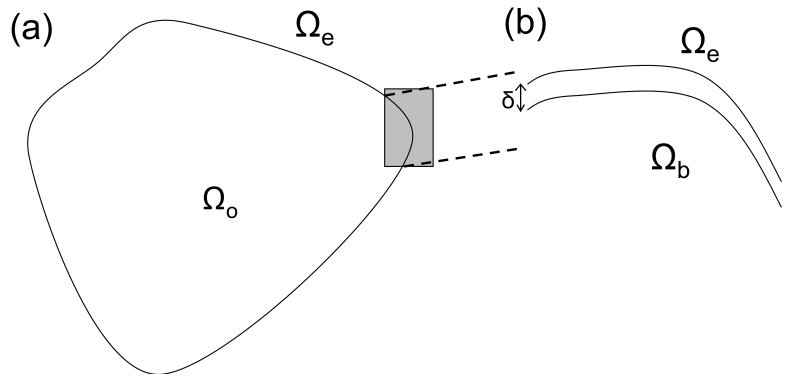

Fig. 1.11 Metal domain embedded in a medium (a) and selvedge-bulk regions near the metal domain boundary (b).

order to define the above expression the fields needed to be evaluated just inside the metal domain and not exactly at the boundary of the metal. Depending on the structural features of the metallic surface, which expect for chiral features, possesses an isotropic mirror-symmetry plane perpendicular on to the interface. The nonlinear susceptibility $\chi_s^{(2)}$ then possess only three components: $\chi_{s,\perp\perp\perp}^{(2)}$, $\chi_{s,\perp\parallel\parallel}^{(2)}$, and $\chi_{s,\parallel\perp\parallel}^{(2)} = \chi_{s,\parallel\parallel\perp}^{(2)}$, with $\perp$ and $\perp$ representing the directions normal and tangent to surface [70, 71], respectively.

Likewise, the bulk nonlinear polarization $\mathbf{P}_b^{(2)}(\mathbf{r})$ originates from the bulk domain of the metal denoted as Ω_b in the Fig. 1.11(b). This contribution is expressed as [69]:

$$\begin{aligned}\mathbf{P}_b^{(2)}(\mathbf{r}) = \gamma\nabla_i[\mathbf{E}(\omega,\mathbf{r})\mathbf{E}\cdot\mathbf{E}(\omega,\mathbf{r})] + \delta'[\mathbf{E}(\omega,\mathbf{r})\cdot\nabla]\mathbf{E}_i(\omega,\mathbf{r}) \\ + \beta[\nabla\cdot\mathbf{E}(\omega,\mathbf{r})]\mathbf{E}_i(\omega,\mathbf{r}) + \zeta\mathbf{E}_i(\omega,\mathbf{r})\nabla_i\mathbf{E}_i(\omega,\mathbf{r})\end{aligned} \tag{1.42}$$

with γ, δ', β, and ζ being the material parameters. The origin of this nonlocal nonlinear polarization is the electric quadrupoles and magnetic dipole source in the bulk of the medium [72]. There has been a debate, however, on the influence of each of these terms to nonlinear optical process. For example, in the case of noble metals, the ratio between the δ' and γ is of the order of $\mathbf{v}/\omega$ [70], with $\mathbf{v}$ being the damping frequency of free electrons, and this ratio is very small at the optical frequencies. So, practically the term proportional to δ' is neglected. Moreover, the anisotropy parameter, ζ, in the case of noble metals has a negligible value, so one the

corresponding term in Eq. (1.42) is also usually set to zero. Furthermore, the term proportional to $\nabla \cdot \mathbf{E}(\omega, \mathbf{r})$ is also usually neglected for spatially non-dispersive media. Spatial dispersion contributions, however, cannot be ignored in plasmonic structures where fields are confined to the subwavelength scales, and more advanced models, to describe nonlinear responses of the metal, are required [53, 55, 73, 74].

1.3 Advanced plasmonics

After having studied some basic notions of plasmonics and nonlinear optics, this section of the chapter presents the discussion of the theoretical model essential for understanding the numerical analysis developed later in chapter 3, the *Hydrodynamic model*. In the discussion of plasmonic systems in section 3.1, free-electron dynamics in the metal are modeled with the classical Drude model [2, 3]. The general, description of the electric displacement field in terms of material's response to the electric field in the frequency domain are as follows:

$$\mathbf{D}(\mathbf{k}, \omega) = \varepsilon_0 \varepsilon(\mathbf{k}, \omega) \mathbf{E}(\mathbf{k}, \omega)$$

while in time domain the above expression can be written as:

$$\mathbf{D}(\mathbf{r}, t) = \varepsilon_0 \int_{-\infty}^{\infty} \varepsilon(\mathbf{r} - \mathbf{r}', t - t') \mathbf{E}(\mathbf{r}', t') d\mathbf{r}' dt'$$

This form of the dielectric function can be simplified in the limits of so-called local spatial response as $\varepsilon(\mathbf{k}, \omega) = \varepsilon(\omega)$, which has been the basis for the Drude model [2, 3]. Such a simplification is valid if the wavelength of electromagnetic radiation is significantly larger than all the characteristic dimensions of the material). This assumption, however, does not hold while incorporating the description of the dynamics of the free carriers on the surface of the material. The context of the applicability of the hydrodynamic model is, therefore, the same as that of the classical models [2, 3]: the description of the optical properties of materials with a high concentration of free charge carriers.

1.3.1 Hydrodynamic model of free electrons

The hydrodynamic description of free electron comprised of set of semi-classical equations as follows:

$$m_e\left[\frac{\partial \mathbf{v}}{\partial t}+\mathbf{v}\cdot\nabla+\gamma\right]\mathbf{v}=-e(\mathbf{E}+\mathbf{v}\times\mathbf{H})-\nabla\frac{\delta G[n]}{\delta n}, \tag{1.43a}$$

$$\frac{\partial n}{\partial t}+\nabla\cdot(n\mathbf{v})=0. \tag{1.43b}$$

Eqs. (1.43) are the Euler equation and the continuity equation for electron fluid, respectively. Where, $n(\mathbf{r},t)$ and $\mathbf{v}(\mathbf{r},t)$ are the hydrodynamic variables that represent the density and velocity of the carriers, e and m_e are the charge and mass, γ is the scattering rate of electrons, $\mathbf{E}$ and $\mathbf{H}$ are local electric and magnetic fields, and and $G[n]$ contains the total internal energy of the electronic system [73, 74]. The hydrodynamic model was introduced in the 1950s with the predictions of surface plasmons. In its complete formulation, i.e., Eqs. (1.43), the model allows reproducing the susceptibility of metals along the entire frequency spectrum. The microscopic scale interactions can be integrated with the electromagnetic model, which allows the possibility of studying large-scale electromagnetic systems. This opportunity does not exist in *ab initio*-based microscopic models [75], which, although providing more quantitative results, require a great time and computational resources due to the complexity of the calculations. Thus, limiting the applicability of such microscopic approaches only to systems often smaller than those experimentally realizable. The hydrodynamic model has been applied to describe a great variety of optical phenomena at the nanometer scale involving materials with free carriers [10, 11].

The Lorentz term $(\mathbf{v}\times\mathbf{H})$ and the convective acceleration proportional to $\mathbf{v}\cdot\nabla\mathbf{v}$ in Eq. (1.43a) can be neglected within the limit of applying the hydrodynamic description of free electrons to linear optical properties of metallic systems. As for the energy functional $G[n]$, here, we consider only the quantum pressure term $(\nabla\frac{\delta p}{\delta n})$, which can be calculated in the context of the Thomas-Fermi theory of the ideal gas of fermions, obtaining the following expression [10, 11]:

$$p=\xi n(\mathbf{r},t)^{5/3}$$

where $\xi = (3\pi^3)^{(2/3)}\frac{\hbar}{5m_e}$. The term under consideration is also nonlinear, but it can be linearized and inserted into the model for a complete description of the linear properties of the systems under consideration. In particular, such hydrodynamic model constitutes a non-local correction to the plasma gas model of free electrons, allowing to adequately describe the dynamics of these carriers in nanostructures and nanoparticles [76], where due to the extremely small size of the system the influence of non-locality is no longer negligible. In these cases, the dielectric function becomes [10, 11]:

$$\varepsilon(\mathbf{k},\omega) = 1 - \frac{\omega_p^2}{\omega^2 + i\gamma\omega - \beta^2\mathbf{k}^2}$$

with $\beta = \sqrt{(5/3)\frac{n_0^{2/3}}{m_e}}$. However, since the free carrier gas is a real source of optical nonlinearities, the neglected terms will be introduced, later in this section, to describe optical nonlinearities of media with free electrons.

The Eqs. (1.43) can be easily rewritten in terms of the polarization field $\mathbf{P}(\mathbf{r},t)$ considering that $\frac{\partial \mathbf{P}}{\partial t} = \mathbf{J} = -en\mathbf{v}$, where $\mathbf{J}(\mathbf{r},t)$ is the current density. Using a perturbative approach, it is possible to write $n(\mathbf{r},t) = n_0 + n_{\text{ind}}(\mathbf{r},t)$, where n_0 and $n_{\text{ind}} = \frac{1}{e}\nabla\cdot\mathbf{P}$ are the equilibrium and the induced charge densities, respectively. Since $n_{\text{ind}} \ll n_0$ we obtain, for time-harmonic fields, the equations set:

$$\nabla^2\mathbf{E} + k_0^2\mathbf{E} = -\mu_0\omega^2\mathbf{P}, \tag{1.44a}$$

$$\beta^2\nabla\nabla\cdot\mathbf{P} + (\omega^2 + i\gamma\omega)\mathbf{P} = -\varepsilon_0\omega_p^2\mathbf{E}. \tag{1.44b}$$

to be solved for the nonlocal response of plasmonic systems within the Thomas-Fermi approximation [10, 11].

1.3.2 Nonlinear hydrodynamic theory

In order to describe nonlinear hydrodynamic description, specifically for the second-harmonic generation process, a perturbative approach [77], leads to the following equations, the first for the polarization in correspondence with the fundamental $\mathbf{P}_1$, the other for the second-harmonic $\mathbf{P}_2$ field as:

$$\beta^2\nabla\nabla\cdot\mathbf{P}_1 + (\omega_1^2 + i\gamma\omega_1)\mathbf{P}_1 = -\varepsilon_0\omega_p^2\mathbf{E}_1, \tag{1.45a}$$

$$\beta^2\nabla\nabla\cdot\mathbf{P}_2 + ((2\omega_1)^2 + 2i\gamma\omega_1)\mathbf{P}_2 = -\varepsilon_0\omega_p^2\mathbf{E}_2 + \mathbf{S}_2^{\text{NL}}. \tag{1.45b}$$

in which

$$\mathbf{S}_2^{\mathrm{NL}} = \frac{e}{m}\mathbf{E}_1\nabla\cdot\mathbf{P}_1 + i\frac{\omega_1\mu_0 e}{m}\mathbf{P}_1\times\mathbf{H}_1 - \frac{\omega_1^2}{n_0 e}\left[\mathbf{P}_1(\nabla\cdot\mathbf{P}_1)+\mathbf{P}_1\cdot\nabla\mathbf{P}_1\right] + \frac{1}{3}\frac{\beta^2}{n_0 e}\nabla(\nabla\cdot\mathbf{P}_1)^2.$$

and ω_1 if the frequency of the fundamental field. The presented equations are valid in the hypothesis that the fundamental field is not modified by the harmonic generated (undepleted pump approximation) [78]. These equations coupled with the two wave equations of the form Eq. 1.56) (one for each frequency), allow to define a complete set of equation for the computation of the material's second-harmonic generation response. In Eq. (1.45), the terms proportional $\beta^2\nabla(\nabla\cdot\mathbf{P})$ describe the linear nonlocal response for the fundamental and second-harmonic field. The $\mathbf{S}_2^{\mathrm{NL}}$ component of Eq. (1.45), on the other hand, includes the contributions that act as a nonlinear source. Among those, the terms that contain the divergence of polarization, $(\nabla\cdot\mathbf{P}_1)$, are purely surface contributions [79–82], i.e., that depend on the behavior of charge carriers in a region very close to the metal-dielectric interface.

The presence of nonlocality (spatial derivatives) in the description of the polarization field, i.e., Eq. (1.45) requires the specification of additional boundary conditions to solve the electromagnetic boundary value problem. Within the Thomas-Fermi hydrodynamic description, the continuity of the normal component of the polarization vector, i.e., $P_n^- = P_n^+$ at the metal surface must be imposed. This assumption is often combined with a constant equilibrium density n_0 in the metal, while being zero outside [79, 80, 83–85, 55]. Here we remark that although the discussion above is based on the Thomas-Fermi approximation to describe the nonlocal dynamics of the material, one can readily add higher order corrections terms to define the generalized energy functional $G[n]$ in Eq. (1.43) [73, 86], and corresponding nonlinear terms [74].

1.4 Numerical tools

The principal method used to carry out the numerical simulations presented in the draft is the *Finite Element Method* (FEM). In this section, we present the employed method, We further introduce the commercial software employed to carry out the simulations and discuss the FEM implementation of the studied problems. Notably,

here we only summarily describe the key components of the FEM modelling, and urge the reader to specialized books for details on FEM [87–89].

1.4.1 Finite element method

Partial differential equations (PDEs) express many laws of physics [90]. Analytical methods, however, provide solutions to only a handful of such problems. Instead, it is possible discretize PDEs and obtain the corresponding *numerical model equations*. Established numerical techniques can be employed to solve the numerical model equations, whose results represent the approximate solutions of the original PDEs. The finite element method (FEM) computes such approximations.

Modelling in the FEM is a two-step process:

- Reformulate PDEs in to the *variational forms*.
- The discretization of the variational forms numerical model equations, solved using the appropriate numerical methods.

Following, we brief about each of the step and discuss the merits and bottlenecks of numerical modeling in FEM.

Variational Formulation (the weak forms)

Intuitively, a PDE can be expressed as:

$$\begin{cases} Lu = f \text{ in } \Omega \\ u|_{\partial\Omega} = 0 \end{cases} \tag{1.46}$$

with L being the general differential operator, u the unknown function, f a known function of u, and PDE is defined over a computational domain Ω with boundaries $\partial\Omega$.

The recipe to obtain a variational form to a PDE is to multiply the equation by a function known as the *test function*, and integrate the resulting equation over the entire *computational domain*. For a "test function ϕ", these steps reduces the general PDE (Eq. (1.46)) to a symmetric bilinear form [87–89] such that:

$$a(u,\phi) = \int_\Omega Lu\phi d\mathbf{r} = \int_\Omega f\phi d\mathbf{r} \tag{1.47}$$

where in Eq. (1.47), the function ϕ and the unknown solution u belong to the *Hilbert space* $\mathbb{H}$. Hilbert space is an infinite-dimensional function space constituting a collection of functions with certain nice properties. These functions allow for mathematical operations the same way as ordinary vectors in a vector space. The forms of Eq. (1.47) is known as the finite element variational formulation.

Discretization of the variational forms

The discretization of finite element variational forms suggests defining a finite-dimensional subspace $\hat{V}_h \subset \mathbb{H}$ and find the approximate solution $u_h \in \hat{V}_h$. The u_h is then expressed as a linear combination of a set of basis functions $\phi_i \in \hat{V}_h$:

$$u_h(\mathbf{r}) = \sum_i u_i \phi_i(\mathbf{r}) \tag{1.48}$$

Substituting Eq. (1.48) into Eq. (1.47), we can rewrite the following linear system to find the unknown coefficients u_i as:

$$\sum_i u_i a(\phi_i, \phi_j) - \int_\Omega f \phi_j d\mathbf{r} = 0 \qquad for \;\; j = 1, ...n \tag{1.49}$$

with $a(\phi_i, \phi_j) = \int_\Omega L\phi_i \phi_j d\mathbf{r}$ and the unknowns u_i are the coefficients in the approximation of the function u. The Eq. (1.49) constructs a system of equations having the same dimension as $\hat{V}_h$. If there are n test functions used such that j goes from 1 to n, a system of n number of equations is obtained according to Eq. (1.49). Here, it is important to point out that the specifying a trial solution u_h is the fundamental step on which the quality of the finite element approximation depend, and completely wrong guess may yield a poor FEM approximation.

In Eq. (1.48-1.49), ϕ_is are known as the shape functions, which interpolate the solution values at the nodes of finite element *mesh*. Appropriate choice of shape functions is necessary to better approximate the obtained solutions. In the implementation of FEM these are usually polynomials. Fig. 1.12(a) shows a typical finite element mesh on a two-dimensional computational domain, formed by the union of triangular elements. For this discretization, a suitable choice of shape function associated with i_{th} node of the mesh element (triangle) can be the linear piecewise function having the value 1 on the node i and the value 0 on all the other nodes. In Fig. 1.12(b), we present an illustration of approximating an unknown function u considering these hat-like shape functions. Although for a 1D problem, Fig. 1.12(b) illustrates the

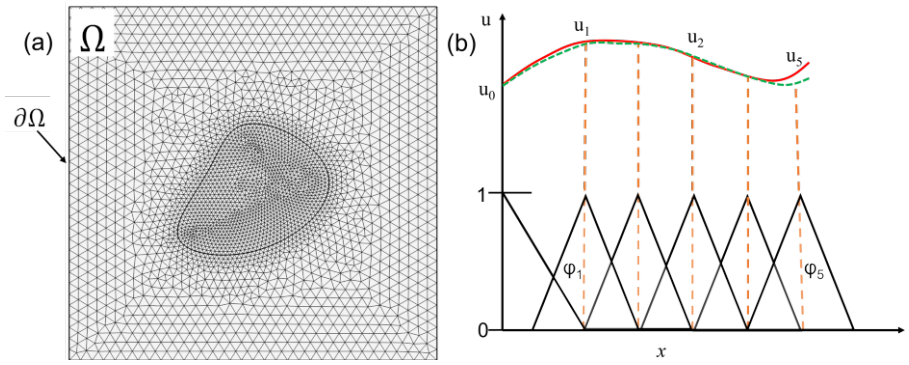

Fig. 1.12 Components of the finite element method (a) two-dimensional finite element meshing and (b) illustration of unknown function u (solid red line) approximated with u_h (dashed green line), which is a linear combination of linear basis functions (ϕ_i is represented by the solid black lines). The coefficients are denoted by u_0 through u_5.

principle. The unknown u could represent, for instance, the non-uniform temperature distribution along the rod extending in $x-$direction.

In this context, FEM provides a robust numerical approach for solving arbitrary PDEs and integral equation-based boundary value problems. It is specifically suitable for the treatment of multi-scale problems. For example, in the nanoplasmonic systems [10, 91], it is necessary to resolve for solutions in the regions of sub-nanometers. Whereas, simultaneously other regions may have effective wavelength of the order of a micron or more. The finite element method's adaptive meshing can efficiently bridge these physical regimes. Another powerful application of such numerical modeling is linking different problem domains by combining the equation systems that govern them. A disadvantage of numerical modeling in FEM can be the need for expensive computing power. Finite element solutions' accuracy depends on the number of finite elements that vary with the complexity of the domain and the physics, and may leading to large a number of numerical degrees of freedom. Another weak point of the finite element method modeling can be the implementation's complexity. Reliable and user-friendly FEM-based platforms are a need of the hour, and one remarkably effective software platform is *Comsol Multiphysics* in this regard. It is a FEM solver and simulation software for various physics and engineering applications. This commercial software provides built-in user interfaces to study various physics problems. Robustness of the package, however, reflects from allowing the implementation of customized PDEs, and the coupling between PDEs describing distinct physics.

1.4.2 Numerical implementation

With in the context of FEM implementation of the linear and nonlinear optical problems, we present the weak forms as follows. The Eq. (1.34) can be rewritten as:

$$\nabla \times \nabla \times \mathbf{E} + \mu_0 \frac{\partial^2}{\partial t^2} \varepsilon_0 \mathbf{E} = -\mu_0 \frac{\partial^2}{\partial t^2} (\mathbf{P}^{(1)} + \mathbf{P}^{\mathrm{NL}}) \tag{1.50}$$

From Eq. (1.47), one can define the differential operator $L = \nabla \times \nabla \times + \mu_0 \frac{\partial^2}{\partial t^2} \varepsilon_0$, the unknown function $u = \tilde{\mathbf{E}}$, the forcing function $f = -\mu_0 \frac{\partial^2}{\partial t^2} (\mathbf{P}^{(1)} + \mathbf{P}^{\mathrm{NL}})$, the test function $\phi = \mathbf{W}$, and $\Omega \Longrightarrow \mathbb{R}^3$ is the domain with smooth boundaries $\partial\Omega$. Then, the variational forms to Eq. (1.50), for the time-harmonic fields, can be written as:

$$\int_\Omega \left(\nabla \times \nabla \times \mathbf{E} - \mu_0 \varepsilon_0 \omega^2 \mathbf{E} \right) \cdot \tilde{\mathbf{E}} dV = \int_\Omega \mu_0 \omega^2 \left(\mathbf{P}^{(1)} + \mathbf{P}^{\mathrm{NL}} \right) \cdot \tilde{\mathbf{E}} dV \tag{1.51}$$

Taking into account the integration by parts:

$$\int_\Omega (\nabla \times \mathbf{U}) \cdot \mathbf{W} dV = \int_\Omega \mathbf{U} \cdot (\nabla \times \mathbf{W}) dV - \int_{\partial\Omega} (\mathbf{U} \times \hat{\mathbf{n}}) \cdot \mathbf{W} dS \tag{1.52}$$

the Eq. (1.51) reduces to:

$$\int_\Omega (\nabla \times \mathbf{E}) \cdot (\nabla \times \tilde{\mathbf{E}}) - \left[\mu_0 \varepsilon_0 \omega^2 \mathbf{E} - \mu_0 \omega^2 \mathbf{P}^{(1)} \right] \cdot \tilde{\mathbf{E}} dV = \int_\Omega \mu_0 \omega^2 \left(\mathbf{P}^{\mathrm{NL}} \right) \cdot \tilde{\mathbf{E}} dV \tag{1.53}$$

where in writing Eq. (1.53) the terms corresponding to the second integral in the right-hand side of the Eq. (1.52) are considered as zero. The Eq. (1.53) requires that the unknown function be continuously differentiable only once, unlike Eq. (1.51), which has a "stronger" constraint, i.e., the function must be continuously differentiable twice. For this reason, the equations having the forms similar to Eq. (1.53) are also called the weak forms. COMSOL's *Electromagnetic Wave Module* has a built-in implementation of left-hand of this equation. Such implementation suffice to extract the linear EM response of the system. Moreover, COMSOL allows the user to plugin the forcing (nonlinear) term through *weak contributions*. The implementation of the Eq. (1.53) is at the core of the results presented in the draft.

The weak forms for the polarization equation, i.e., Eq. (1.44b) can be derived as:

$$\int_{\Omega} \beta^2 (\nabla \cdot \mathbf{P}) \cdot \tilde{\mathbf{P}} + \left[(\omega^2 + i\gamma\omega)\mathbf{P} + \varepsilon_0 \omega_p^2 \mathbf{E} \right] \cdot \tilde{\mathbf{P}} dV = 0 \tag{1.54}$$

with $\tilde{\mathbf{P}}$ being the test function. Using the vector identity:

$$\int_{\Omega} \nabla (\nabla \cdot \mathbf{U}) \cdot \mathbf{W} dV = -\int_{\Omega} (\nabla \cdot \mathbf{U})(\nabla \cdot \mathbf{W}) dV + \int_{\partial\Omega} (\nabla \cdot \mathbf{U}) \mathbf{W} \cdot \hat{\mathbf{n}} dS$$

the weak form for the eq. (1.54) is:

$$\int_{\Omega} -\beta^2 (\nabla \cdot \mathbf{P})(\nabla \cdot \tilde{\mathbf{P}}) + \left[(\omega^2 + i\gamma\omega)\mathbf{P} + \varepsilon_0 \omega_p^2 \mathbf{E} \right] \cdot \tilde{\mathbf{P}} dV = 0 \tag{1.55}$$

The Eq. (1.55) can be implemented through a general interface provided in COMSOL (known as the *Weak Form PDE Module*) for specifying and solving PDEs in the weak form. Likewise, the weak form for the polarization equation Eq. (1.4.2), containing second-harmonic nonlinear source, can be derived as:

$$\int_{\Omega} \beta^2 (\nabla \cdot \mathbf{P})(\nabla \cdot \tilde{\mathbf{P}}) + \left[(4\omega^2 + 2i\gamma\omega)\mathbf{P} + \varepsilon_0 \omega_p^2 \mathbf{E} \right] \cdot \tilde{\mathbf{P}} dV = \int_{\Omega} \mathbf{S}_2^{\mathrm{NL}} \cdot \tilde{\mathbf{P}} dV$$

with nonlinear source term, $\mathbf{S}_2^{\mathrm{NL}}$, added as a weak contribution. The equations defining the polarization vector can be coupled to the equation for the electric field (Eq. (1.53)) to characterize nonlocal/nonlinear light-matter interaction.

Eigenvalue problem

In EM problems concerning waveguides, we look for the solutions to Maxwell's equations propagating along the guiding direction and confined in the guiding structure's vicinity. Thus, we must specialize in the form of the electric field and seek solutions of the form:

$$\mathbf{E}(x, y, z) = \tilde{\mathbf{E}}(x, y) e^{ik_z z} \tag{1.56}$$

where (x, y) are the transverse coordinates of the wavegudie and k_z is the wavenumber defined as:

$$k_z = \beta + i\frac{\alpha}{2}$$

with β and α being the propagation and attenuation constants, respectively. The Eq. (1.56) implicate that for a $z-$ directed waveguide, an EM mode with shape

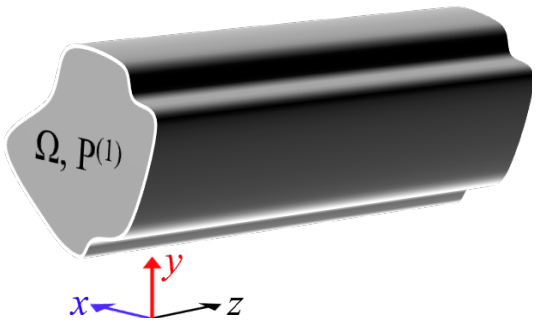

Fig. 1.13 Schematic of a generic waveguide Ω with material characteristic $P^{(1)}$. The guide is extended indefinitely along the $z-$ axis.

$\tilde{\mathbf{E}}(x,y)$ in the direction transverse to the waveguide propagate along it with a propagation constant β, and it's intensity $|\tilde{\mathbf{E}}(x,y)|^2$ attenuates with a factor of $1/\alpha$ during propagation.

For a linear and local media with polarization $\mathbf{P}^{(1)}$ the weak form to calculate the fields is:

$$\int_{\Omega} (\nabla \times \mathbf{E}) \cdot (\nabla \times \tilde{\mathbf{E}}) - \left[\mu_0 \varepsilon_0 \omega^2 \mathbf{E} - \mu_0 \omega^2 \mathbf{P}^{(1)}\right] \cdot \tilde{\mathbf{E}} dV = 0. \tag{1.57}$$

The test function $\tilde{\mathbf{E}}$ must have the form of solution similar to Eq. (1.56):

$$\tilde{\mathbf{E}} = \tilde{\mathbf{E}}(x,y) e^{-ik_z z}$$

The procedure of finding solutions' dynamics in the propagation direction and field shapes in $\tilde{\mathbf{E}}(x,y)$ in the transverse direction leads to an eigenvalue problem for the Electric field $\mathbf{E}$, with eigenvalue k_z. Such implementations are carried with the *Mode-Analysis* routine of Comsol, with finite element modelling carried out in Electromagnetic Wave Module.

Summary

In summary, here we briefed about the principles of plasmonics, nonlinear optics, and nonlinear plasmonics. We discussed the characteristics of distinct plasmonic systems (the plasmonic antennas and waveguides) through simpler systems of each configuration and reviewed their applications. From the perspective of nonlinear optics and plasmonics, we provided an exhaustive literature review to establish

the plasmonic systems' applicability nonlinear nanophotonic applications. In the following chapters, we will focus on the plasmonics-assisted enhancement of the second-harmonic generation for distinct nanostructures. This chapter also encompasses mathematical tools that are basis of the theoretical models presented in the later chapters.

Chapter 2

Hybrid Plasmonic Nanopatch Antennas for Optimal SHG

Plasmonic enhancement of nonlinear optical processes confront severe limitations arising from the strong dispersion of metal susceptibilities and small interaction volumes that hamper desirable phase-matching-like conditions. Maximizing nonlinear interactions in nanoscale systems require simultaneous excitation of resonant modes that spatially and constructively overlap at all wavelengths involved in the process.

In this chapter of the manuscript, we present a hybrid rectangular patch antenna design for optimal second harmonic generation (SHG) that is characterized by a non-centrosymmetric dielectric/ferroelectric material at the plasmonic hot spot (see Fig. 2.1 for the schematic illustration of the proposed design). The optimization of the rectangular patch allows for the independent tuning of various modes of resonances that can be used to enhance the SHG process. We explore the angular dependence of SHG in these hybrid structures and highlight conditions necessary for maximal SHG efficiency. Furthermore, we propose a novel configuration with a periodically-poled ferroelectric layer for orders-of-magnitude enhanced SHG at normal incidence. Such a platform may enable the development of integrated nanoscale light sources and on-chip frequency converters. The results discussed in this chapter comprises the contents of the publications referenced as [92, 93]. As a first author to the works [92, 93], student's contribution comprised of setting up the numerical models and

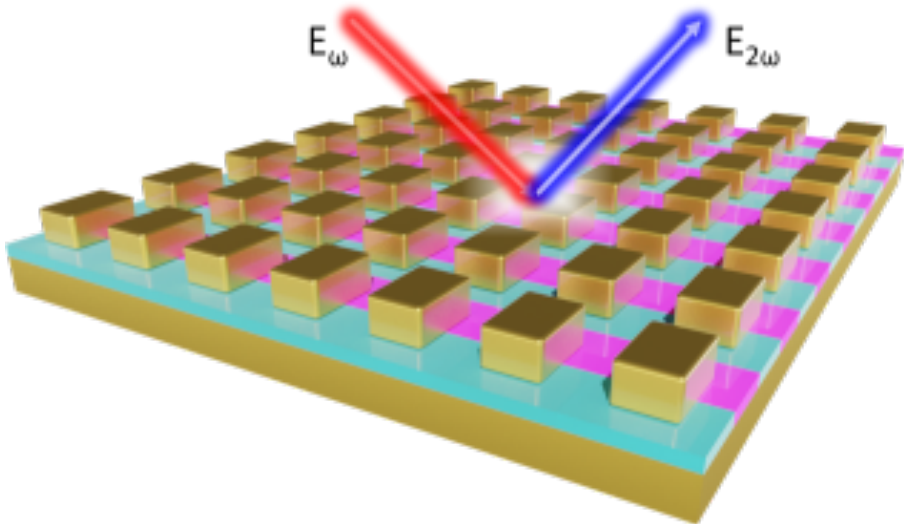

Fig. 2.1 Schematic illustration of SHG in hybrid plasmonic nanopatch antennas

obtain and organize all the presented data. Student also the contributed majorly in the preparation of the manuscripts' text.

2.1 Introduction

Optical functionalities achieved through the nonlinear interaction of light with matter are cornerstones of many present-day technological innovations [94]. These include control over the laser spectrum (optical frequency conversion), ultra-short pulse generation, and all-optical signal processing [42]. Optical nonlinear susceptibilities of natural materials are intrinsically low, and conventional nonlinear optical devices rely on high laser intensities and long propagation distances in macroscopic crystals in order to exhibit sizable nonlinear effects [42]. Such devices are often not compatible with an integrated design, and consequently hinder the realization of efficient *nanoscale* nonlinear optical components, which are essential for all-optical signal processing in photonic integrated circuits. To this end, resonant excitation (electromagnetic field enhancements) of nonlinear dielectric based nanoresonators [95–99], plasmonic metamaterials [53–59], and hybrid metal-dielectric metamaterials/metasurfaces and waveguides [49, 60–68] have been proposed to improve the efficiency of nonlinear optical processes in small volumes.

Among nonlinear optical processes, achieving efficient frequency conversion at the nanoscale is particularly desirable for many applications in biosensing [100],

photonic circuitry [101], and quantum optics [102]. The difficulty in realizing efficient frequency conversion at the nanoscale arises from the fact that some of the factors that contribute to the wave-mixing processes are often hard to satisfy simultaneously. In particular, a nanosystem needs to fulfill three main requirements [103, 104]:

- generate local field enhancement, through the excitation of resonant modes, at all the wavelengths involved in the nonlinear process [103, 105, 106];
- the different modes at the frequencies of interest need to exhibit significant spatial overlap in order to maximize their interaction in the nonlinear volume[104, 68];
- nonlinear polarization currents need to constructively add up and efficiently couple to the far-field [54].

A nanosystem that fulfills all the aforementioned properties and simultaneously offers the possibility of realizing an experimentally viable design, may pave the way towards the realization of the efficient nanoscale nonlinear devices.

For nonlinear optics, plasmonic structures can be used in two distinct configurations:

- a pure nonlinear-plasmonic configuration, in which the intrinsic nonlinear responses of the metals in the system are exploited [53–55];
- a hybrid plasmonic-dielectric configuration, where plasmonic enhancement is used to enhance the nonlinear responses of optically active dielectric materials [49, 56–68].

Although metals may posses large second- and third-order nonlinear susceptibilities, their opaqueness makes the design of pure nonlinear-plasmonic configurations challenging. Moreover, second-order nonlinear processes require a break of symmetry both at the microscopic level (i.e., at the metal surface) and at the macroscopic level (structure asymmetry) to avoid near- and far-field cancellation. This condition is difficult to achieve in some of the most efficient plasmonic systems, often characterized by locally symmetric gaps. This includes the case of two nanoparticles a few nanometers apart (in a dimer configuration) that are known to demonstrate some of the largest local field enhancements [107, 108].

Plasmonic systems formed by metallic nanoparticles over a metallic film, such as film-coupled nanosphere [49, 50] and nanopatch antennas [25] retain the characteristics of a dimer configuration in terms of local field enhancements, while simultaneously offering a better control over the thickness of gaps using modern fabrication techniques such as layer-by-layer deposition [109, 10] and atomic layer deposition (ALD) [110]. Compared to its film-coupled nanosphere counterpart, plasmonic film-coupled nanopatch systems posses a richer mode structure. Film-coupled nanopatch systems support *gap-plasmon* modes that are induced between the flat face of the nanopatch antenna and the metallic film [111, 112]. The unique properties of these modes include a wider range of tunability of resonances through careful selection of various design parameters of the system (e.g., the size of the nanopatch or the gap between the film and patch), and efficient far-field coupling due to the magnetic-dipole-like emission pattern of the patch antenna system [113–116]. Encompassing robust resonant response [111], efficient free-space coupling [114, 115], and relative ease of fabrication and incorporation of optically active dielectric gap materials, the nanopatch antenna system is an ideal candidate for developing efficient on-chip nonlinear devices.

To increase the efficiency of the nonlinear processes involving plasmonic components, often a single resonance is matched either with the fundamental wavelength to enhance the pump intensities [117, 49] or with the generated harmonic wavelength [118] to enhance the emission efficiency. This approach has been employed to demonstrate enhanced third-order nonlinear optical processes in film-coupled nanopatch antennas [65–67] and its two-dimensional counterpart, i.e., film-coupled nanowires [119, 49], with plasmonic resonances tuned at the pump wavelengths. Other nanoantenna designs have been proposed to realize doubly- or multi-resonant designs for SHG, sum- and difference-frequency generation [103, 120]. Recently, nanopatch antennas have been exploited to demonstrate enhanced SHG by coupling of the gap-plasmon mode of the nanopatch system and epsilon-near-zero mode of the spacer layer [112], and simultaneous control of third-harmonic generation, sum-frequency generation, and four-wave mixing[60]. Doubly-resonant colloidal nanoantennas have also been proposed to enhance SHG [121]. In this case, however, the lack of independent control of the patch dimensions makes it very difficult to doubly-match the system's resonances, giving rise to poor spatial mode overlap and incoherent SHG signals.

In the following, we present a numerical investigation of mode-matched SHG from plasmonic nanopatch antennas that overcome previous limitations. The proposed system operates in the hybrid framework, with a thin dielectric spacing layer of a non-centrosymmetric material acting as source of nonlinearity within a plasmonic structure. First, characteristics of the linear response of the plasmonic system and the modes taking part in mode-matched SHG are discussed. Linear resonant characteristics of two optimized mode-matched configurations of distinct modal interactions and their SHG efficiency spectra are then introduced and analyzed. We show how the symmetry of the modes taking part in the nonlinear process might lead to higher or lower SHG efficiency and associate this behaviour to the maximization/minimization of the *overlap integral*, a key parameter in nonlinear emission process. Finally, we present an ideal system that maximize SHG efficiency through optimization of this integral.

2.2 Theory and Methods

The SHG process can be described in frequency domain, under undepleted pump approximation, by the following set of equations [42]:

$$\nabla \times \nabla \times \mathbf{E}_1(\mathbf{r}) - k_1^2 \varepsilon(\mathbf{r}, \omega)\mathbf{E}_1(\mathbf{r}) = 0 \tag{2.1a}$$

$$\nabla \times \nabla \times \mathbf{E}_2(\mathbf{r}) - k_2^2 \varepsilon(\mathbf{r}, 2\omega)\mathbf{E}_2(\mathbf{r}) = 4\mu_0 \omega^2 \mathbf{P}^{(NL)}(\mathbf{r}) \tag{2.1b}$$

where $k_1 = \omega/c$, $k_2 = 2\omega/c$, with ω being the fundamental field's angular frequency; $\varepsilon(\mathbf{r}, \omega)$ is the dispersive permittivity representing the different materials of the design, μ_0 is the permeability of free space, and c is the speed of light in vacuum. In the above system of equations, Eq. (2.1a) describes the electric field at the fundamental frequency, $\mathbf{E}_1$, whereas the Eq. (2.1b) is an inhomogeneous vector wave equation that is solved for the generated (second-harmonic) signal $\mathbf{E}_2$. The right-hand side of Eq. (2.1b) represents the contributions from nonlinear sources in the system. For simplicity we have considered a nonlinear polarization vector possessing the z-component only. This is justified by the following reasons. First, the main components of the electric field of the modes excited in the film-coupled nanopatch system, as discussed in the main-text, are primarily polarized perpendicular to the metallic surface (i.e., along the z-direction). Second, the dominant component of the second-order susceptibility tensor exhibited by the nonlinear dielectric material

filling the gap between the metallic nanopatch and the film is $\chi^{(2)}_{zzz}$, whose orientation can be controlled through the film growth [49, 122]. We defined then the nonlinear polarization vector as $\mathbf{P}^{(NL)} = (0,0,\ \varepsilon_0\chi^{(2)}_{zzz}E^2_{1,z})$, with $\chi^{(2)}_{zzz} = 6$ pm/V. Note that $\mathbf{P}^{(NL)} \neq 0$ only in the thin film embedded in the gap between the metallic film and the nanopatch.

Eq. (2.1a) and Eq. (2.1b) are numerically solved using finite-element based commercial software *COMSOL Multiphysics*, within a customized frequency-dependent implementation. Solving Eqs. (2.1) is a two step process [49]: first, we solve Eq. (2.1a) under TM-polarized incidence for the fundamental field $\mathbf{E}_1$, in the subsequent step, the second harmonic signal is extracted by solving Eq. (2.1b), with the nonlinear polarization term, which is defined by utilizing the fields calculated in the first step. Equations (2.1) are solved using periodic boundary conditions, to mimic the electromagnetic response of an infinitely extended periodic array.

The nonlinear conversion efficiency, η, is defined as [49]:

$$\eta = \frac{I_{\mathrm{SHG}}}{I_{\mathrm{FF}}} \tag{2.2}$$

where I_{FF} is incident intensity at the fundamental wavelength ω and I_{SHG} is the intensity of generated signal measured in the far-field, along the specular direction with respect to the incident excitation. The intensity of the incident fields considered in the simulations is $I_{\mathrm{FF}} \simeq 55$ MW/cm^2. To circumvent the possible issue of numerical artifacts due to the field localization near the metal corners, we considered rounded corner cube with a radius of curvature of 5 nm.

We perform numerical calculations, by incorporating in our simulations the dispersive dielectric permittivity of gold [123], a complex dielectric constant $n = 1.955 + 0.0045i$, and an effective second-order nonlinear optical coefficient $\chi^{(2)}$ of 6 pm/V for the HfO_2-based ferroelectric material embedded in the gap (in the wavelength range considered here (from 0.6 to 2.4 μm) the refractive index is almost a constant) [49].

2.3 Linear Properties of the nanopatch system

As already stated, the nanopatch antenna system offers a variety of resonant modes that can be used to enhance nonlinear interactions. The wavelengths associated to

these modes can be tuned by acting on the geometrical parameters of the system. In particular, we consider a periodic array whose unit-cell design consist of a rectangular gold patch coupled to a gold substrate through a dielectric layer, as illustrated in Fig. 2.2(a). We consider a HfO_2-based ferroelectric spacer that can be grown using mature ALD processes with excellent CMOS (complementary metal-oxide-semiconductor) compatibility and potential for on-chip integration [124, 122].

Fig. 2.2(b) (top) shows a typical spectrum of the patch antenna system for normal incidence of TM-polarized plane wave. The system exhibits two resonances (indicated as FP1 and FP3, as we will show later these resonances correspond to Fabry-Pérot modes of the first- and third-order associated to the gap plasmons) that are ideal candidates to achieve mode-matching for the SHG processes. In general, however, due to the dispersion of metallic permittivities, it is very difficult for these resonances to satisfy the energy conservation condition, i.e., $\omega_{\mathrm{FP3}} = 2\omega_{\mathrm{FP1}}$. A rectangular patch, however, allows to overcome this limitation. By acting on the dimensions of the patch aligned along the x and y directions separately, it is in fact possible to tune almost independently the two resonances. For example, by increasing the arm-length a (see the dashed-curve in Fig. 2.2(b)), it is possible to largely shift the mode FP1, while only slightly modifying the mode FP3.

For oblique illumination, a distinct resonance indicated by FP2 in Fig. 2.2(b) (bottom) is excited. The tuning characteristics of this mode is similar to modes FP1 and FP3. The spatial configuration however is different among all the excited modes, as can be observed from the normalized electric field maps presented in Fig. 2.2(c−e). The electric field distributions of the modes FP1 and FP3 (for normal and oblique incidence), and FP2 (excited under oblique illumination) can be associated to Fabry-Pérot modes of the first-, third-, and second-order, respectively. In what follows, we will realize two optimized designs for SHG, with mode-matching achieved through the interaction of the mode FP1 with either the mode FP2 or FP3.

It is worth mentioning that in general, all the geometrical parameters such as thickness of the dielectric spacer, and the lattice constant of the unit-cell contribute to tuning the resonance positions. Choice of these parameters allows also for controlling the device operating spectral range.

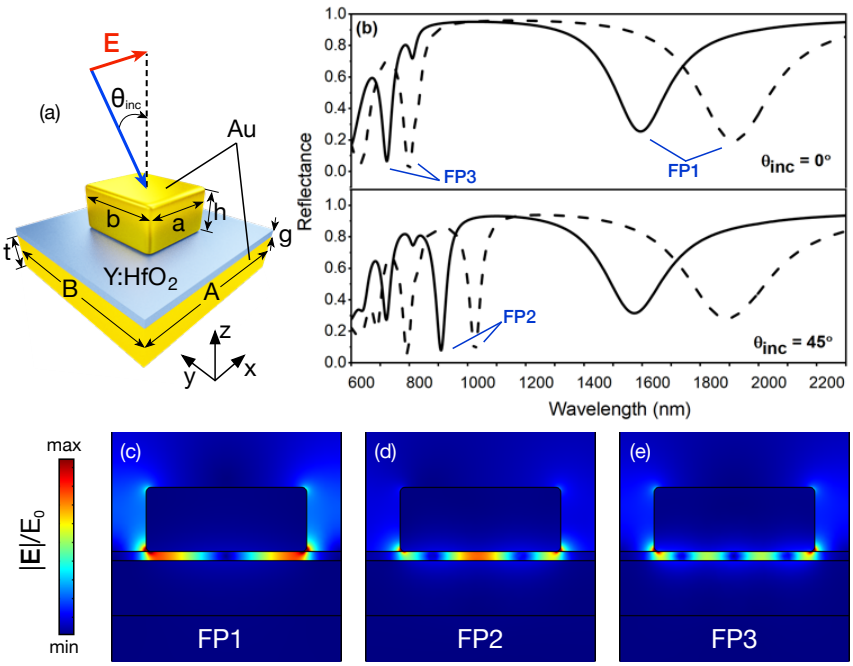

Fig. 2.2 Device layout and its linear electromagnetic response. (a) Schematic of the unit-cell of film-coupled nanopatch system and illustration of its design parameters. (b) Simulated linear reflectance spectra for different values of the patch width a (the dashed lines shows the spectra obtained by 20% increase in a); (c-e) the normalized electric field distributions (in the xz-plane) of the modes indicated as FP1, FP2, and FP3 in (b).

2.4 Mode-matched second-Harmonic generation with nanopatch system

In Fig. 2.3, we show the electromagnetic response of the mode-matched design optimized for the interaction of modes FP1 and FP3. The design is optimized for a nonlinear conversion of infrared incident to a visible light, as apparent from its linear reflection spectra presented in Fig. 2.3 (the optimized design parameters are detailed in the figure caption). The choice of these two modes is driven by three main factors:

- these modes can be excited at the normal incidence;
- the energy matching condition can be realized while keeping reasonable values of the geometrical parameters;
- there is a clear overlap between the two modes.

For these reason, one would expect this system to generate the largest SHG conversion, but as we will show in the following that there is one more very important factor that one needs to consider.

In order to numerically evaluate the efficiency of the system, we perform SHG calculations assuming the undepleted pump approximation using a one-way-coupled system of two equations (as detailed in the Methods section). The conversion efficiency η (see Eq. (3) in the Methods section) is evaluated for a TM-incident field carrying an intensity of $I_{\mathrm{FF}} \simeq 55$ MW/cm^2, impinging at different angles and wavelengths. The summary of SHG calculations for the optimized system is shown in Fig. 2.3(b). The SHG efficiency map as a function of the incident angle and wavelength is overlapped to the FP1 linear trajectory (blue curve) and linear reflection contour map around the second-harmonic (SH) wavelength. The system exhibits a modest conversion efficiency of the order of $\eta \simeq 1.2 \times 10^{-9}$ at the normal incidence, where there is a perfect overlap of the modes FP1 and FP3 at the fundamental and second-harmonic wavelengths, respectively (see Fig. 2.3(b)). For oblique illuminations, however, a gradual increase in the conversion efficiency is observed, with a maximum value reaching three orders of magnitude higher than the efficiency recorded under the normal incidence, $\eta \simeq 2.4 \times 10^{-6}$, at an incidence angle of around incidence 45°. Note that this maximum in the conversion efficiency does not seem to correspond to any particularly favorable spectral condition.

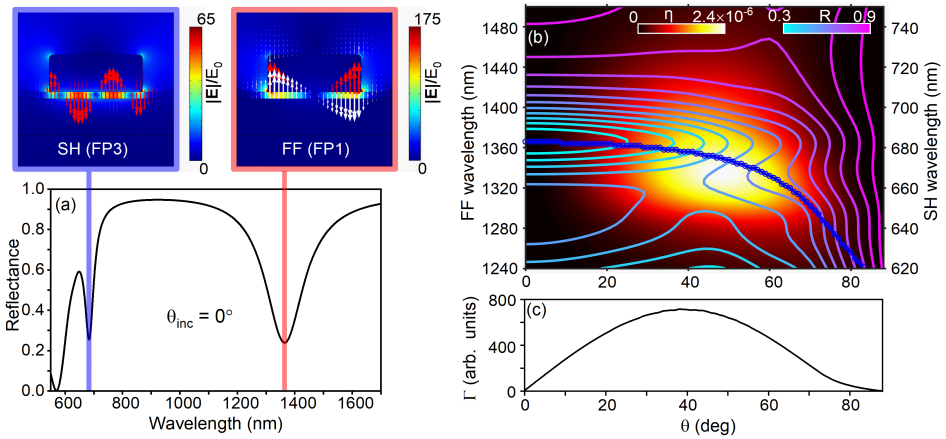

Fig. 2.3 The mode-matched design optimized for the interaction of mode FP1 and mode FP3. (a) The linear response: the reflectance spectra and normalized electric field distributions (in the xz-plane) of modes at the interacting wavelengths; the insets show the electric field distribution maps in the xz-plane; red and white arrows indicate the E_z and the E_z^2 components respectively. (b-c) The nonlinear response of the system: (b) the SHG efficiency (heat-map), linear reflection around the SHG wavelength (contour lines), and the FP1 trajectory (blue curve) as a function of the incident angles and wavelengths and (c) the overlap integral extracted following the blue trajectory in (b). The geometrical parameters are: $a = 150$ nm, $b = 80$ nm, $g = 11$ nm, $h = 60$ nm, $t = 60$ nm, $A = 250$ nm, and $B = 200$ nm (refer to schematic of the unit-cell in Fig. 2.2(a)).

In order to understand this behaviour it is useful to introduce the *overlap integral* defined as [95]:

$$\Gamma = \left| \int_{\Omega} \chi^{(2)} : \mathbf{E}(\omega)\mathbf{E}(\omega)\mathbf{E}(2\omega)^* \, d\Omega \right| \tag{2.3}$$

where $\chi^{(2)}$ is the second-order nonlinear susceptibility tensor, while the $\mathbf{E}(\omega)$ and $\mathbf{E}(2\omega)$ are the linear local fields at the fundamental and second-harmonic wavelengths, respectively. The integral is performed over the nonlinear volume Ω. The overlap integral, Γ, represents the *propensity* of the energy to flow from the fundamental to the second-harmonic mode. From its definition, it is clear that in order to maximize Γ in Eq. (2.3), local field enhancements at the wavelengths of interaction and spatial overlap are not sufficient. The product of the fields in the integrand needs to add up constructively, i.e., the modes must have the correct symmetry. It is interesting to remark that for plane waves, Γ is maximized when the phase-matching condition ($k_{2\omega} = 2k_{\omega}$), is satisfied.

In order to easily visualize how the fields interact, note that in the film-coupled nanopatch systems, resonant local electric fields in the gap are predominantly polar-

ized perpendicularly to the surface of the metal, i.e., $\mathbf{E} \simeq (0,0,E_z)$. In Fig. 2.3(a), the normalized electric field distribution map of the mode excited at the fundamental field (FF) wavelength, labeled as FF (FP1), reports its z-component, $E_z(\omega)$, with white arrows, while red arrows refer to its squared values, $E_z^2(\omega)$. Similarly, the red arrows in the field distribution map of the mode excited at second-harmonic (SH) wavelength, indicated as SH (FP3), correspond to its z-component, $E_z(2\omega)$. It is easy to see how an anti-symmetric mode at the second-harmonic wavelength interacting with the squared of an anti-symmetric mode at the fundamental wavelength (red arrows in both the field distribution maps) will minimize Γ, instead of maximizing it. This can be also observed in the overlap integral shown in Fig. 2.3(c), calculated along the trajectory of FP1. The lowest magnitude of the overlap integral is observed at the normal incidence, which leads to a smaller conversion efficiency despite the field enhancements at the wavelengths of interaction. For oblique illumination, however, a break in the symmetry results in the increase of the overlap integral, and a gradual increase (peaking in the range of 40-50°), as can be observed in the SHG efficiency spectra in Fig. 2.3(b).

In order to avoid the cancellation effects due to the anti-symmetric nature of the mode FP3, let us now consider the interaction of the mode FP1 with the mode FP2. The symmetric nature of the mode FP2 should in fact ensure the maximum efficiency conversion. The linear characteristics of the mode-matched design optimized for such an interaction are shown in Fig. 2.4(a), for a TM-polarized excitation impinging at $\theta = 40°$. This design is optimized to operate in the infrared regime. Fig. 2.4b shows the SHG efficiency map as a function of the incident angle and wavelength. The FP1 linear trajectory (blue curve) and linear reflection contour map around the second-harmonic wavelength are layered on top. In this case, the lowest values of SHG efficiency at the normal incidence are expected, since the FP2 mode cannot be excited (see the contour levels in Fig. 2.4(b)). For oblique illumination, the system exhibits a gradual increase in the SHG efficiency with a peak value of 5.5×10^{-6} at $\theta \simeq 35°$. The peak SHG efficiency for this mode-matched design is increased 2-fold in comparison with the peak efficiency of the previous design. For completeness we also show in Fig. 2.4(c) the value of the overlap integral Γ along the FP1 trajectory in Fig. 2.4(b). Similarly to the previous case, Γ follows qualitatively the SHG efficiency trend. Note however that differences between peak angles could be due to the out-coupling efficiency of the mode, which is not considered in the overlap integral calculation.

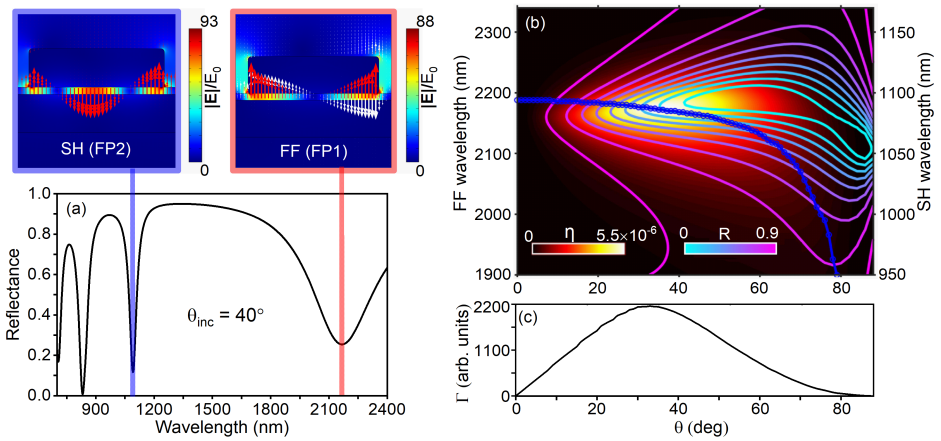

Fig. 2.4 The Mode-matched configuration optimized for the interaction of modes FP1 and FP2. (a) The linear reflectance spectra at an incident angle of $\theta = 40^\circ$ with the normalized electric field distributions at the resonant wavelengths; the insets show the electric field distribution maps in the xz-plane; red and white arrows indicate the E_z and the E_z^2 components respectively. (b-c) The nonlinear response: (b) second-harmonic efficiency spectra (heat-map, linear reflection around the SHG wavelength (contour lines), and the FP1 trajectory (blue curve) as a function of the incident angles and wavelengths and (c) the overlap integral extracted following the blue trajectory in (b). The geometrical parameters are the same as in Fig. 2.3 with $a = 211$ nm and $b = 170$ nm.

2.5 Mode-matched nano-patch configuration for optimal second-harmonic generation

Both configurations analyzed so far require to excite the patch antenna system at an oblique incidence, to achieve maximum possible SHG efficiencies. Ideally, one could remove this inconvenience by using a periodically-poled ferroelectric spacer, such that half of the patch would lay over a $-\chi^{(2)}$ material while the other half on a $+\chi^{(2)}$ material, as shown in the inset of Fig. 2.5(a).

In such a configuration, one would be able to optimize the overlap integral between the FP1 and FP3 modes at normal incidence by breaking the symmetry through the sign of $\chi^{(2)}$. This is shown in Fig. 2.5(a), where Γ is calculated over the FP1 trajectory shown in Fig. 2.3(b). This time the maximum magnitude of the overlap integral is obtained at $\theta = 0^\circ$ where quasi-phase-matching between the modes involved is obtained. In Fig. 2.5(b), we show the SHG efficiency for a poled patch antenna system at normal incidence for an interval of frequencies around the modes FP1 and FP3 for the fundamental and harmonic wavelengths, respectively. As expected, in this case, the conversion is much more efficient ($\eta \simeq 2.0 \times 10^{-6}$)

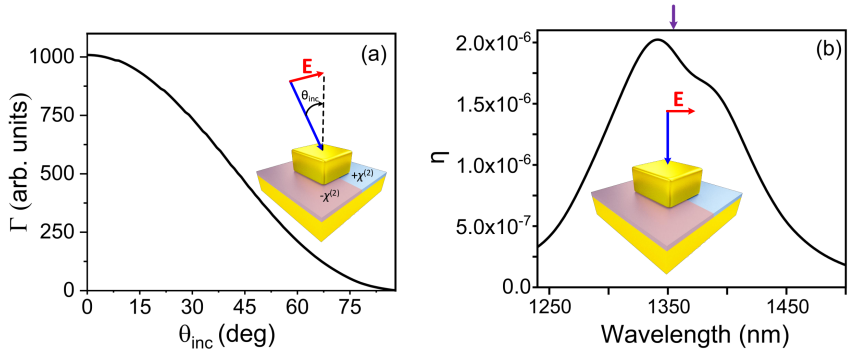

Fig. 2.5 (a) The overlap integral along the FP1 trajectory in Fig. 2.3(b) for the poled system depicted in the inset; (b) SHG efficiency spectra at normal incidence; the arrow indicates the FP1 spectral position at $\lambda_{FP1} = 2\lambda_{FP3} = 1366$ nm.

than the previous case (see Fig. 2.3(b)) at normal incidence. Interestingly, however, the overall maximum value of η remains very close to the maximum value in the previous case.

Summary

In conclusion, we have presented a strategy to doubly mode-match plasmonic resonances for efficient SHG using nanopatch antennas in the visible and near-infrared regimes. We have numerically explored different configurations by providing optimized designs for mode-matching different type of resonances. Our study has shown that a doubly resonant structure with spatial mode overlap does not guaranteed maximum efficiency. In fact, destructive interference of the generated fields may lead to weak harmonic conversion. This can be overcome by exciting the system at a non-zero angle of incidence. In general, a measure of propensity of two modes to constructively interact can be obtained by calculating the overlap integral, Γ, defined in Eq. (2.3). In all our calculations, Γ, describes very well the trend of the nonlinear SHG efficiency. Finally, we have shown that efficient SHG at normal incidence can be obtained using a periodically-poled ferroelectric spacer[124, 122], by correctly aligning poling periodicity with the patch patterning. The obtained efficiencies are comparable (for analogous input powers) to those obtained with dielectric AlGaAs nanoantennas [97], whose nonlinear susceptibility is two orders of magnitude larger than the value considered in this article. This work show the great poten-

tial and versatility of plasmonic nanopatach antennas for nonlinear nanophotonic applications.

Chapter 3

SHG in plasmonic waveguides with hydrodynamic nonlinearities

Plasmonic waveguides are an integrated platform to implement efficient nanoscale ultrafast photonic devices exhibiting higher operating bandwidths. Although metals display a rich variety of nonlocal optical effects and surface nonlinearities, the study of plasmonic waveguides has been limited to considering conventional bulk nonlinearities. Such analytical tools, however, does not allow to incorporate the *nonlocal* optical effects on the studied phenomenon or the nonlinearities arising from it. In this work, we present a method based on the numerical calculation of the inhomogeneous solution that enables the study of nonlinear optical effects, such as second-harmonic generation (SHG), in waveguides displaying nonlocal response effects as well surface nonlinearities. We use the proposed method to study the nonlinear response arising from the hydrodynamic description of free electron in the metallic constituents of the waveguides, comparing local and nonlocal approximations. As a more general application of our method we also consider nonlinearities arising from the quantum hydrodynamic theory with electron spill-out. Our results may find applicability in design and analysis of integrated photonic platforms for nonlinear optics incorporating wide variety of nonlinear materials such as heavily doped semiconductors for mid-infrared applications. The content of this chapter are a part of the results discussed in the paper referenced as [125]. Being the leading author of the work [125], student's contribution comprised of setting the numerical simulation models and obtain and organize the results data presented in

the sections 3.3.1 and 3.3.2. Moreover, student participated as a major contributor to overall preparation of the manuscript.

3.1 Introduction

Plasmonic systems provide the possibility of concentrating and manipulating light below the diffraction limit and are at the core of a variety of optical applications [4, 5], from improved chemical and biological sensing [24, 26–28], and efficient photovoltaic energy harvesting [25], to ultrafast photonic signal processing [13, 14, 29], and nanolasing [32]. In the past decades, due to the ever-increasing demand for data processing capabilities, researchers have focused a great effort into the development of ultra-compact photonic elements, including plasmonic components, such as waveguides and couplers, [13, 14], digital gates, routers, photon-electric converters, and control switches [32]. Plasmonic waveguides have also been relevant with regards to several quantum optical phenomena like single photon emission [33], energy transfer and superradiance of emitter pairs [126], and qubit-qubit entanglement generation [34]. Plasmonic systems owe the demostration of these exotic optical functionalities to surface plasmon-polariton (SPP) modes —the resonant collective oscillations of free electrons (FEs) —appearing in materials with a high carrier concentration (i.e., metals and heavily doped semiconductors) and arising at the interface with a dielectric because of the interaction with an external electromagnetic (EM) excitation. Localization of light associated to SPPs modes is naturally promising for the enhancement of intensity-dependent phenomena [53, 55, 58, 59].

Functionalities based on nonlinear optics are very attractive in terms of their femtosecond response times and terahertz bandwidths. However, sizeable nonlinear effects demand both high field intensities and large interaction volumes, together with configurations that offer efficient nonlinear conversions as well as materials with large nonlinear susceptibilities [42, 43]. All these features could be in principle provided by plasmonic systems, since metals possess some of the largest nonlinear susceptibilities. Notably, however, interaction volumes in nanoantennas are quite limited and nonlinear efficiencies remain overall very small [79, 80, 117]. On the other hand, plasmonic waveguides can sustain sub-wavelength field localization for the entire propagation length, thereby providing ideally larger volumes of interactions. Indeed, hybrid dielectric-plasmonic waveguides have been reported with a variety of

nonlinear applications (see for example a comprehensive review on latest advances in nonlinear plasmonic waveguides [59]).

In this work, we present a method to study SHG in waveguides based on the numerical calculation of the inhomogenous solution at the waveguide cross-section in the presence of arbitrary nonlinear sources. Conventionally, coupling of the pump field modes and SH modes is carried out through the evaluation of overlap integrals [127, 128]. Most waveguide systems can in fact be easily studied by decoupling the propagation and transverse problems [127, 128]. This separation is only possible when the electric field divergence, which is non-zero at the metal surface, is negligible. As it will be shown in Sec. II, such approximation does not hold when nonlinearities arise directly from the plasmonic material [129, 53, 55] and, in particular, from the dynamics of non-equilibrium FEs [129, 53, 55]. Indeed, FE nonlinearities in noble metals have been shown to strongly contribute to second-order nonlinear processes in the visible/near-infrared (IR) [79, 80, 82], while experimental measurements in gold nanoparticle arrays have demonstrated SHG efficiencies comparable to those in nonlinear crystals when normalized to the active volumes [117].

The discussion in the chapter is arranged as follows. We first present the derived method, labeled as the particular solution method (PSM) in section 3.2. We then proceed towards setting up benchmark simulations for the applicability of our method for nonlinearities described through the hydrodynamic model for free electrons in section 3.3.1. Once the benchmark is setup we will employ the proposed method to study second-harmonic generation in distinct waveguides with their nonlinear hydrodynamic nonlinearities as well as nonlinearities arising from the quantum hydrodynamic theory with electron spill-out.

3.2 Particular solution method to study SHG in a waveguide

In order to describe nonlinear interactions within a waveguide divergences of the fields are usually ignored. Further, considering the transitional invariant of the waveguide and electromagnetic problem splits to finding solutions in the transverse and longitudinal coordinates of waveguide. Moreover, the slowly varying envelope approximation —the assumption that the envelope of a forward-travelling wave pulse

varies slowly in time and space compared to a period or wavelength of —can be considered. These are the ingredients which leads to the numerical recipe of the overlap integral [127, 128], utilized extensively to study the harmonic generation in the waveguides. On the contrary, consideration that divergence of the fields is zero, does not hold for the case when spatial dispersion is considered and nonlinearities that arise from the dynamics of non-equilibrium free electrons [53, 55]. Numerical recipe of the proposed generalized formulation for the SHG in waveguide is the following.

In order to study SHG, let us expand the fields into two time-harmonic contributions as:

$$\mathbf{F}(\mathbf{r},t) = \sum_j \mathbf{F}_j(\mathbf{r}) e^{-i\omega_j t} \tag{3.1}$$

with $\mathbf{F} = \mathbf{E}$, $\mathbf{H}$, or $\mathbf{P}$ and $j = 1,2$ for the fundamental and second-harmonic wavelength. Considering the fields $\mathbf{E}_1$ and $\mathbf{E}_2$ at the interaction wavelengths in SHG process, the wave equation to describe nonlinear interactions are:

$$\nabla^2\mathbf{E}_1 - \left[1 - \beta^2 \frac{k_1^2 \chi(\omega_1)}{\omega_p^2}\right] \nabla\nabla\cdot\mathbf{E}_1 + \varepsilon_r(\omega_1) k_1^2 \mathbf{E}_1 = 0, \tag{3.2a}$$

$$\nabla^2\mathbf{E}_2 - \left[1 - \beta^2 \frac{k_2^2 \chi(\omega_2)}{\omega_p^2}\right] \nabla\nabla\cdot\mathbf{E}_2 + \varepsilon_r(\omega_2) k_2^2 \mathbf{E}_2 = -\mu_0 \omega_2^2 \mathbf{P}_2^{\mathrm{NL}}. \tag{3.2b}$$

where k_j is the free-space wavenumber and $\chi(\omega_j) = \varepsilon_r(\omega_j) - 1 = -\frac{\omega_p^2}{\omega^2 + i\gamma\omega_j}$ at ω_j, for $j = 1,2$. In writing Eq. (3.2), it is noted that, we have assumed that a material component of the the system (waveguide) is described within the Thoams-Fermi hydrodynamic formulation discussed in section 1.3.2.

Since we are interested in waveguide solutions at this point. In order to derive the fundamental field (FF) from Eq. (3.2a), let us assume, without loss of generality, that the modes propagate along the z-direction. The solution is then of the form:

$$\mathbf{E}_1(\mathbf{r}) = A_1 \tilde{\mathbf{E}}_1(x,y) e^{i\kappa_1 z} \tag{3.3}$$

with κ_1 being the complex propagation constant of the waveguide's mode at the FF, A_1 is the mode amplitude, and $\tilde{\mathbf{E}}_1(x,y)$ is the mode profile at the waveguide

cross-section. By writing $\nabla = \nabla_\perp + i\kappa_1\hat{\mathbf{z}}$, Eq. (3.2a) can be solved either analytically, in a few simple cases [83], or numerically, for an arbitrary waveguide cross-section [85, 84], using an eigenmode solver to calculate mode profile and propagation constant (see appendix A for details on the implementation in *Comsol Multiphysics* [130]). The found mode can then be normalized assuming the input-power at the $z = 0$ waveguide cross-section to be 1 W:

$$\frac{1}{2}\int_\Omega \mathrm{Re}\left[\tilde{\mathbf{E}}_1 \times \tilde{\mathbf{H}}_1^*\right] \cdot \hat{\mathbf{z}} dS = 1\mathrm{W}, \tag{3.4}$$

where Ω is the cross-sectional plane. Therefore, within these assumptions, the second-order nonlinear source in Eq. (3.2b) can be rewritten as:

$$\begin{aligned}
\mathbf{P}_2^{\mathrm{NL}}(\mathbf{r}) =& A_1^2 \frac{\chi(\omega_2)}{\omega_p^2} e^{2i\kappa_1 z} \Bigg\{ \frac{e}{m_e}\tilde{\mathbf{E}}_1(\nabla_\perp + i\kappa_1\hat{\mathbf{z}})\cdot\tilde{\mathbf{P}}_1 \\
&+ i\frac{\omega_1\mu_0 e}{m_e}\tilde{\mathbf{P}}_1 \times \tilde{\mathbf{H}}_1 \\
&- \frac{\omega_1^2}{n_0 e}\left[\tilde{\mathbf{P}}_1\left[(\nabla_\perp + i\kappa_1\hat{\mathbf{z}})\cdot\tilde{\mathbf{P}}_1\right]\right. \\
&\left. + \tilde{\mathbf{P}}_1\cdot(\nabla_\perp + i\kappa_1\hat{\mathbf{z}})\tilde{\mathbf{P}}_1\right] \\
&+ \frac{1}{3}\frac{\beta^2}{n_0 e}(\nabla_\perp + i\kappa_1\hat{\mathbf{z}})\left[(\nabla_\perp + i\kappa_1\hat{\mathbf{z}})\cdot\tilde{\mathbf{P}}_1\right]^2 \Bigg\},
\end{aligned} \tag{3.5}$$

where the mode is normalized in such a way that A_1^2 is the pump input power. For the SHG, let us now consider Eq. (3.2b). In nonlinear optics, the divergence term is generally neglected and a solution of Eq. (3.2b) can be easily obtained in the slowly varying envelope approximation, through the definition of overlap integrals evaluated in the waveguide cross-section [127, 128]. In the case of metal nonlinearities, and in particular of hydrodynamic nonlinearities, neglecting the divergence will strongly affect the results, since the larger nonlinear contributions arise at the metal surface, where the divergence is non-zero. On the other hand, fully solving Eq. (3.2b) in a three-dimensional numerical set-up is challenging, due to the large scale mismatch between the surface effects and the overall mode propagation.

The general solution of the partial differential equation (3.2b) is given by the sum of the solution of the homogeneous equation (i.e., assuming $\mathbf{P}_{2,\mathrm{NL}}(\mathbf{r}) = 0$) and a particular solution of the inhomogeneous equation, i.e., $\mathbf{E}_2(\mathbf{r}) = \mathbf{E}_h(\mathbf{r}) + \mathbf{E}_p(\mathbf{r})$.

$\mathbf{E}_h(\mathbf{r}) = \sum_m a_m \tilde{\mathbf{E}}_m(x,y)e^{i\kappa_m z}$ with $\tilde{\mathbf{E}}_m$ being the modes supported by the waveguide at ω_2, and a_m are amplitude coefficients to be determined. The modes $\tilde{\mathbf{E}}_m$ can be easily found through an eigenmode solver. As usual, we assume that the modes are normalized to carry the same input power, i.e.,

$$\frac{1}{2}\int_\Omega \tilde{\mathbf{E}}_m \times \tilde{\mathbf{H}}_m^* \cdot \hat{\mathbf{z}} dS = 1\mathrm{W}, \tag{3.6}$$

Because the system is not lossless, the modes need to satisfy the orthogonality relation described in section 1.1.3:

$$\int_\Omega \left(\tilde{\mathbf{E}}_m \times \tilde{\mathbf{H}}_n\right) \cdot \hat{\mathbf{z}} dS = N_m \delta_{nm}, \tag{3.7}$$

with

$$N_m = \int_\Omega \left(\tilde{\mathbf{E}}_m \times \tilde{\mathbf{H}}_m\right) \cdot \hat{\mathbf{z}} dS. \tag{3.8}$$

The particular solution can be sought of the form $\mathbf{E}_p(\mathbf{r}) = \tilde{\mathbf{E}}_p(x,y)e^{i2\kappa_1 z}$ where κ_1 is the known FF's propagation constant. The Eq. (3.2b) then can be solved in the waveguide cross-section by transforming the nabla operator as $\nabla = \nabla_\perp + 2i\kappa_1\hat{\mathbf{z}}$. Once $\mathbf{E}_p(\mathbf{r})$ is known we can determine the coefficients a_m by imposing the total power flow to be zero at the waveguide input, $z = 0$:

$$W_{\mathrm{SHG}}(z=0) = \frac{1}{2}\int_\Omega \mathrm{Re}\left[\mathbf{E}_2 \times \mathbf{H}_2^*\right] \cdot \hat{\mathbf{z}} dS = 0. \tag{3.9}$$

In order to do so, it is useful to project the field $\mathbf{E}_p$ on the waveguide modes at $z = 0$, i.e., find the coefficients b_m such that $\mathbf{E}_p(z=0) = \sum_m b_m \tilde{\mathbf{E}}_m$. These coefficients can be found as [41, 39] (see section 1.1.3 for the detailed derivation):

$$b_m = \frac{1}{2N_m}\int_\Omega \left(\tilde{\mathbf{E}}_p \times \tilde{\mathbf{H}}_m + \tilde{\mathbf{E}}_m \times \tilde{\mathbf{H}}_p\right) \cdot \hat{\mathbf{z}} dS. \tag{3.10}$$

The condition of Eq. (3.9) then becomes:

$$\sum_{m,n}\Bigg[\left(a_m a_n^* + a_m b_n^* + b_m a_n^* + b_m b_n^*\right) \times \int_\Omega \left(\tilde{\mathbf{E}}_m \times \tilde{\mathbf{H}}_n^*\right) \cdot \hat{\mathbf{z}} dS\Bigg] = 0, \tag{3.11}$$

If the number of modes and losses are small such that $\sum_{m\neq n}\int_\Omega \left(\tilde{\mathbf{E}}_m \times \tilde{\mathbf{H}}_n^*\right)\cdot\hat{\mathbf{z}}dS \ll \sum_m \int_\Omega \left(\tilde{\mathbf{E}}_m \times \tilde{\mathbf{H}}_m^*\right)\cdot\hat{\mathbf{z}}dS$, Eq. (3.11) can be simplified as:

$$\sum_m \Bigg[\left(|a_m|^2 + a_m b_m^* + b_m a_m^* + |b_m|^2\right) \times \int_\Omega \left(\tilde{\mathbf{E}}_m \times \tilde{\mathbf{H}}_m^*\right)\cdot\hat{\mathbf{z}}dS \Bigg] \simeq 0, \tag{3.12}$$

Since the quantity in the integral is nonzero it must be:

$$\sum_m \left(|a_m|^2 + a_m b_m^* + b_m a_m^* + |b_m|^2\right) = 0. \tag{3.13}$$

Eq. (3.13) can be satisfied by choosing $a_m = -b_m$. The SH field then can be written as:

$$\mathbf{E}_2(\mathbf{r}) = \sum_m b_m \tilde{\mathbf{E}}_m(x,y)\left(e^{i2\kappa_1 z} - e^{i\kappa_m z}\right), \tag{3.14}$$

and the SHG power as a function of the propagation distance z is given by:

$$W_{\mathrm{SHG}}(z) = \sum_m |b_m|^2 |e^{i2\kappa_1 z} - e^{i\kappa_m z}|^2. \tag{3.15}$$

Equation (3.15) constitutes the main result of this section. The SHG power along the waveguide can be obtained through the mode propagation constants, κ_1 and κ_m, at the FF and SH wavelengths, respectively. Note that if only one mode is supported by the waveguide at ω_2, i.e. $b_1 = b$, then $|b|^2 = \frac{1}{2}\int_\Omega \mathrm{Re}\left[\tilde{\mathbf{E}}_p \times \tilde{\mathbf{H}}_p^*\right]\cdot\hat{\mathbf{z}}dS$. In the following, we will refer to this method as the *particular solution method* (PSM).

3.3 SHG in plasmonic waveguides with hydrodynamic nonlinearties

In this section, we present some application examples of SHG in waveguides with hydrodynamic nonlinearities. In order to validate our method, we first consider a

simple metal-insulator-metal (MIM) waveguide. Because of the translation symmetries of the system, in fact, it is possible to easily perform full-wave calculations without having to rely on a three-dimensional implementation of the hydrodynamic equations [82]. Subsequently, we apply the PSM to a typical waveguide design without any translation symmetry in the transverse plane. Finally, we demonstrate the validity of the PSM for a system in which electron spill-out effects are taken into account through a more sophisticated model.

3.3.1 Second-harmonic generation in metal-insulator-metal waveguides (setting up a benchmark)

Different types of metal-dielectric waveguides have been presented theoretically and demonstrated experimentally (see, e.g., Ref. [2]). Here, we study a symmetric configuration, i.e., a thin dielectric layer of size g sandwiched between two gold surfaces (with the metal extending indefinitely on both sides of the dielectric), as shown in Fig. 3.1(a). We consider the following parameters for gold: $n_0 = 5.7 \times 10^{22}$ cm^{-3}, $\gamma = 1.07 \times 10^{14}$ s^{-1}, and $\beta = 1.27 \times 10^{6}$ ms^{-1} [80], while the dielectric layer has a relative permittivity $\varepsilon_d = 5.56$. The wavelengths considered for parametric interaction are $\lambda_{\mathrm{FF}} = 1550$ nm and $\lambda_{\mathrm{SH}} = 775$ nm at the FF and SH, respectively. The MIM waveguide supports symmetric gap-plasmon modes at both FF and SH wavelengths, denoted as $\mathrm{TM}_1@\lambda_{\mathrm{FF/SH}}$, and an anti-symmetric SPP at SH, indicated as $\mathrm{TM}_2@\lambda_{\mathrm{SH}}$ (see Fig. 3.1). We render the magnetic field profiles and real part of the effective indices of the modes in Fig. 3.1(b) and Fig. 3.1(c), respectively. As shown in the latter figure, their dispersive behavior holds for a wide range of gap sizes.

An efficient energy transfer from the mode at the FF to that at the SH can be obtained if a gap size is chosen that guarantees a phase-matching (PM) condition [128]. In our case, as it can be seen in Fig. 3.1(c), the PM occurs between the symmetric mode $\mathrm{TM}_1@\lambda_{\mathrm{FF}}$ at FF and the higher-order anti-symmetric modes $\mathrm{TM}_2@\lambda_{\mathrm{SH}}$ at the SH wavelength for a gap size of $g \approx 327$ nm. For the validation of our method we consider two situations: i) the just mentioned phase-matched case, and ii) a non-phase-matched, with $g = 270$ nm. We assume that the whole FF energy is in the $\mathrm{TM}_1@\lambda_{\mathrm{FF}}$ mode, while the SHG can couple to both $\mathrm{TM}_1@\lambda_{\mathrm{SH}}$ and $\mathrm{TM}_2@\lambda_{\mathrm{SH}}$. In Fig. 3.2 we show the magnetic field profile of the particular solution (PS) obtained by considering the nonlinear polarization in Eq. (3.5), as well as the modes available

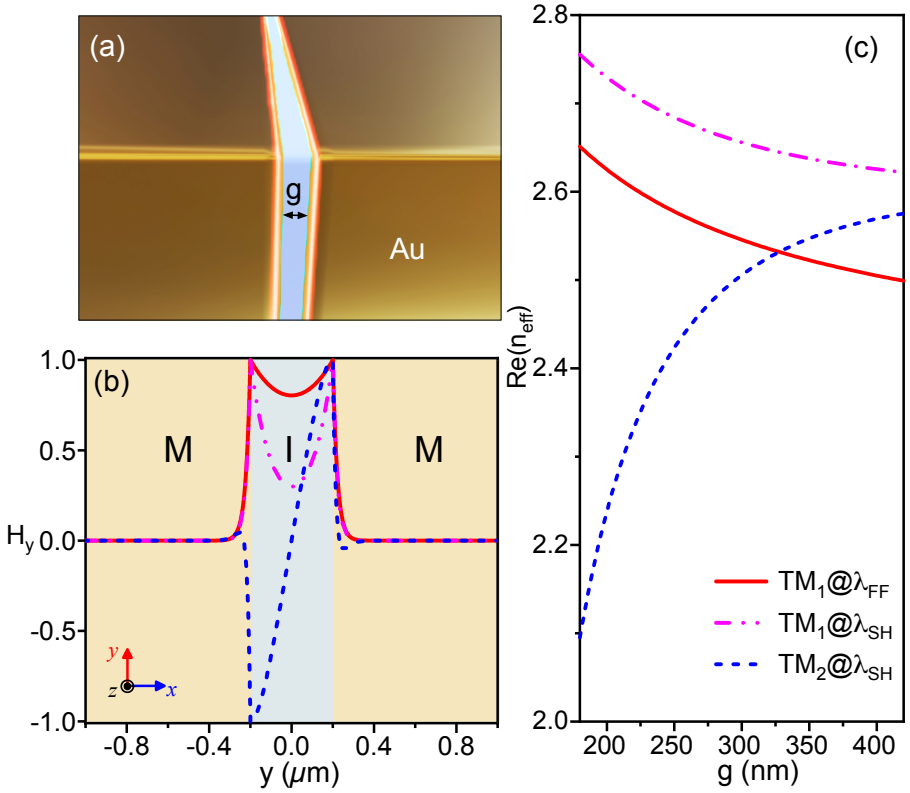

Fig. 3.1 The MIM waveguide: (a) schematic of the geometry, (b) magnetic field profiles, and (c) real part of the effective refractive indices as a function of the gap size of the supported modes.

at the SH. It is easy to guess from the plot that most of the SHG energy will be coupled to $TM_2@\lambda_{SH}$, due to the modes' symmetries. Indeed, this is confirmed by the evaluation of the coefficients $|b_m|^2$ associated to the modes, which differ by several orders in magnitude (see Table 3.1). By using Eq. (3.15) we can calculate

Table 3.1 Coefficients $|b_m|^2$ and energy flux W_p of the particular solution for the MIM waveguide.

g (nm)	$\lvert b_{TM_1}\rvert^2$	$\lvert b_{TM_2}\rvert^2$	W_p (W)
327	7.6×10^{-22}	0.25	0.25
270	2.9×10^{-24}	2.2×10^{-3}	2.2×10^{-3}

the SHG power along the waveguide, reported in Fig. 3.3 for the two studied cases, considering an input power of 1 MW/m. As expected, in the phase-matched case we observe the SH signal building up until the losses in both the FF and the SH modes

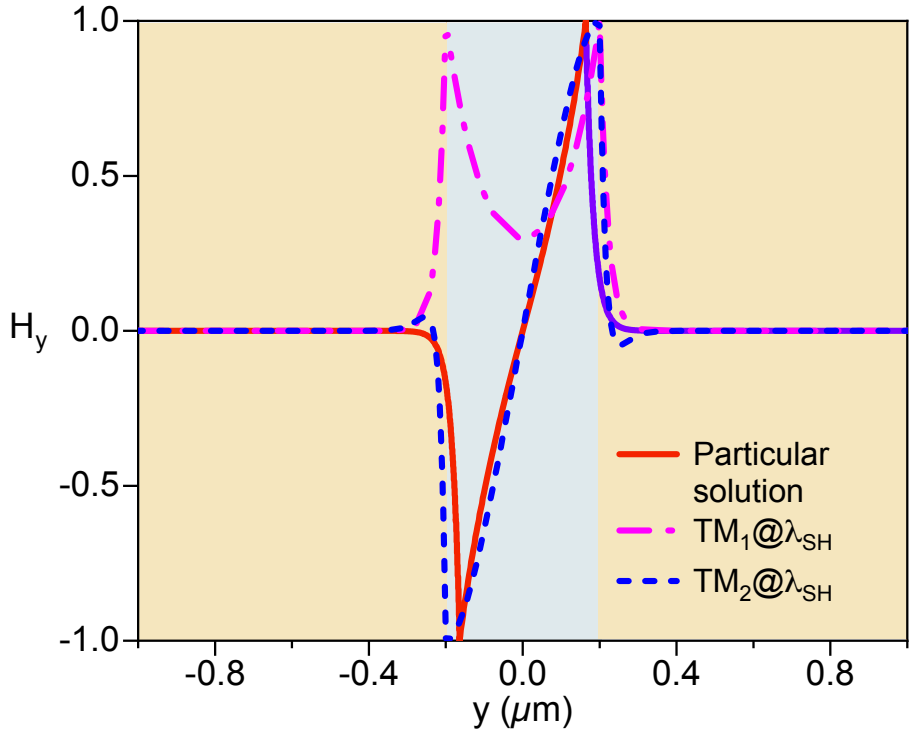

Fig. 3.2 Magnetic field transverse component, H_y, of the particular solution and modes at the SH wavelength for the MIM waveguide.

start affecting the conversion process. The SHG peak is obtained at approximately 10 μm. Conversely, in the non-phase-matched case, the SHG is limited first by the short coherence length, and then by the metal losses. However, in both cases we obtained perfect agreement with full-wave calculations [80, 79], performed by solving directly Eq. (3.2) in the x-z plane (see Fig. 3.3). These results shall lay a foundation for the applicability of the PSM to characterize the SHG in a variety of waveguides with hydrodynamic nonlinearities, as will be shown in the following subsections.

3.3.2 Non-planar waveguide with hydrodynamic nonlinearities

Non-planar waveguides, characterized by an index profile n that is a function of both transverse coordinates,are the most used in device applications There are many examples of this kind of structures, differentiated by the distinctive features of their index profiles [14, 32]. Here, we consider a non-planar waveguide whose cross-

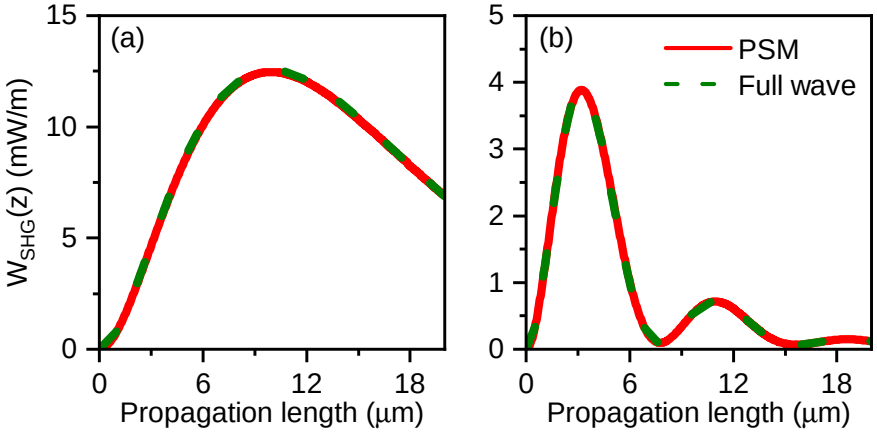

Fig. 3.3 SHG intensity as function of the of the propagation distance: (a) the phase-matched and (b) non phase-matched case for the MIM waveguide. Wavenumbers of the interacting $TM_1@\lambda_{FF}$ and $TM_2@\lambda_{SH}$ modes are: $\kappa_{FF} = 1.02\times10^7 + 3.64\times10^4 i$, $\kappa_{SH} = 2.05\times10^7 + 1.34\times10^5 i$ in (a) and $\kappa_{FF} = 1.03\times10^7 + 4.19\times10^4 i$, $\kappa_{SH} = 1.99\times10^7 + 1.49\times10^5 i$ in (b).

section is shown in the inset of Fig. 3.4(a), together with its dispersion characteristics. The structure consists of a ridge made of high-index dielectric material (Si) grown over a rectangular nanowire metallic core (which will act as a nonlinear medium) surrounded by a low-index dielectric material placed on top of a SiO_2 substrate. The index contrast of the waveguide's constituents enforces the electromagnetic energy to be confined in the core-region of the ridge, which can be exploited to enhance nonlinearities present in that region while reducing losses associated to a typical plasmonic waveguide.

The waveguide is designed to support the FF mode at $\lambda_1 = 1300$ nm, while generating at $\lambda_2 = 650$ nm. We present the modal structure of the waveguide in Fig. 3.4. The variation of the mode effective indices as a function of the height h of the metallic core is reported in Fig. 3.4, while the norm of the electric field of the supported modes is shown in Fig. 3.4. We observe that a lower-order hybrid mode of the non-planar waveguide appears at both the FF and SH wavelength (see the trends $EH_{00}@\lambda_{FF/SH}$ in Fig. 3.4). Whereas, the modal dispersion of the guided modes dictates that the higher-order hybrid modes indicated as $EH_{10/01}@\lambda_{SH}$ are excited only at the SH wavelength. The PM condition occurs between the $EH_{00}@\lambda_{FF}$ and $EH_{01}@\lambda_{SH}$ for h=89.5 nm, for fixed geometrical parameters (see the inset of Fig. 3.4).

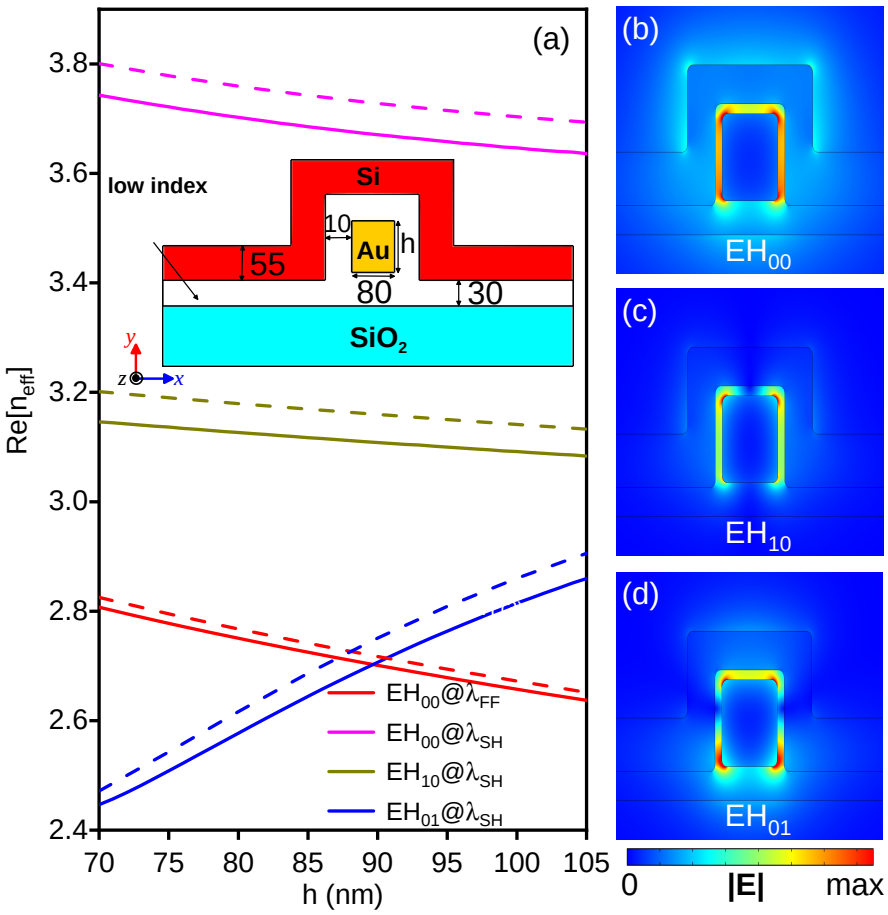

Fig. 3.4 Non-planar waveguide: (a) Tuning of the effective refractive indices as a function of the height of the metallic core, h, and (b-d) electric field profiles of modes supported by the structure at distinct wavelengths; the inset in (a) shows a schematic of the non-planar waveguide; dimensions are in nanometers. The dielectric constants used are: $\varepsilon_{\mathrm{Si}} = 12.25$, $\varepsilon_{\mathrm{SiO_2}} = 2.0$ and $\varepsilon_l = 3.422$ for the low-index dielectric. The dashed-line plots represent the dispersion characteristics of the interacting modes corresponding to the local response approximations

Let us consider a pump input power of 1 W and start quantifying the contribution of each of the mode at the SH interaction wavelength to the SHG. Based on the calculated $|b_m|^2$ of each of the mode at SH wavelength, we conclude that both the modes $\mathrm{EH}_{00}@\lambda_{\mathrm{SH}}$ and $\mathrm{EH}_{01}@\lambda_{\mathrm{SH}}$ can contribute to the SHG (see Table 3.2).

The single mode contributions and the total SHG power as a function of the propagation distance are reported in Fig. 3.5(a). Interestingly, the phase-matched mode (blue line) contributes almost negligibly to the overall SHG energy, which couple mostly into the non-phase-matched mode (green line). This counterintuitive result is

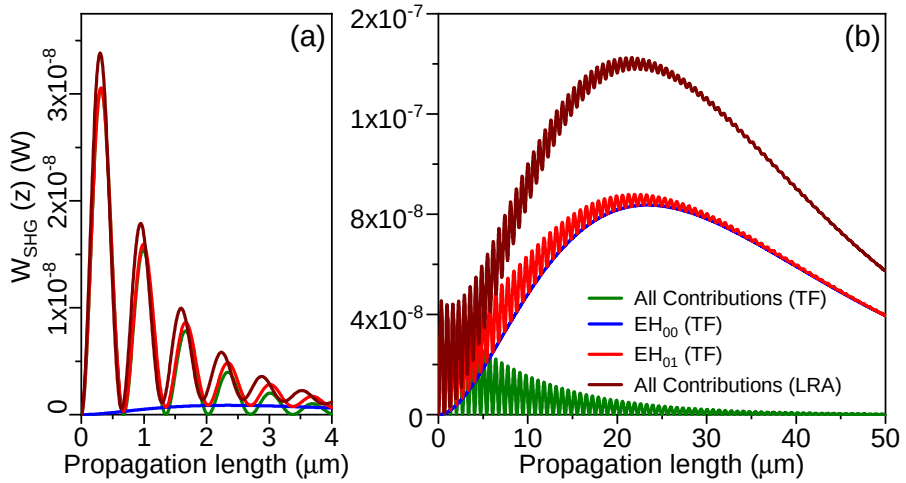

Fig. 3.5 Evolution of SHG intensity along the non-planar waveguide, (red line) total and individual SH modes' contributions (green line) EH_{00} and (blue line) EH_{01}: (a) original system and (b) the case of reduced losses. The wavenumbers of the mode involved are: $\kappa_{FF} = 1.30 \times 10^7 + 2.38 \times 10^5 i$, $\kappa_{EH_{00}} = 3.53 \times 10^7 + 5.34 \times 10^5 i$ and $\kappa_{EH_{01}} = 2.60 \times 10^7 + 3.84 \times 10^5 i$.

Table 3.2 Coefficients $|b_m|^2$ and energy flux W_p of the particular solution for the non-planar waveguide under TF approximations.

γ (s^{-1})	$\lvert b_{EH_{00}}\rvert^2$	$\lvert b_{EH_{10}}\rvert^2$	$\lvert b_{EH_{01}}\rvert^2$	W_p (W)
1.07×10^{14}	1.1×10^{-8}	1.5×10^{-20}	1.4×10^{-8}	1.5×10^{-7}
1.07×10^{13}	1.1×10^{-8}	1.5×10^{-20}	1.4×10^{-5}	1.4×10^{-5}

due to the interplay between the waveguide losses and the SHG build-up speed. To understand this mechanism, let us artificially reduce the metal losses in the waveguide by one order in magnitude. SHG along the waveguide length for such case is shown in Fig. 3.5(b). We observe that, although at small propagation distances, the non phase-matched $EH_{00}@\lambda_{SH}$ carries more SHG energy than the phase-matched mode, it diminishes quickly, whereas the contribution from the phase-matched mode slowly builds up, peaking at a distance of around 25 μm. We partially retrieve then the results for the ideal case without losses in which the SHG in the phase-matched mode increases until saturation of the pump. This example shows that, in general, the optimal device length is not determined by the coherence length of the phase-matched mode but it requires evaluating the contributions of all relevant modes. This is particularly relevant with hydrodynamic nonlinearities since most

of the surface contributions drive strong evanescent fields that can easily couple to non-phase-matched modes.

Although, we have so far considered nonlocal effects (under the TF approximation), the PSM can also be applied to the case in which the nonlinear response is due to purely surface currents. Under the well-known local response approximations (LRA) [2] it possible to define purely surface nonlinear susceptibilities [80, 81] (see section 3.5) on top of the bulk contributions, such as the Lorentz term and part of the convective term [80, 81]. Note that even within the LRA, the presence of effective magnetic currents generate sharp variations of the electric field at the metal surface, requiring a very fine mesh to avoid numerical artifacts. This makes it computationally demanding to numerically calculate SHG in a conventional three-dimensional full-wave set up. In Fig. 3.4(a), we provide the dispersion relation of the system under LRA (dashed lines). Interestingly, we observe almost no difference between the SHG intensities obtained in the presence of a hydrodynamic pressure and in the LRA (see Fig. 3.5). As we will show in next section, this is due to the fact that nonlocal optical effects are more pronounced at structure sizes below 20 nm [73, 85, 84]. In the current waveguide, the wire has a much larger size, and its SHG is virtually unaltered by the presence of nonlocal effects.

3.3.3 Plasmonic waveguide with the electron spill-out

In this section, we demonstrate the generality of the PSM by incorporating electron spill-out at the metal surfaces. While defining the nonlocal response of a material with free electrons in section 1.3, while writing Eq. (1.44b), we assumed a specific approximation for the energy functional $G[n] = T_{\mathrm{TF}}[n]$, *i.e.*, the Thomas-Fermi approximation with the hard-wall boundary conditions (i.e., no electron spill-out). In the following, we express the functional in a more general form: $G[n] = T_{\mathrm{TF}}[n] + T_{\mathrm{vW}}[n, \nabla n] + E_{\mathrm{XC}}[n]$, where T_{vW} is the von Weizsäcker correction to the TF kinetic energy and E_{XC} is the exchange-correlation energy functional. The ∇n-dependent correction in the kinetic energy functional allows to take into account the electron spill-out (spatial variation of charge density) at the metal interface. This approach is generally known as quantum hydrodynamic theory (QHT).

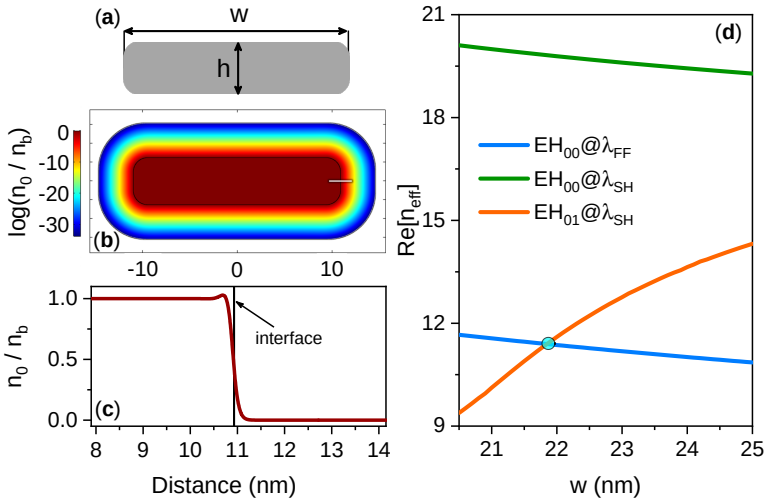

Fig. 3.6 (a) Schematic of the strip waveguide embedded in a dielectric medium with $\varepsilon_d = 5.56$. The sharp corners are rounded off with a radius of curvature of 1.5 nm. (b) The equilibrium charge density $n_0(\mathbf{r})$ normalized by the charge density in the bulk, n_b and (c) the density profile near the metal-dielectric interface along the white line shown in (b). (d) Real part of n_{eff} as a function of the guide width w, considering $h = 5$ nm.

Eq. (3.2b) can be then be generalized to:

$$-\nabla\times\nabla\times\mathbf{E}_j - \frac{\chi(\omega_j)k_j^2}{e}\nabla\left(\frac{\delta G[n]}{\delta n}\right)_j + \varepsilon_r(\omega_j)k_0^2\mathbf{E}_j = -\mu_0\omega_j^2\mathbf{P}_{j,\text{NL}} \tag{3.16}$$

where $j = 1,2$ and $\mathbf{P}_{1,\text{NL}} = 0$ (undepleted pump approximation). The nonlinear polarization $\mathbf{P}_{2,\text{NL}}$ must be enriched with nonlinear terms associated to the space dependent density as well as to the more complex expression of $G[n]$. Detailed expressions for the linear functionals and $\mathbf{P}_{2,\text{NL}}$ can be found in Ref. [74].

In order to show an example of the proposed formulation with electron spill-out within the framework of QHT, we study SHG in a metal strip waveguide of width w and height h immersed in a dielectric medium with a dielectric constant ε_d, as depicted in Fig. 3.6(a). We compute the space-dependent equilibrium electron density $n_0(\mathbf{r})$ self-consistently using the zero-*th* order QHT equation (see Ref. [73] for more details). The color map and line plot of n_0, showing the electron spill-out from the metal-dielectric interface, are presented in Fig. 3.6(b) and 3.6(c), respectively. Considering a fixed waveguide height $h = 5$ nm, this configuration supports the hybrid mode $\text{EH}_{00}@\lambda_{\text{FF}}$ at a pump wavelength $\lambda_{\text{FF}} = 1550$ nm and two

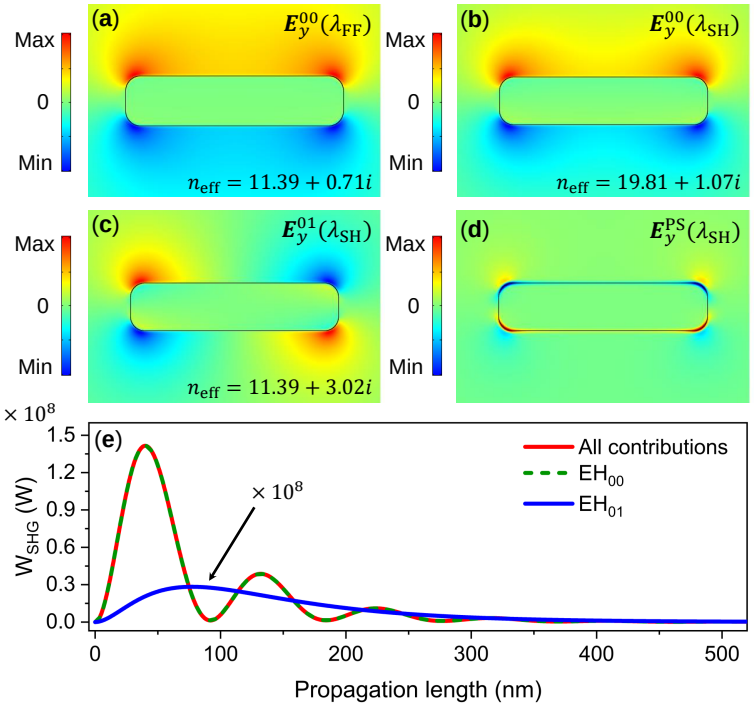

Fig. 3.7 Electric field profile (E_y–component) of the (a) fundamental mode $EH_{00}@\lambda_{FF}$, (b) first mode $EH_{00}@\lambda_{SH}$, (c) the second mode $EH_{01}@\lambda_{SH}$ at the SH wavelength, and (d) the particular solution (PS). (e) SHG intensity as a function of propagation distance along with the individual contribution of the each mode. The propagation constant of the $EH_{00}@\lambda_{FF}$ is $\kappa_{FF} = 4.62 \times 10^7 + 2.88 \times 10^7 i$ whereas those of $EH_{00}@\lambda_{SH}$ and $EH_{01}@\lambda_{SH}$ are $\kappa_{EH00} = 1.6 \times 10^8 + 8.7 \times 10^6 i$ and $\kappa_{EH01} = 9.23 \times 10^7 + 2.44 \times 10^7 i$, respectively.

hybrid modes $EH_{00}@\lambda_{SH}$ and $EH_{01}@\lambda_{SH}$ at the SH wavelength $\lambda_{SH} = 775$ nm. The real part of the effective indices of these modes as a function of waveguide width w are plotted in 3.6 (d).

The PM between the symmetric mode $EH_{00}@\lambda_{FF}$ and the anti-symmetric mode $EH_{01}@\lambda_{SH}$ occurs for the waveguide width $w = 21.85$ nm. The associated mode profiles (E_y –component) at the FF and SH are depicted in 3.7(a-c) and the field profile of the particular solution (PS) is shown in Fig. 3.7(d). To explore the contributions from each mode at the SH to the generated signal, it can be noted that nonlinear source field, i.e. the particular solution, see Fig. 3.7(d), overlaps well with the symmetric mode $EH_{00}@\lambda_{SH}$ and, therefore, major contribution to the generated power comes from this mode, as shown in Fig. 3.7(e). indeed, we can observe that there is no overlap between the nonlinear source (PS) and the $EH_{01}@\lambda_{SH}$ mode due to its anti-symmetric nature, resulting in virtually zero contribution to the SHG from

this mode. From this example, we can appreciate how important is to have access to the exact SHG along the waveguide. In fact, a traditional optimization technique, i.e. the PM technique, might not always provide the most efficient design.

Finally, we show a comparison between the aforementioned approaches in order to show the impact of the nonlocality and quantum spill-out on the mode indices on the SHG power. In particular, we consider the metal strip waveguide with the same material and geometrical parameters as considered in Fig. 3.6. The effective mode indices computed within the conventional approach, which neglects the electron pressure and spill-out, i.e., the LRA, and TFHT, which only neglects spill-out effects, are compared against the QHT, as shown in Fig. 3.8(a). The dispersion curves show that the hybrid modes at the SH wavelength are considerably influenced by the nonlocal and spill-out effects. The calculated SHG intensity along the waveguide is plotted in Fig. 3.8(b) under different approximations. It can be seen that while TFHT overestimates the SHG intensity as compared to the LRA, the QHT due to electron spill-out predicts much lower intensity. From this example, we can appreciate how important is to have access to arbitrarily precise models to evaluate exact SHG along waveguides. In fact, a traditional optimization technique, i.e. the PM technique, might not always provide the most efficient design.

3.4 Summary

We have derived and employed a method to study SHG originating from FE hydrodynamic nonlinearities in plasmonic waveguides. Our technique enables calculation of SHG arising from arbitrary sources and distinguishes itself from conventional approaches, which often neglect electron pressure effects and other quantum hydrodynamic corrections to surface nonlinear contributions. Indeed, such elements play a pivotal role in nonlinear interactions, as shown in [80, 74]. Moreover, the numerical nature of the PSM allows to easily calculate the response of purely surface nonlinear sources providing a valuable and flexible tool for nonlinear guided optics, even when not considering nonlocal or spill-out effects. In particular, our formalism can be applied to explore FE nonlinearities in mid-IR plasmonic waveguides made of heavily doped semiconductors [131], which have emerged as promising high-quality and tunable plasmonic materials in this range of wavelengths, with many potential applications in IR detection, sensing, optoelectronics and light harvesting [132]. Indeed, although FE optical nonlinearities have mostly been observed in metals,

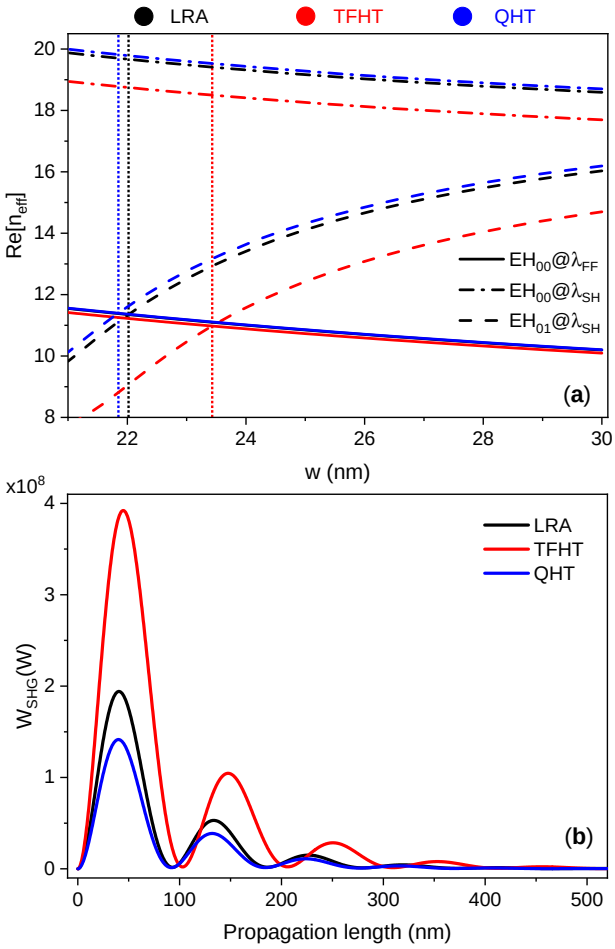

Fig. 3.8 (a) Effective mode indices as a function of guide width w computed using the conventional methods, LRA and TFHT (without electron spill-out); and are compared against the QHT (with electron spill-out). (b) SHG intensity plotted along the direction of mode prorogation under different approximations. The waveguide width considered in each case is indicated by the vertical dotted line shown in Fig. 3.8(a).

analogous effects may also occur in heavily doped semiconductors and, when coupled with plasmonic enhancement, these nonlinearities could be up to two orders of magnitude larger than conventional semiconductor nonlinearities [131].

3.5 Second-order surface susceptibilities

Centrosymmetric media like noble metals and amorphous solids does not allow bulk second-order nonlinear processes [42]. However, the center of inversion can be broken at the material's surface, giving rise to the second-order nonlinear contributions. The two nonzero surface susceptibilities, following the Ref. [80] are defined as:

$$\chi^{(2)}_{\perp\perp\perp} = -\frac{\varepsilon_0}{4n_0e}\frac{3\omega_1 + i\gamma}{2\omega_1 + i\gamma}, \tag{3.17}$$

$$\chi^{(2)}_{\parallel\perp\parallel} = -\frac{\varepsilon_0}{2n_0e}\chi_1^2. \tag{3.18}$$

where in Eqs. (3.18-3.18) n_0 is the equilibrium charge density, $-e$ is the electron charge, ε_0 is the permittivity of free space, and ε_1 is the relative permittivity of the centrosymmetric materials at fundamental frequency ω_1. The two surface nonlinear polarization components, then, can be expressed as:

$$P_\perp = \varepsilon_0\chi^{(2)}_{\perp\perp\perp}E_\perp^2, \tag{3.19}$$

$$P_\parallel = \varepsilon_0\chi^{(2)}_{\parallel\perp\parallel}E_\parallel E_\perp. \tag{3.20}$$

These polarization components can be linked to the two surface currents: the electric surface current J^e and the magnetic surface current J^m defined as [**? ?**]:

$$J^e = \frac{\partial P_\parallel}{\partial t}, \tag{3.21}$$

$$J^m = \frac{1}{\varepsilon_0\varepsilon(\omega_2)}\mathbf{n}\times\nabla_\parallel P_\perp. \tag{3.22}$$

where J^e and J^m are parallel to the surface.

3.6 Simulation configurations

Here, we present the finite element method (FEM) based implementation of the results presented in this chapter. Commercial software Comsol Multiphysics [130] has been employed for this numerical study. Outlined are two distinct schemes: (1)

implementation of the PSM presented in section 3.2 and (2) the full-wave simulation of nonlinear propagation through a waveguide.

3.6.1 Implementation of the particular solution method described in section 3.2

Our proposed theoretical model, as discussed above in section 3.2, is based on finding the guided-modes at the cross-sectional plane of the waveguide, having the forms:

$$\mathbf{F}(\mathbf{r}) = \tilde{\mathbf{F}}(x,y)e^{i\kappa z} \tag{3.23}$$

where $\mathbf{F}(\mathbf{r})$ is a general representation of all fields: electric- $\mathbf{E}$, magnetic- $\mathbf{H}$, and polarization-field $\mathbf{P}$. In Eq. (3.23), the quantity $\tilde{\mathbf{F}}(x,y)$ is the shape of the mode at the waveguide's cross-section, and κ is the complex wavenumber of the corresponding mode along the direction of the guide (z-direction) defined as:

$$\kappa = \beta + i\frac{\alpha}{2} \tag{3.24}$$

with β and α being the propagation and attenuation constant of the mode, respectively.

The Comsol Multiphysics' implementation to find $\mathbf{F}(\mathbf{r})$ is based on solving the linear coupled equation set, the Eq. (3.2) of section 3.2 with ($\mathbf{S}_{2,\mathrm{NL}} = 0$ in Eq. 3.2a). The FEM modelling of these equations is carried out in "Electromagnetic Wave" module for the field's equation, Eq. (1.56), while the polarization equation, Eq. (1.44b), is modeled through the "Weak Form PDE" module. These modules are coupled within a *Mode Analysis* study at the wavelengths of interactions in the SHG process, and we extract shape of the supported guided-modes, i.e., $\tilde{\mathbf{F}}(x,y)$, and their effective refractive indices. The calculated mode indices, denoted as n_{eff}, are then used to define the propagation constants, i.e., Eq. 3.24, of each mode as: $\kappa = kn_{\mathrm{eff}}$ where k is the free-space wavenumber.

After obtaining the guided-modes forms, i.e., $\mathbf{F}(\mathbf{r})$, one can scale the modes to a predefined input-power at the waveguide by evaluating the Eq. (3.4) and Eq. (3.6) (see section 3.2) for the FF and SH modes, respectively. Meanwhile, the found wavenumbers of the modes, "κ", help writing the specific form of the nabla operator, $\nabla = \nabla_{\perp} + i\kappa\hat{z}$ used in defining the nonlinear polarization source vector $\mathbf{S}_{2,\mathrm{NL}}(\mathbf{r})$.

This nonlinear polarization source field is then used to obtain the particular solution, $\mathbf{E}_p(\mathbf{r})$, at the SH wavelength by solving the equation set:

$$\nabla \times \nabla \times \mathbf{E}_p - k_2^2 \mathbf{E}_p = \mu_0 \omega_2^2 \mathbf{P}_p \tag{3.25a}$$

$$-\frac{en_0}{m_e} \nabla \left(\frac{\delta G[n]}{\delta n} \right)_2 - \left(\omega_2^2 + i\gamma\omega_2 \right) \mathbf{P}_p = \varepsilon_0 \omega_p^2 \mathbf{E}_p + \mathbf{S}_{2,\mathrm{NL}} \tag{3.25b}$$

In calculating particular solution, the "Electromagnetic Wave" module in Comsol is employed to model Eq. (3.25a); and the module is fed a propagation constant $2\kappa_1$, defined using the wavenumber of input (FF) mode κ_1. Likewise, the polarization equation, Eq. (3.25b), is modeled using "Weak Form PDE" module. The modules are then coupled in a *Frequency Domain* study and particular solution is obtained, which is utilized to calculate each $|b_m|^2$ (Eq. (3.10)). Finally, the calculated $|b_m|^2$ are used to implement Eq. (3.15) of the main-text to observe the evolution of the SHG along the guide's direction; simultaneously, one can also split the contribution of each distinct mode, at the SH, to the generated signal.

3.6.2 Full-wave simulation

In this section, we present a generalized method to study EM wave propagation in a *waveguide* by employing full wave simulations. Full wave simulations are electromagnetic problems that describe the propagation of predefined excitations, generally along a cross-sectional volume. The EM wave propagation in a waveguide is somewhat linked to the electromagnetic problem solved at the cross-sectional plane, i.e., finding the excitations (modes) $\mathbf{F}(\mathbf{r}) = \tilde{\mathbf{F}}(x,y)e^{i\kappa z}$. In the subsection (3.6.1), we have described this procedure.

Once the modal field shapes and the corresponding dispersion characteristics (wavenumbers) are known, the next step is to utilize these modes as an excitation to the waveguide and solve an EM wave propagation problem in the cross-sectional volume of the waveguide. We define excitation to the waveguide by using *User defined Port*s provided in Comsol's "Electromagnetic Wave" module. The *Port*'s mode settings are specified by the wavenumber and corresponding modal fields from the problem solved at the cross-sectional plane of the waveguide; with

"generalized nonlocal extrusion coupling operator" of Comsol mapping modal fields on the ports. The EM wave propagation is then characterized by solving the coupled equation set:

$$\nabla \times \nabla \times \mathbf{E}_j - k_j^2 \mathbf{E}_j = \mu_0 \omega_j^2 \mathbf{P}_j \tag{3.26a}$$

$$-\frac{en_0}{m_e} \nabla \left(\frac{\delta G[n]}{\delta n} \right)_j - \left(\omega_j^2 + i\gamma\omega_j \right) \mathbf{P}_j = \varepsilon_0 \omega_p^2 \mathbf{E}_j + \mathbf{S}_{j,\mathrm{NL}} \tag{3.26b}$$

The Eqs. (3.26) are solved by employing *Frequency Domain* study of "Electromagnetic Wave" module coupled to "Weak Form PDE" module, for $j = 1$ at the FF and $j = 2$ for the SH field, with $\mathbf{S}_{1,\mathrm{NL}} = 0$ since we operate under the undepleted pump framework. Finally, intensity of the modes, at both the FF and SH (generated) field can be evaluated along the waveguide by employing *General Projection* operator provided in Comsol.

Chapter 4

Conclusions and Outlook

In this thesis, I presented a theoretical study and the numerical implementation of the SHG in distinct plasmonic nanostructures, with particular focus on plasmonic enhancement of the underlying nonlinear phenomena.

The Chapter 1 of the manuscript provides an overview of plasmonics, the principles of nonlinear optics and application of plasmonics for nonlinear optics. In particular, I discuss the hybrid nonlinear plasmonic systems, which are the core of the results parented in one of the part of the draft. I discuss the basics of the numerical method, the FEM, utilized to for the presented studies. I provide details on the numerical implementation of the studied problems using a commercial software COMSOL Multiphysics, including their governing FEM weakforms. The key information in this chapter also comprised of the discussion on the mode-orthogonality theorem in optical waveguide and the modal expansion of a field, the core to our novel "particular solution method (PSM)" used to study SHG in optical waveguides composed of arbitrary nonlinear sources. Further, the advanced plasmonic topics and their significance has been introduced. The main point of this chapter was to provide an overview of the basic concepts and techniques used for state of the art numerical studies presented in this thesis.

In Chapter 2, I presented the numerical implementation of the SHG in hybrid-plasmonic nanopatch antennas. I studied two mode-matched configurations of the distinct modal characteristics and operating regimes. For both the studied configurations, angular dependence of the SHG is studied. In each of the configuration the optimal SHG efficiency is observed at the oblique angles. I explored the origin of

optimal second-harmonic signal. The origin of the optimal SHG in each system is linked to the overlap integral.

Note that the although *higher* SHG efficiencies in each of the mode-matched configurations, their optimal excitation conditions (oblique illuminations) are not favorable experimentally. Moreover, one of the optimized mode-matched SHG configurations, although presenting the highest efficiency, was obtained for design parameters difficult to be fabricated. In that regard, the second part of this chapter is focused on obtaining a mode-matched design, that enables optimal SHG at the normal illuminations and allow for an experimentally realizable design. We realize such a system, by loading the spacer layer in the nanopatch antenna with a periodically poled materials HfO_2 [49]. The physical origin of the to obtain such optimal efficiency in such a system is explored, which is linked with the periodic modulation of the of nonlinearities that enables quasi phase-matching like conditions [42] to meet, although the system is still has miniaturized scale footprints.

The significance and outlook of the work presented in chapter 2 are that, first the study shows the versatility of the nano-patch system as a controllable platform for nano-optical applications. Second the work discusses the strategy to extract optimal nonlinear efficiencies in nanoplasmonic systems. Future works on nonlinear nano-optics may benefit from the strategy while designing systems exhibiting optimal nonlinearities.

In Chapter 3, I presented a novel semi-analytical formulation of to study SHG in plasmonic waveguides in the presence of variety of nonlinear sources, including nonlinearities that arise from the nonlocal effects based on the hydrodynamic of motion of free electrons. I employed the proposed formulation in variety of waveguides for the SHG, including plasmonic waveguide with electron spill-out. I also compared the SHGs obtained in the presence of distinct free electron nonlinear sources, which also included the surface hydrodynamic nonlinear sources. It's the robustness of our formulation that all the such distinct type nonlinearities can be readily incorporated to study the designated phenomenon. All the studies are carried out with computational rigor which is much less than what such studies would incur under the conventional full-wave simulations. The validity of the proposed formulation through the full-wave FEM simulations is also a part of the works presented in this chapter.

Plasmonic waveguides are a key building block of optical circuits for nanoscale signal processing. Nonlinear optical functionalities are at the core of the devices demonstrating ultrafast optical functionalities and wider bandwidths. To this end the work presented in chapter 3 provide a useful numerical tool to study the nonlinear optical effects in plasmonic waveguides incorporating variety of nonlinear sources. A natural direction for the future development of the work in this chapter 3 would be the study of the nonlinear optical phenomenon arising from the materials with heavily doped semiconductors. Such studies may enables optical applications in the newly explored mid-infrared range op EM spectrum for sensing and energy harvesting applications.

References

[1] L. Novotny and B. Hecht, *Principles of nano-optics*. Cambridge university press, 2012.

[2] S. A. Maier, *Plasmonics, Fundamentals and Applications*. Springer, 2007.

[3] J. Weiner and F. Nunes, *Light-matter interaction: physics and engineering at the nanoscale*. (Oxford University Press, 2017).

[4] M. I. Stockman, K. Kneipp, S. I. Bozhevolnyi, S. Saha, A. Dutta, and et al., "Roadmap on plasmonics," *Journal of Optics*, vol. 20, p. 043001, mar 2018.

[5] S. Lal, S. Link, and N. J. Halas, "Nano-optics from sensing to waveguiding," *Nanoscience And Technology: A Collection of Reviews from Nature Journals*, pp. 213–220, 2010.

[6] E. Abbe, "Ueber einen neuen beleuchtungsapparat am mikroskop," *Archiv für mikroskopische Anatomie*, vol. 9, no. 1, pp. 469–480, 1873.

[7] R. H. Ritchie, "Plasma losses by fast electrons in thin films," *Phys. Rev.*, vol. 106, pp. 874–881, Jun 1957.

[8] C. J. Powell and J. B. Swan, "Origin of the characteristic electron energy losses in aluminum," *Phys. Rev.*, vol. 115, pp. 869–875, Aug 1959.

[9] J. D. Jackson, "Classical electrodynamics," 1999.

[10] C. Ciracì, R. T. Hill, J. J. Mock, Y. Urzhumov, A. I. Fernández-Domínguez, S. A. Maier, J. B. Pendry, A. Chilkoti, and D. R. Smith, "Probing the ultimate limits of plasmonic enhancement," *Science*, vol. 337, no. 6098, pp. 1072–1074, 2012.

[11] C. Ciraci, J. B. Pendry, and D. R. Smith, "Hydrodynamic model for plasmonics: a macroscopic approach to a microscopic problem," *ChemPhysChem*, vol. 14, no. 6, pp. 1109–1116, 2013.

[12] S. I. Bozhevolnyi, "Plasmonic nano-guides and circuits," in *Plasmonics and Metamaterials*, p. MWD3, Optical Society of America, 2008.

[13] J. Zhang, L. Zhang, and W. Xu, "Surface plasmon polaritons: physics and applications," *Journal of Physics D: Applied Physics*, vol. 45, p. 113001, feb 2012.

[14] R. Zia, J. A. Schuller, A. Chandran, and M. L. Brongersma, "Plasmonics: the next chip-scale technology," *Mater. Today*, vol. 9, no. 7, pp. 20–27, 2006.

[15] J. A. Schuller, E. S. Barnard, W. Cai, Y. C. Jun, J. S. White, and M. L. Brongersma, "Plasmonics for extreme light concentration and manipulation," *Nat. Mater.*, vol. 9, no. 3, pp. 193–204, 2010.

[16] P. Muhlschlegel, H.-J. Eisler, O. J. Martin, B. Hecht, and D. Pohl, "Resonant optical antennas," *science*, vol. 308, no. 5728, pp. 1607–1609, 2005.

[17] M. Agio and A. Alù, *Optical antennas*. Cambridge University Press, 2013.

[18] M. Song, D. Wang, S. Peana, S. Choudhury, P. Nyga, Z. A. Kudyshev, H. Yu, A. Boltasseva, V. M. Shalaev, and A. V. Kildishev, "Colors with plasmonic nanostructures: A full-spectrum review," *Applied physics reviews*, vol. 6, no. 4, p. 041308, 2019.

[19] V. Giannini, A. I. Fernández-Domínguez, S. C. Heck, and S. A. Maier, "Plasmonic nanoantennas: fundamentals and their use in controlling the radiative properties of nanoemitters," *Chemical reviews*, vol. 111, no. 6, pp. 3888–3912, 2011.

[20] P. Biagioni, J. S. Huang, L. Duò, M. Finazzi, and B. Hecht, "Cross resonant optical antenna," *Phys. Rev. Lett.*, vol. 102, p. 256801, Jun 2009.

[21] V. K. Valev, J. J. Baumberg, C. Sibilia, and T. Verbiest, "Chirality and chiroptical effects in plasmonic nanostructures: fundamentals, recent progress, and outlook," *Advanced Materials*, vol. 25, no. 18, pp. 2517–2534, 2013.

[22] M. Poblet, R. Berté, H. D. Boggiano, Y. Li, E. Cortés, G. Grinblat, S. A. Maier, and A. V. Bragas, "Acoustic coupling between plasmonic nanoantennas: Detection and directionality of surface acoustic waves," *ACS Photonics*, vol. 8, no. 10, pp. 2846–2852, 2021.

[23] J. Mejía-Salazar and O. N. Oliveira Jr, "Plasmonic biosensing: Focus review," *Chemical reviews*, vol. 118, no. 20, pp. 10617–10625, 2018.

[24] J. M. Fitzgerald, S. Azadi, and V. Giannini, "Quantum plasmonic nanoantennas," *Physical Review B*, vol. 95, no. 23, p. 235414, 2017.

[25] A. Moreau, C. Ciracì, J. J. Mock, R. T. Hill, Q. Wang, B. J. Wiley, A. Chilkoti, and D. R. Smith, "Controlled-reflectance surfaces with film-coupled colloidal nanoantennas," *Nature*, vol. 492, pp. 86–89, 2012.

[26] G. M. Akselrod, C. Argyropoulos, T. B. Hoang, C. Ciracì, C. Fang, J. Huang, D. R. Smith, and M. H. Mikkelsen, "Probing the mechanisms of large purcell enhancement in plasmonic nanoantennas," *Nature Photonics*, vol. 8, no. 11, pp. 835–840, 2014.

[27] M. Manjare, F. Wang, S. G. Rodrigo, and H. Harutyunyan, "Exposing optical near fields of plasmonic patch nanoantennas," *Applied Physics Letters*, vol. 111, no. 22, p. 221106, 2017.

[28] M. Zhang, M. Pu, F. Zhang, Y. Guo, Q. He, X. Ma, Y. Huang, X. Li, H. Yu, and X. Luo, "Plasmonic metasurfaces for switchable photonic spin–orbit interactions based on phase change materials," *Advanced Science*, vol. 5, no. 10, p. 1800835, 2018.

[29] W. L. Barnes, A. Dereux, and T. W. Ebbesen, "Surface plasmon subwavelength optics," *Nature*, vol. 424, no. 6950, pp. 824–830, 2003.

[30] S. Szunerits and R. Boukherroub, *Introduction to plasmonics: advances and applications*. CRC Press, 2015.

[31] S. K. Selvaraja and P. Sethi, "Review on optical waveguides," *Emerging Waveguide Technology*, vol. 95, 2018.

[32] Y. Fang and M. Sun, "Nanoplasmonic waveguides: towards applications in integrated nanophotonic circuits," *Light Sci. Appl.*, vol. 4, no. 6, pp. e294–e294, 2015.

[33] A. Huck and U. L. Andersen, "Coupling single emitters to quantum plasmonic circuits," *Nanophotonics*, vol. 5, no. 3, pp. 483–495, 2016.

[34] A. Gonzalez-Tudela, D. Martin-Cano, E. Moreno, L. Martin-Moreno, C. Tejedor, and F. J. Garcia-Vidal, "Entanglement of two qubits mediated by one-dimensional plasmonic waveguides," *Phys. Rev. Lett.*, vol. 106, p. 020501, Jan 2011.

[35] H. N. Daghestani and B. W. Day, "Theory and applications of surface plasmon resonance, resonant mirror, resonant waveguide grating, and dual polarization interferometry biosensors," *Sensors*, vol. 10, no. 11, pp. 9630–9646, 2010.

[36] M. R. Rakhshani, "Tunable and sensitive refractive index sensors by plasmonic absorbers with circular arrays of nanorods and nanotubes for detecting cancerous cells," *Plasmonics*, vol. 15, no. 6, pp. 2071–2080, 2020.

[37] Y. Wang, W. Srituravanich, C. Sun, and X. Zhang, "Plasmonic nearfield scanning probe with high transmission," *Nano letters*, vol. 8, no. 9, pp. 3041–3045, 2008.

[38] A. W. Snyder and J. Love, *Optical waveguide theory*. Springer Science & Business Media, 2012.

[39] S. F. Mahmoud, *Electromagnetic waveguides: theory and applications*. No. 32, IET, 1991.

[40] P. Bienstman, *Rigorous and efficient modelling of wavelenght scale photonic components*. PhD thesis, Ghent University, 2001.

[41] P. R. McIsaac, "Mode orthogonality in reciprocal and nonreciprocal waveguides," *IEEE transactions on microwave theory and techniques*, vol. 39, no. 11, pp. 1808–1816, 1991.

[42] R. W. Boyd, *Nonlinear Optics*. Academic Press, San Diego, CA, 2006.

[43] E. Garmire, "Nonlinear optics in daily life," *Opt. Express*, vol. 21, pp. 30532–30544, Dec 2013.

[44] M. L. Brongersma and V. M. Shalaev, "The case for plasmonics," *science*, vol. 328, no. 5977, pp. 440–441, 2010.

[45] T. H. Maiman *et al.*, "Stimulated optical radiation in ruby," 1960.

[46] P. A. Franken, A. E. Hill, C. W. Peters, and G. Weinreich, "Generation of optical harmonics," *Phys. Rev. Lett.*, vol. 7, pp. 118–119, Aug 1961.

[47] N. Bloembergen and P. Pershan, "Light waves at the boundary of nonlinear media," *Physical review*, vol. 128, no. 2, p. 606, 1962.

[48] M. L. Alles, R. Pasternak, X. Lu, N. H. Tolk, R. D. Schrimpf, D. M. Fleetwood, R. P. Dolan, and R. W. Standley, "Second harmonic generation for noninvasive metrology of silicon-on-insulator wafers," *IEEE transactions on semiconductor manufacturing*, vol. 20, no. 2, pp. 107–113, 2007.

[49] J. Qin, F. Huang, X. Li, L. Deng, T. Kang, A. Markov, F. Yue, Y. Chen, X. Wen, S. Liu, *et al.*, "Enhanced second harmonic generation from ferroelectric hfo_2-based hybrid metasurfaces," *ACS Nano*, vol. 13, no. 2, pp. 1213–1222, 2019.

[50] X. Chen, P. Karpinski, V. Shvedov, A. Boes, A. Mitchell, W. Krolikowski, and Y. Sheng, "Quasi-phase matching via femtosecond laser-induced domain inversion in lithium niobate waveguides," *Optics Letters*, vol. 41, no. 11, pp. 2410–2413, 2016.

[51] M. Shao, F. Liang, H. Yu, and H. Zhang, "Pushing periodic-disorder-induced phase matching into the deep-ultraviolet spectral region: theory and demonstration," *Light: Science & Applications*, vol. 9, no. 1, pp. 1–8, 2020.

[52] D. Rossouw and G. A. Botton, "Plasmonic response of bent silver nanowires for nanophotonic subwavelength waveguiding," *Phys. Rev. Lett.*, vol. 110, p. 066801, Feb 2013.

[53] M. Kauranen and A. V. Zayats, "Nonlinear plasmonics," *Nature photonics*, vol. 6, no. 11, pp. 737–748, 2012.

[54] J. Butet, P.-F. Brevet, and O. J. Martin, "Optical second harmonic generation in plasmonic nanostructures: from fundamental principles to advanced applications," *ACS Nano*, vol. 9, no. 11, pp. 10545–10562, 2015.

[55] A. V. Krasavin, P. Ginzburg, and A. V. Zayats, "Free-electron optical nonlinearities in plasmonic nanostructures: a review of the hydrodynamic description," *Laser Photonics Rev.*, vol. 12, no. 1, p. 1700082, 2018.

[56] A. Krasnok, M. Tymchenko, and A. Alù, "Nonlinear metasurfaces: a paradigm shift in nonlinear optics," *Materials Today*, vol. 21, no. 1, pp. 8–21, 2018.

[57] N. C. Panoiu, W. E. I. Sha, D. Y. Lei, and G.-C. Li, "Nonlinear optics in plasmonic nanostructures," *Journal of Optics*, vol. 20, p. 083001, jun 2018.

[58] L. Bonacina, P.-F. Brevet, M. Finazzi, and M. Celebrano, "Harmonic generation at the nanoscale," *J. Appl. Phys.*, vol. 127, no. 23, p. 230901, 2020.

[59] A. Tuniz, "Nanoscale nonlinear plasmonics in photonic waveguides and circuits," *Riv. del Nuovo Cim.*, pp. 1–57, 2021.

[60] Q. Shen, W. Jin, G. Yang, A. W. Rodriguez, and M. H. Mikkelsen, "Active control of multiple, simultaneous nonlinear optical processes in plasmonic nanogap cavities," *ACS Photonics*, vol. 7, no. 4, pp. 901–907, 2020.

[61] W. Fan, S. Zhang, K. Malloy, S. Brueck, N. Panoiu, and R. Osgood, "Second harmonic generation from patterned gaas inside a subwavelength metallic hole array," *Opt. Express*, vol. 14, no. 21, pp. 9570–9575, 2006.

[62] C. J. Barrelet, H.-S. Ee, S.-H. Kwon, and H.-G. Park, "Nonlinear mixing in nanowire subwavelength waveguides.," *Nano Letters*, vol. 11, pp. 3022–3025, 2011.

[63] E. Barakat, M.-P. Bernal, and F. I. Baida, "Theoretical analysis of enhanced nonlinear conversion from metallo-dielectric nano-structures," *Opt. Express*, vol. 20, no. 15, pp. 16258–16268, 2012.

[64] H. Aouani, M. Rahmani, M. Navarro-Cía, and S. A. Maier, "Third-harmonic-upconversion enhancement from a single semiconductor nanoparticle coupled to a plasmonic antenna," *Nat. Nanotechnol.*, vol. 9, no. 4, pp. 290–294, 2014.

[65] C. Argyropoulos, C. Ciracì, and D. R. Smith, "Enhanced optical bistability with film-coupled plasmonic nanocubes," *Appl. Phys. Lett.*, vol. 104, no. 6, p. 063108, 2014.

[66] Z. Huang, A. Baron, S. Larouche, C. Argyropoulos, and D. R. Smith, "Optical bistability with film-coupled metasurfaces," *Opt. Lett.*, vol. 40, no. 23, pp. 5638–5641, 2015.

[67] S. Guddala and S. A. Ramakrishna, "Optical limiting by nonlinear tuning of resonance in metamaterial absorbers," *Opt. Lett.*, vol. 41, no. 22, pp. 5150–4, 2016.

[68] F. Wang, M. Manjare, R. Lemasters, C. Li, and H. Harutyunyan, "Enhancing second-harmonic generation using dipolar-parity modes in non-planar plasmonic nanocavities," *Opt. Lett.*, vol. 44, no. 11, pp. 2787–2790, 2019.

[69] T. F. Heinz, "Second-order nonlinear optical effects at surfaces and interfaces," in *Modern Problems in Condensed Matter Sciences*, vol. 29, pp. 353–416, Elsevier, 1991.

[70] F. X. Wang, F. J. Rodríguez, W. M. Albers, R. Ahorinta, J. Sipe, and M. Kauranen, "Surface and bulk contributions to the second-order nonlinear optical response of a gold film," *Physical Review B*, vol. 80, no. 23, p. 233402, 2009.

[71] M. Corvi and W. Schaich, "Hydrodynamic-model calculation of second-harmonic generation at a metal surface," *Physical Review B*, vol. 33, no. 6, p. 3688, 1986.

[72] N. Bloembergen, R. K. Chang, S. S. Jha, and C. H. Lee, "Optical second-harmonic generation in reflection from media with inversion symmetry," *Phys. Rev.*, vol. 174, pp. 813–822, Oct 1968.

[73] C. Ciracì and F. D. Sala, "Quantum hydrodynamic theory for plasmonics: Impact of the electron density tail," *Physical Review B*, vol. 93, p. 205405, 2016.

[74] M. Khalid and C. Ciracì, "Enhancing second-harmonic generation with electron spill-out at metallic surfaces," *Commun. Phys.*, vol. 3, p. 214, 2020.

[75] C. Schäfer, F. Buchholz, M. Penz, M. Ruggenthaler, and A. Rubio, "Making ab initio qed functional(s): Nonperturbative and photon-free effective frameworks for strong light–matter coupling," *Proceedings of the National Academy of Sciences*, vol. 118, no. 41, p. e2110464118, 2021.

[76] N. A. Mortensen, "Mesoscopic electrodynamics at metal surfaces: — from quantum-corrected hydrodynamics to microscopic surface-response formalism," *Nanophotonics*, vol. 10, no. 10, pp. 2563–2616, 2021.

[77] J. E. Sipe, V. C. Y. So, M. Fukui, and G. I. Stegeman, "Analysis of second-harmonic generation at metal surfaces," *Phys. Rev. B*, vol. 21, pp. 4389–4402, May 1980.

[78] M. Scalora, G. D'Aguanno, N. Mattiucci, M. J. Bloemer, D. d. Ceglia, M. Centini, A. Mandatori, C. Sibilia, N. Akozbek, M. G. Cappeddu, M. Fowler, and J. W. Haus, "Negative refraction and sub-wavelength focusing in the visible range using transparent metallodielectric stacks," *Optics Express*, vol. 15, pp. 508–523, 2006.

[79] M. Scalora, M. A. Vincenti, D. d. Ceglia, V. Roppo, M. Centini, N. Akozbek, and M. J. Bloemer, "Second- and third-harmonic generation in metal-based structures," *Phys. Rev. A*, vol. 82, p. 043828, 2010-10.

[80] C. Ciracì, E. Poutrina, M. Scalora, and D. R. Smith, "Second-harmonic generation in metallic nanoparticles: Clarification of the role of the surface," *Phy. Rev. B*, vol. 86, p. 115451, 2012.

[81] C. Ciracì, E. Poutrina, M. Scalora, and D. R. Smith, "Origin of second-harmonic generation enhancement in optical split-ring resonators," *Physical Review B*, vol. 85, p. 201403, 2012.

[82] F. D. Luca and C. Ciracì, "Difference-frequency generation in plasmonic nanostructures: a parameter-free hydrodynamic description," *J. Opt. Soc. Am. B*, vol. 36, pp. 1979–1986, Aug 2019.

[83] S. Raza, T. Christensen, M. Wubs, S. I. Bozhevolnyi, and N. A. Mortensen, "Nonlocal response in thin-film waveguides: Loss versus nonlocality and breaking of complementarity," *Phys. Rev. B*, vol. 88, pp. 115401–9, 2013.

[84] Q. Huang, F. Bao, and S. He, "Nonlocal effects in a hybrid plasmonic waveguide for nanoscale confinement," *Opt. Express*, vol. 21, pp. 1430–1439, Jan 2013.

[85] G. Toscano, S. Raza, W. Yan, C. Jeppesen, and S. Xiao, "Nonlocal response in plasmonic waveguiding with extreme light confinement," *Nanophotonics*, vol. 2, pp. 161–166, 2013.

[86] H. M. Baghramyan, F. Della Sala, and C. Ciracì, "Laplacian-level quantum hydrodynamic theory for plasmonics," *Phys. Rev. X*, vol. 11, p. 011049, Mar 2021.

[87] H. P. Langtangen and K.-A. Mardal, *Introduction to numerical methods for variational problems*, vol. 21. Springer Nature, 2019.

[88] J.-M. Jin, *The finite element method in electromagnetics*. John Wiley & Sons, 2015.

[89] F. Zolla, G. Renversez, A. Nicolet, B. Kuhlmey, S. R. Guenneau, and D. Felbacq, *Foundations of photonic crystal fibres*. World Scientific, 2005.

[90] J. Kirkwood, *Mathematical physics with partial differential equations*. Academic Press, 2018.

[91] J. Wu, Z. T. Xie, Y. Sha, H. Fu, and Q. Li, "Epsilon-near-zero photonics: infinite potentials," *Photonics Research*, vol. 9, no. 8, pp. 1616–1644, 2021.

[92] A. Noor, A. R. Damodaran, I.-H. Lee, S. A. Maier, S.-H. Oh, and C. Ciracì, "Mode-matching enhancement of second-harmonic generation with plasmonic nanopatch antennas," *ACS Photonics*, vol. 7, pp. 3333–3340, 2020.

[93] A. Noor, A. R. Damodaran, I. Lee, S. A. Maier, S.-H. Oh, A. D'Orazio, and C. Ciracì, "Plasmonic nanopatch antennas as a doubly resonant platform for mode-matched second-harmonic generation," in *2021 Fifteenth International Congress on Artificial Materials for Novel Wave Phenomena (Metamaterials)*, pp. 305–307, 2021.

[94] E. Garmire, "Nonlinear optics in daily life," *Opt. Express*, vol. 21, no. 25, pp. 30532–30544, 2013.

[95] L. Carletti, A. Locatelli, O. Stepanenko, G. Leo, and C. D. Angelis, "Enhanced second-harmonic generation from magnetic resonance in algaas nanoantennas," *Opt. Express*, vol. 23, pp. 26544–26550, Oct 2015.

[96] S. Liu, M. B. Sinclair, S. Saravi, G. A. Keeler, Y. Yang, J. Reno, G. M. Peake, F. Setzpfandt, I. Staude, T. Pertsch, *et al.*, "Resonantly enhanced second-harmonic generation using iii–v semiconductor all-dielectric metasurfaces," *Nano Lett.*, vol. 16, no. 9, pp. 5426–5432, 2016.

[97] V. F. Gili, L. Carletti, A. Locatelli, D. Rocco, M. Finazzi, L. Ghirardini, I. Favero, C. Gomez, A. Lemaître, M. Celebrano, C. D. Angelis, and G. Leo, "Monolithic algaas second-harmonic nanoantennas," *Optics Express*, vol. 24, pp. 15965–7, 2016.

[98] J. D. Sautter, L. Xu, A. E. Miroshnichenko, M. Lysevych, I. Volkovskaya, D. A. Smirnova, R. Camacho-Morales, K. Zangeneh Kamali, F. Karouta, K. Vora, *et al.*, "Tailoring second-harmonic emission from (111)-gaas nanoantennas," *Nano Lett.*, vol. 19, no. 6, pp. 3905–3911, 2019.

[99] K. Koshelev, S. Kruk, E. Melik-Gaykazyan, J.-H. Choi, A. Bogdanov, H.-G. Park, and Y. Kivshar, "Subwavelength dielectric resonators for nonlinear nanophotonics," *Science*, vol. 367, no. 6475, pp. 288–292, 2020.

[100] G. Deka, C.-K. Sun, K. Fujita, and S.-W. Chu, "Nonlinear plasmonic imaging techniques and their biological applications," *Nanophotonics*, vol. 6, no. 1, pp. 31–49, 2017.

[101] M. P. Nielsen, X. Shi, P. Dichtl, S. A. Maier, and R. F. Oulton, "Giant nonlinear response at a plasmonic nanofocus drives efficient four-wave mixing," *Science*, vol. 358, no. 6367, pp. 1179–1181, 2017.

[102] L. Caspani, C. Xiong, B. J. Eggleton, D. Bajoni, M. Liscidini, M. Galli, R. Morandotti, and D. J. Moss, "Integrated sources of photon quantum states based on nonlinear optics," *Light: Sci. Appl.*, vol. 6, no. 11, pp. 17100–17100, 2017.

[103] M. Celebrano, X. Wu, M. Baselli, S. Großmann, P. Biagioni, A. Locatelli, C. De Angelis, G. Cerullo, R. Osellame, B. Hecht, *et al.*, "Mode matching in multiresonant plasmonic nanoantennas for enhanced second harmonic generation," *Nat. Nanotechnol.*, vol. 10, no. 5, pp. 412–417, 2015.

[104] F. Wang, A. B. Martinson, and H. Harutyunyan, "Efficient nonlinear metasurface based on nonplanar plasmonic nanocavities," *ACS Photonics*, vol. 4, no. 5, pp. 1188–1194, 2017.

[105] K. Thyagarajan, S. Rivier, A. Lovera, and O. J. Martin, "Enhanced second-harmonic generation from double resonant plasmonic antennae," *Opt. Express*, vol. 20, no. 12, pp. 12860–12865, 2012.

[106] H. Aouani, M. Navarro-Cia, M. Rahmani, T. P. Sidiropoulos, M. Hong, R. F. Oulton, and S. A. Maier, "Multiresonant broadband optical antennas as efficient tunable nanosources of second harmonic light," *Nano Lett.*, vol. 12, no. 9, pp. 4997–5002, 2012.

[107] W. R. Holland and D. G. Hall, "Frequency shifts of an electric-dipole resonance near a conducting surface," *Phys. Rev. Lett.*, vol. 52, pp. 1041–1044, Mar 1984.

[108] A. Aubry, D. Y. Lei, S. A. Maier, and J. B. Pendry, "Plasmonic hybridization between nanowires and a metallic surface: a transformation optics approach," *ACS Nano*, vol. 5, no. 4, pp. 3293–3308, 2011.

[109] J. J. Mock, R. T. Hill, A. Degiron, S. Zauscher, A. Chilkoti, and D. R. Smith, "Distance-dependent plasmon resonant coupling between a gold nanoparticle and gold film," *Nano Lett.*, vol. 8, no. 8, pp. 2245–2252, 2008.

[110] C. Ciracì, X. Chen, J. J. Mock, F. McGuire, X. Liu, S.-H. Oh, and D. R. Smith, "Film-coupled nanoparticles by atomic layer deposition: Comparison with organic spacing layers," *Appl. Phys. Lett.*, vol. 104, no. 2, p. 023109, 2014.

[111] J. B. Lassiter, F. McGuire, J. J. Mock, C. Ciracì, R. T. Hill, B. J. Wiley, A. Chilkoti, and D. R. Smith, "Plasmonic waveguide modes of film-coupled metallic nanocubes," *Nano Lett.*, vol. 13, no. 12, pp. 5866–5872, 2013.

[112] C. K. Dass, H. Kwon, S. Vangala, E. M. Smith, J. W. Cleary, J. Guo, A. Alu, and J. R. Hendrickson, "Gap-plasmon-enhanced second-harmonic generation in epsilon-near-zero nanolayers," *ACS Photonics*, vol. 7, no. 1, pp. 174–179, 2019.

[113] D. Knebl, A. Hörl, A. Trügler, J. Kern, J. R. Krenn, P. Puschnig, and U. Hohenester, "Gap plasmonics of silver nanocube dimers," *Phys. Rev. B: Condens. Matter Mater. Phys.*, vol. 93, p. 081405, Feb 2016.

[114] A. Rose, T. B. Hoang, F. McGuire, J. J. Mock, C. Ciracì, D. R. Smith, and M. H. Mikkelsen, "Control of radiative processes using tunable plasmonic nanopatch antennas," *Nano Lett.*, vol. 14, no. 8, pp. 4797–4802, 2014.

[115] C. Ciracì, J. B. Lassiter, A. Moreau, and D. R. Smith, "Quasi-analytic study of scattering from optical plasmonic patch antennas," *J. Appl. Phys.*, vol. 114, no. 16, p. 163108, 2013.

[116] G. M. Akselrod, T. Ming, C. Argyropoulos, T. B. Hoang, Y. Lin, X. Ling, D. R. Smith, J. Kong, and M. H. Mikkelsen, "Leveraging nanocavity harmonics for control of optical processes in 2d semiconductors," *Nano Letters*, vol. 15, pp. 3578–3584, 2015.

[117] M. W. Klein, C. Enkrich, M. Wegener, and S. Linden, "Second-harmonic generation from magnetic metamaterials," *Science*, vol. 313, no. 5786, pp. 502–504, 2006.

[118] B. Metzger, L. Gui, J. Fuchs, D. Floess, M. Hentschel, and H. Giessen, "Strong enhancement of second harmonic emission by plasmonic resonances at the second harmonic wavelength," *Nano Lett.*, vol. 15, no. 6, pp. 3917–3922, 2015.

[119] J. B. Lassiter, X. Chen, X. Liu, C. Ciracì, T. B. Hoang, S. Larouche, S.-H. Oh, M. H. Mikkelsen, and D. R. Smith, "Third-harmonic generation enhancement by film-coupled plasmonic stripe resonators," *ACS Photonics*, vol. 1, no. 11, pp. 1212–1217, 2014.

[120] J. Butet, S. Dutta-Gupta, and O. J. F. Martin, "Surface second-harmonic generation from coupled spherical plasmonic nanoparticles: Eigenmode analysis and symmetry properties," *Physical Review B*, vol. 89, pp. 245449–10, 2014.

[121] Y. Zeng, H. Qian, M. J. Rozin, Z. Liu, and A. R. Tao, "Enhanced second harmonic generation in double-resonance colloidal metasurfaces," *Advanced Functional Materials*, vol. 28, pp. 1803019–8, 2018.

[122] J. Müller, U. Schröder, T. Böscke, I. Müller, U. Böttger, L. Wilde, J. Sundqvist, M. Lemberger, P. Kücher, T. Mikolajick, and L. Frey, "Ferroelectricity in yttrium-doped hafnium oxide," *J. Appl. Phys.*, vol. 110, no. 11, p. 114113, 2011.

[123] R. L. Olmon, B. Slovick, T. W. Johnson, D. Shelton, S.-H. Oh, G. D. Boreman, and M. B. Raschke, "Optical dielectric function of gold," *Phys. Rev. B: Condens. Matter Mater. Phys.*, vol. 86, p. 235147, Dec 2012.

[124] M. J. Dicken, L. A. Sweatlock, D. Pacifici, H. J. Lezec, K. Bhattacharya, and H. A. Atwater, "Electrooptic modulation in thin film barium titanate plasmonic interferometers," *Nano Lett.*, vol. 8, no. 11, pp. 4048–4052, 2008.

[125] A. Noor, M. Khalid, F. De Luca, H. M. Baghramyan, M. Castriotta, A. D'Orazio, and C. Ciracì, "Second-harmonic generation in plasmonic waveguides with nonlocal response and electron spill-out," *Phys. Rev. B*, vol. 106, p. 045415, Jul 2022.

[126] D. Martin-Cano, L. Martin-Moreno, F. J. Garcia-Vidal, and E. Moreno, "Resonance energy transfer and superradiance mediated by plasmonic nanowaveguides," *Nano Lett.*, vol. 10, no. 8, pp. 3129–3134, 2010.

[127] Z. Ruan, G. Veronis, K. L. Vodopyanov, M. M. Fejer, and S. Fan, "Enhancement of optics-to-thz conversion efficiency by metallic slot waveguides," *Opt. Express*, vol. 17, pp. 13502–13515, Aug 2009.

[128] J. Zhang, E. Cassan, D. Gao, and X. Zhang, "Highly efficient phase-matched second harmonic generation using an asymmetric plasmonic slot waveguide configuration in hybrid polymer-silicon photonics," *Opt. Express*, vol. 21, pp. 14876–14887, Jun 2013.

[129] P. Ginzburg, A. V. Krasavin, and A. V. Zayats, "Cascaded second-order surface plasmon solitons due to intrinsic metal nonlinearity," *New Journal of Physics*, vol. 15, p. 013031, jan 2013.

[130] "Comsol multiphysics."

[131] F. De Luca, M. Ortolani, and C. Ciracì, "Free electron nonlinearities in heavily doped semiconductors plasmonics," *Phys. Rev. B*, vol. 103, p. 115305, Mar 2021.

[132] T. Taliercio and P. Biagioni, "Semiconductor infrared plasmonics," *Nanophotonics*, vol. 8, pp. 949–990, 2019.